Jens Gunnar Slettedal

Numerical Investigation of Scrubber

Master's thesis in Mechanical Engineering
Supervisor: Reidar Kristoffersen
June 2019

Master's thesis

NTNU
Norwegian University of Science and Technology
Faculty of Engineering
Department of Energy and Process Engineering

NTNU
Norwegian University of
Science and Technology

NIKKELVERK
A GLENCORE COMPANY

Jens Gunnar Slettedal

Numerical Investigation of Scrubber

Master's thesis in Mechanical Engineering
Supervisor: Reidar Kristoffersen
June 2019

Norwegian University of Science and Technology
Faculty of Engineering
Department of Energy and Process Engineering

NTNU
Kunnskap for en bedre verden

Preface

This thesis marks the end of the five years I have spent at the Norwegian University of Science and Technology (NTNU). Throughout the studies, fluid mechanics and computational fluid dynamics have been the most interesting topics and this thesis epitomizes my academical inclination. Modelling turbulent particle-laden flows is complex due to the advanced theory and the numerous approaches found in the literature. Considering the extensive work in this thesis, I feel that I have surpassed the original scope of understanding I had hoped to achieve. Moreover, I have obtained a profound motivation for continuing within the field of fluid mechanics. Finally, I am certain that my experiences and knowledge obtained during my master thesis, will be of great value to me in the coming years.

Firstly, I would like to thank my supervisor Associate Professor Reidar Kristoffersen for helpful guidelines and by offering his expertise and time. Secondly, I would like to extend my gratitude to Glencore Nikkelverk, and specifically Per Ramsdal for providing me an interesting and topical problem description. In addition, I am grateful for the measurements provided by Ernst Rosseland. Lastly, special thanks to my supporting family and Mari for encouragement throughout the work with this master thesis.

Trondheim, 10.06.2019

Jens Gunnar Slettedal

Abstract

Glencore Nikkelverk is designing a large-scale venturi scrubber to clean pollutant gas from a new processing plant. The proposed design by Glencore Nikkelverk of the large-scale scrubber is based on an already installed smaller venturi scrubber. By obtaining the fluid dynamics of the scrubber it is possible to optimize the design and reduce air pollution in accordance to the modern standards for a greener future. This thesis investigates the particle-laden gas flow in the installed scrubber at Glencore Nikkelverk and the full-scale scrubber by means of CFD. Furthermore, two test cases were performed to enhance validation of the simulations of the scrubber. Specifically, turbulence modelling was benchmarked in the first test case, i.e. turbulent flow in a concentric annulus. Simulations with standard two-equation turbulence models and Reynolds stress model were performed and compared to experimental and numerical data in the literature. In the second test case, confined bluff body flow, the particle modelling was benchmarked by comparisons of simulations and experimental data.

Based on the findings of the two test cases, two-dimensional axisymmetric simulations of the installed scrubber were performed. One of the most important design parameters is the pressure drop across the venturi scrubber. In the present study, the pressure drop was computed for different operating conditions. The computed pressure drop was within the standard deviation of the measurements obtained by Glencore Nikkelverk for the installed venturi scrubber. The conducted literature study revealed that most designers rely on empirical correlations for determining the pressure drop. For an accurate a priori pressure drop estimation based on empirical correlations, appropriate factors must be determined. Thus, the reliability of these correlations is limited, and a CFD simulation is therefore preferred.

An investigation of the particle paths in the installed scrubber was conducted. The results were consistent with the literature, i.e. the smaller particles are more difficult to separate from the gas phase than larger particles. Finally, simulations of the large-scale scrubber were performed where the dimensions are scaled-up by a factor of ten. The results indicated smaller particle Stokes number and less efficient separation than the installed scrubber. It was found that further work is needed in order to accurately predict the particle collection efficiency.

Sammendrag

Glencore Nikkelverk utvikler en fullskala venturi skrubber for å rense forurenset gass fra et nytt prosessanlegg. Designet skal optimalisere separasjon av partikler i gassfasen og skal baseres på en mindre installert skrubber. Høy virkningsgrad er avgjørende for å imøtekomme standarder for luftforurensing og bidra til et grønnere og mer bærekraftig miljø. Denne oppgaven anvender CFD som analyseverktøy for partikkelbelastet gasstrømning i både den installerte og fullskala skrubberen. To klassiske interne strømningstilfeller ble undersøkt for validering av de numeriske beregningene av skrubberen. Turbulens modellering ble undersøkt i det første strømningstilfellet, turbulent strømning i en konsentrisk annulus. CFD simuleringer med standard to-lignings turbulens modeller og Reynoldsspennings modell ble benyttet og sammenlignet med eksperimentelle data og numeriske simuleringer i litteraturen. I det andre strømningstilfellet, nedstrøms rørstrømning rundt et butt objekt, er partikkel modelleringen validert ved sammenligning med eksperimentell data.

Basert på erfaringer fra de to strømningstilfellene ble det utført todimensjonale aksesymmetrisk numeriske beregninger av den installerte skrubberen. En viktig design parameter er trykkfallet over skrubberen. I denne oppgaven ble trykkfallet beregnet ved forskjellige driftstilstander. Beregnet trykkfall for den installerte skrubberen er innenfor standardavviket for målingene utført av Glencore Nikkelverk. Litteraturstudiet viste at hovedsakelig empiriske korrelasjoner blir brukt til å beregne trykkfallet i utviklingsfasen. Et nøyaktig a priori estimat av trykkfallet avhenger av at korrekte konstanter blir satt i de empiriske korrelasjonene. Derfor er påliteligheten av disse korrelasjonene begrenset og CFD simuleringer er dermed foretrukket.

Partikkelbaner i den installerte skrubberen ble undersøkt. Det er funnet at mindre partikler er vanskeligere å separere fra gassfasen enn større partikler, som er bekreftet i litteraturstudiet. Til slutt, ble simuleringer av en fullskala skrubber utført, hvor dimensjonene er oppskalert med en faktor på ti. Resultatene indikerte lavere Stokes nummer og mindre effektiv seperasjon av partikler. Det er funnet at betraktinger utenfor oppgavens avgrensning må inkluderes for å designe en effektiv fullskala skrubber.

Contents

List of Figures

Nomenclature

$-\overline{u_i' u_j'}$	Reynolds stress tensor
α	Volume fraction
ΔP	Pressure drop
δ_{ij}	Kronecker delta
$\dot{m}$	Mass flow rate
ϵ	Turbulent dissipation rate
ϵ_{ij}	Dissipation rate tensor
η	Kolmogorov length scale
$\mathcal{L}$	Length scale of the larger eddies
μ	Dynamic viscosity
μ_T	Turbulent viscosity
∇	Diffential operator
ν	Kinematic viscosity
ω	specific dissipation rate
$\overline{u}, \overline{v}, \overline{w}$	Mean velocity component in x-, y- and z-direction
ϕ_{ij}	Pressure-strain tensor
ψ	Pressure drop factor
ρ	Density
ρ_P	Particle density
τ_F	Fluid characteristic time scale

τ_K	Kolmogorov time scale
τ_P	Particle response time
τ_{ij}	Viscous stress tensor
τ_{Re}	Reynolds stress
τ_{Tot}	Total shear stress
θ	Radius ratio
$\mathbf{U}$	Velocity vector in three dimensions
$\mathbf{x_P}$	Position vector of the particle
C_D	Drag coefficient
d_P	Particle diameter
f	Body forces
F_D	Drag force
I	Turbulent intensity
k	Turbulent kinetic energy
m_p	Mass of particle
p	Pressure
p_{grid}	Order of grid convergence
Q	Volumetric flow rate
r_{eff}	Effective refinement ratio
r_g	Refinement ratio
Re	Reynolds number
Re_P	Particle Reynolds number
Re_y	Turbulent Reynolds number
S	Stagnation point
S_{ij}	Rate of mean strain tensor

St Stokes number

u, v, w Velocity component in x-, y- and z-direction

u^+ Dimensionless velocity

U_b Bulk velocity

u_P Velocity of particle

u_τ Friction velocity

v_{gt} Throat velocity

y^+ Dimensionless distance from wall

Chapter 1

Introduction

1.1 Background

In recent years there has been an increased interest in gas cleaning due to new standards for air pollution control in the general industry, marine, as well as in the oil and gas industry. Glencore Nikkelverk AS produce high quality nickel and cobalt as well as copper and sulphuric acid. The company aim to lead the technological development in the market and operate to the high standards and principles set for sustainable development. Glencore Nikkelverk AS is investing in a new copper production process. The aim is to develop a cleaning process of the polluted air from this process to comply with the company's focus on sustainability. Glencore Nikkelverk AS is issued a permit by the Norwegian Environment Agency for activities that may cause pollution. The permit is based on the Pollution Control Act and the purpose of the act "is to protect the outdoor environment against pollution and to reduce existing pollution, to reduce the quantity of waste and to promote better waste management" [1]. The permit conditions including emission limit values are set on the basis of Best Available Techniques (BAT) [23] under Directive 2010/75/EU of the European Parliament and of the Council on industrial emissions, for the non-ferrous metals industries.

There exists many different devices that can be used for gas cleaning, e.g. settling chambers, centrifugal separators, wet scrubbers, packed beds, high-efficiency air filters, mechanical separators, electrical precipitators. The venturi scrubber is a type of wet scrubber. A scrubbing liquid is used for removing particles from the polluted gas. The flow in a scrubber include complex geometry, turbulence and multi-phase with interaction between gas, liquid and particles. Understanding the behaviour of the particle-laden gas flow is crucial knowledge in order to predict the particle collection efficiency of a venturi scrubber. Only by obtaining an understanding of the physics involved, it is possible to predict and design gas cleaning devices to meet the standards for air pollution and to ensure a greener future.

1.2 Previous work

The present work is a continuation of the project work completed by the author at Norwegian University of Science and Technology (NTNU) during the autumn of 2018. The project work provided an introduction to CFD and particle-laden gas flows through the OpenFOAM software. In addition, a detailed literature study of particle-laden gas flows was conducted. Particle-laden gas flow over a backward-facing step (BFS) were investigated with the $k - \epsilon$ turbulence model. Results were compared with experimental data provided by Eaton and Fessler [30] and numerical data by Greifzu et al. [33], Jin et al. [40] and Lu et al. [50]. In addition, flow characteristics and setup were modified to gain knowledge of particle-laden flows. The project provided the author with important experience and knowledge about particle-laden flows in order to approach the current thesis in an efficient manner.

1.3 Scope of this thesis

The purpose of this thesis is to develop a numerical model of the particle-laden gas flow in the venturi scrubber in ANSYS Fluent. Consequently, a literature study of the venturi scrubber and particle-laden gas flows will be conducted. Furthermore, two test cases are investigated to validate the numerical model of the scrubber. Simulations of test cases are conducted and validated by experimental and numerical data available in the literature. The thesis is divided into three cases:

- Turbulent flow in concentric annulus
- Confined bluff body
- Venturi scrubber

The first two cases include physics that need special considerations in the venturi scrubber. The scope of this thesis will include a numerical analysis of one continuous phase of air and the dispersed phase of solid particles for the venturi scrubber. This is to set a basis for a future multiphase model of the venturi scrubber where air, liquid water and solid particles are considered in order to predict the particle collection efficiency. This thesis will not include the liquid phase, the liquid droplet breakup nor the interaction between the droplets and solid particles and its associated chemistry. Numerical simulations will be performed for the installed venturi scrubber at Glencore Nikkelverk. The results, i.e. pressure drop across the venturi scrubber, from the presented numerical model are compared to experimental data, provided by Glencore Nikkelverk AS. Finally, the geometry of the installed scrubber will be scaled up to predict the flow in a full-scale venturi scrubber which is planned to be built in 2022.

1.4 Outline of the thesis

Chapter 2 will cover the relevant theory to the numerical analysis in the present study. An introduction to the governing equations, turbulence modelling and particle-laden gas flows are given. The mathematical models used in this study are explained in detail.
A short introduction of CFD software and level of modelling is provided in chapter 3. In addition, a short note on different types of grids and mesh generation is included. The three cases, i.e. turbulent flow in a concentric annulus, confined bluff body (CBB) and venturi scrubber are given in chapter 4, 5, 6, respectively. The results from the calculations for each case will be presented consecutively. The results of the concentric annulus and CBB are compared to experimental and numerical data available in the literature, while the results of the pilot venutri scrubber are compared to experimental data by Glencore Nikkelverk. Finally, concluding remarks and recommended further work will subsequently be given in chapter 7 and 8.

1.5 Literature Survey

Particle-laden flows have been subject to research for a long time. This is because particle-laden flows are found in many engineering applications as well as in natural settings, this includes for example separation of particles, erosion, combustion and sedimentation. Relevant text books for particle-laden flows are Crowe, Sommerfeld and Tsuji [21], Varaksin [84] and Schellander [72]. In particle-laden flows there are three different flow regimes and a corresponding coupling between the continuous and dispersed particle phase. Elghobashi [28] proposed a method to determine what regime is present for particle-laden flows. The approach by Elghobashi [28] is presented in section 2.9. The review by Van der Hoef et al. [83] states the different approaches to solve particle-laden gas flows numerically. The three main approaches are resolved particle model, which is a direct numerical simulation (DNS), unresolved discrete particle models (DPM) and two-fluid models. A review by Kuerten [52] give an overview of the research on particle-laden flow for DNS and large eddy simulation (LES). The discrete particle model (DPM) is a frequently applied model for numerical computations of particle-laden flows and is based on the work by Cundall [22]. The review of Deen [26] contains different approaches on how fluidized beds can be computed by discrete particle modelling today.

The venturi scrubber is a highly efficient particle-laden gas cleaning device and it is used in various industries and power plants. Relevant text books for scrubbers and air pollution are Wang et al. [87], Danielson [25], Couper et al. [19] and Perry [62]. In the wake of the Fukushima Daiichi nuclear disaster in 2011 countermeasures are urgently needed. As a result of increased focus on safety of nuclear power plants, Ali et al. [4] gave a comprehensive re-

view of the venturi scrubber. The review presented published studies related to performance of the venturi scrubber in the last few decades. The review state that performance is dependent on droplet dispersion, pressure drop, atomization, size of droplets, injection method and collection mechanism. The pressure drop is one of the most important parameter. As the pressure drop is related to both collection efficiency and operational cost, several models have been developed. The pressure drop model by Calvert [16] is one of the simplest models. The pressure drop is predicted due to change in momentum of droplets in the throat and the model does not include the geometry of the scrubber. More sophisticated pressure drop models have been developed on the basis of the simple model by Calvert [16], e.g. Viswanathan [86] and Azzopardi et al. [11]. Allen and van Santen [5] measured the pressure drop for different operating conditions for a venturi scrubber. The study is relevant because of measurements in terms of dry and wet pressure drop. Allen and van Santen stated that the turbulence-induced gas phase losses, i.e. dry pressure drop, is important in determining the total pressure drop.

Some numerical analysis with the use of CFD software have been performed. Goniva [32] conducted a simulation of a venturi scrubber in the OpenFOAM software to determine the performance. An Eulerian-Langrangian approach for the particle-laden gas and the droplets was used. The simulated pressure drops were in good quantitative agreement with experiments, while an accurate prediction of the collection efficiency was however not achieved. Guerra et al. [35] conducted experiments and CFD simulations for a venutri scrubber and focused on pressure drop and liquid distribution. Pak & Chang [60] developed a numerical model to predict pressure drop and collection efficiency of a venturi scrubber. The simulated pressure drop was a little under-predicted compared to experimental data. The inaccurate prediction of the droplet size and no liquid film modelling were given as arguments for the under-predicted pressure drop. The collection efficiency was in good agreement with experimental data except for the low gas throat velocity. All simulations of the aforementioned authors used the $k - \epsilon$ turbulence model.

In terms of geometric similarities of the installed scrubber at Glencore Nikkelverk and the literature, the venturi scrubber in the study by Viswanathan [86] has been found to be closest. Based on experimental studies, Viswanathan developed an empirical correlation for the two-phase pressure drop in the scrubber. However, no identical geometry was found in the literature and thereby validation of the venturi scrubber simulations is obtained by the test cases and the measurements provided by Glencore Nikkelverk.

Chapter 2

Theory

2.1 Governing Equations

There are three universal laws of conservation in fluid mechanics: conservation of mass, conservation of momentum and conservation of energy.

2.1.1 Conservation of mass

Conservation of mass, implies that mass cannot be created or destroyed in a flow field. Using the Eulerian approach, the conservation of mass is given as:

$$\frac{\partial}{\partial t}\int_V \rho dV = -\oiint_S \rho \mathbf{U}\cdot\mathbf{n}dS \tag{2.1}$$

The equation states that the rate of increase of mass inside the volume, V, is equal to the net inflow of mass through the closed surface S. By applying the divergence theorem and consider that the equation is valid for any arbitrary volume, equation 2.1 may be written as:

$$\frac{\partial \rho}{\partial t} + \frac{\partial(\rho u_i)}{\partial x_i} = 0 \tag{2.2}$$

A special case give an important simplification of equation 2.2. For homogeneously constant density, which is valid for incompressible flows, equation 2.2 is reduced to:

$$\frac{\partial u_i}{\partial x_i} = 0 \tag{2.3}$$

2.1.2 Conservation of momentum

For stationary control volume Ω, with boundary $\partial\Omega$, considering pressure, viscous and volume forces as external forces the momentum equation on integral form is:

$$\int_{\Omega} \frac{\partial \rho \mathbf{U}}{\partial t} dV + \int_{\partial\Omega} \rho \mathbf{U}\mathbf{U} \cdot \mathbf{n} dA = -\int_{\partial\Omega} p\mathbf{n} dA + \int_{\partial\Omega} \tau \cdot \mathbf{n} dA + \int_{\Omega} \rho \mathbf{f} dV \tag{2.4}$$

Simplifying equation 2.4, in a Cartesian coordinate system, for an incompressible, Newtonian fluid flow and constant viscosity and density, give rise to the famous Navier-Stokes equation:

$$\frac{\partial u_i}{\partial t} + u_j \frac{\partial u_i}{\partial x_j} = -\frac{1}{\rho}\frac{\partial p}{\partial x_i} + \nu \frac{\partial^2 u_i}{\partial x_j \partial x_j} + \frac{f}{\rho} \tag{2.5}$$

where p is the pressure, ν is the kinematic viscosity of the fluid and f is the body force, e.g. gravity. Equation 2.5 is valid for an incompressible, Newtonian fluid flow problem. Steady air flows are assumed to be incompressible for fluid velocities below 100 m/s, according to Pletcher [63] .

2.2 Principles of solution

To solve the governing equations in a numerical approach, physical space and time are discretized. Different discretization schemes are used in time and space, since the different terms of the governing equations are approximated at different levels. For a transient problem the equations are time-dependent and advanced in time from initial conditions. A steady state is achieved when the solution is time independent. Appropriate boundary conditions must be applied and are given in section 3.3.

2.2.1 Spatial discretization

There are three main concepts of spatial discretization, finite difference, finite volume and finite element. It is well known that finite difference and finite volume method (FVM) is closely related [63]. This thesis is based on the formulation of finite volume. The finite volume method uses the integral formulation of the Navier-Stokes, equation 2.4. In the finite volume approach, the continuous problem domain is discretized into control volumes. These control volumes represent a spatial grid for the computational domain with associated grid points. A typical CV in 2D are shown in Fig. 2.1. The surfaces of the CV are denoted with lower-case letters, w (west), e (east), n (north) and s (south), with a central node (P). The governing integral conservation equation is valid for each CV and for the whole domain. Summation of the equations for all CVs yield the global conservation equation. As a result the global conservation is built into the FVM-method. In this project a cell-centered method is used where the grid points are in the centers of the volume. In addition the co-located grid system is used, based on the work by Rhie and Chow [67]. As a consequence all variables are stored in one point.

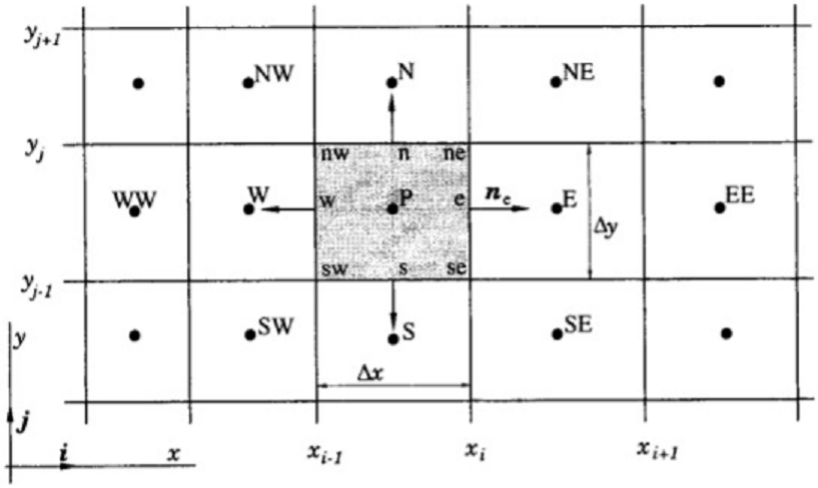

Figure 2.1 Schematic representation of CV for a 2D Cartesian grid and notations, adapted from [29].

In order to approximate the integrals of equation 2.4 the values of variables at other locations, than the CV center, are needed. The following will show schemes to approximate these variables.

Schemes for convection and diffusion

The convective flux for a quantity ϕ is given by:

$$f^c = \rho\phi\mathbf{U} \cdot \mathbf{n} \tag{2.6}$$

The diffusive flux for the same quantity ϕ is given as:

$$f^d = \Gamma\nabla\phi \cdot \mathbf{n} \tag{2.7}$$

The velocity field, the density and fluid property Γ are assumed to be known at all locations. The value of ϕ and its normal gradient on the surface of the CV are needed. To find the value at the surface, interpolation of the centre values is performed. The most popular schemes, according to Ferziger [29], are presented for the value of ϕ and its normal gradient at the eastern cell face, "e", corresponding with Fig. 2.1.

Upwind Differencing Scheme (UDS)
The first order upwind scheme use a forward- or backward-difference approximation depend-

ing on the flow direction. Using the UDS, the value of ϕ_e is approximated by:

$$\phi_e = \begin{cases} \phi_P & \text{if} \quad (\mathbf{U} \cdot \mathbf{n})_e > 0 \\ \phi_E & \text{if} \quad (\mathbf{U} \cdot \mathbf{n})_e < 0 \end{cases} \tag{2.8}$$

The scheme unconditionally satisfies the boundedness criterion. However, it is only a first order scheme and introduce numerical diffusion, which can be shown by Taylor series expansion.

Central-difference scheme (CDS)
The central-difference scheme is based on linear interpolation between the two neighboring nodes. Using the CDS, the value of ϕ_e is approximated by:

$$\phi_e = \phi_E \lambda_e + \phi_P (1 - \lambda_e), \quad \lambda_e = \frac{x_e - x_P}{x_E - x_P} \tag{2.9}$$

The CDS is second-order accurate and most widely used, but may produce oscillatory solutions.

Another relevant scheme is the Linear Upwind Scheme, which is second-order accurate, where the quantities at cell faces are computed using a multidimensional linear reconstruction approach, see Barth & Jespersen [12]. A number of higher-order schemes are available and often used together with limiters. Limiters are used to avoid oscillations for high gradients regions, see Pletcher [63] and Ferziger [29].

2.3 RANS - Reynolds Averaged Navier-Stokes

An important simplification of the Navier-Stokes equations is to assume a time averaging of the equations. This is known as the Reynolds averaged Naiver-Stokes equations. The instantaneous quantities are split into mean and fluctuating components by Reynolds decomposition. The streamwise velocity component for a Cartesian coordinate system is decomposed as

$$u = \overline{u} + u' \tag{2.10}$$

where u is the instantaneous velocity, $\overline{u}$ is the mean value of velocity and u' is the fluctuating value of velocity. As a result of the Reynolds decomposition, the mean of a fluctuating component is zero by definition. The reader should also notice that the time average of the product of two fluctuating quantities is, in general, not equal to zero. By Reynolds decomposition and time averaging of equation 2.5, the RANS equation is given as [63]:

$$\frac{\partial}{\partial t}(\rho\overline{u_i}) + \frac{\partial}{\partial x_j}(\rho\overline{u_i u_j}) = -\frac{\partial \overline{p}}{\partial x_i} + \frac{\partial}{\partial x_j}(\overline{\tau_{ij}} - \rho\overline{u_i' u_j'}) + \overline{f_i} \tag{2.11}$$

where $\overline{\tau_{ij}}$ is the averaged viscous stress tensor, given as:

$$\overline{\tau_{ij}} = \mu\left(\frac{\partial \overline{u_i}}{\partial x_j} + \frac{\partial \overline{u_j}}{\partial x_i}\right) \tag{2.12}$$

In equation 2.11 the Reynold stress tensor, $\overline{u_i' u_j'}$, is introduced and will be revisited. At this point is hard to see why this is a helpful simplification to solve the NS equations as new unknowns are introduced, like the Reynolds stress tensor. Therefore, new equations are needed in order to close the system of equations. This is achieved by turbulence modelling.

Most flows occurring in nature are turbulent, this also apply in many engineering applications. Turbulence has no precise definition, but turbulence characteristics are given after Tennekes & Lumley [81]:

- Randomness - All turbulent flows are irregular and statistical methods are applied.
- Diffusive - The diffusivity of turbulence is responsible for enhanced mixing of momentum, heat and mass transfer.
- Large Reynolds number - A characteristic of turbulence is large Reynolds number.
- Three dimensional
- Transient
- Dissipative

- Continuum phenomenon

It is known that in turbulent flows a wide range of length scales exists. The largest length scale is bounded by the dimensions of the flow field, while the smallest is bounded by the diffusive action of molecular viscosity. As a result also different time scales exists. The smallest scales are the Kolmogorov microscales of length, time and velocity. The Kolmogorov time scale is given as:

$$\tau_K = \left(\frac{\nu}{\epsilon}\right)^{1/2} \tag{2.13}$$

where ϵ is the turbulent dissipation rate per unit mass. The Kolmogorov length scale is given as:

$$\eta = \left(\frac{\nu^3}{\epsilon}\right)^{1/4} \tag{2.14}$$

2.4 Turbulence Modelling

The unknown averages of products of fluctuating quantities in the RANS equation can be modelled with equations for dependent variables. An example of a turbulence model is the relation between the unknown Reynolds stresses and the mean velocity components. An overview of turbulence models with an increase in complexity is given, according to Kristoffersen [43]: algebraic models, one-equation model, two-equation model, algebraic stress model (ASM), Reynolds stress model (RSM), Large Eddy Simulation (LES) and Direct Numerical Simulation (DNS). In this thesis several turbulence models is utilized. Therefore, the two equation models $k-\epsilon$, $k-\omega$, $k-\omega SST$ and RSM are presented. ANSYS Fluent is used in this study. Consequently, the turbulence models are given according to the implementation in Fluent. In addition, a short note on ASM is given.

A common approximation to obtain closure is the Boussinesq's eddy viscosity hypothesis relate the unknown Reynolds stresses to the mean flow:

$$-\overline{u_i' u_j'} = 2\nu_T S_{ij} - \frac{2}{3}k\delta_{ij} \tag{2.15}$$

where $S_{ij} = \frac{1}{2}(\frac{\partial \overline{u_i}}{\partial x_j} + \frac{\partial \overline{u_j}}{\partial x_i})$ is the mean strain rate and ν_t is the turbulent viscosity. The turbulent kinetic energy k is a measure of the turbulence intensity and is given as:

$$k = \frac{1}{2}\overline{u_i' u_i'} \tag{2.16}$$

The exact differential equation for the turbulent kinetic energy can be derived from the Navier-Stokes equations assumed constant density:

$$\frac{\partial k}{\partial t} + \overline{u_j}\frac{\partial k}{\partial x_j} = D_k + P_k - \epsilon \tag{2.17}$$

where

$$D_k = -\frac{\partial}{\partial x_i}\left[\overline{u_i'\left(\frac{p}{\rho} + k\right)}\right] + \frac{\partial}{\partial x_i}\left(2\nu\overline{u_j' s_{ij}'}\right) \tag{2.18}$$

$$P_k = -\overline{u_i' u_j'}\frac{\partial \overline{u_i}}{x_j} \tag{2.19}$$

$$\epsilon = 2\nu\overline{s_{ij}' s_{ij}'} \tag{2.20}$$

Equation 2.17 has the same form as an general transport equation where the left hand side of equation 2.17 represents the rate of change of k within a fluid element. The terms on the right hand side may contribute to the change of k. The first term on the right hand side of equation 2.17, D_k represents the diffusion of k due to molecular and turbulent transport and has a spatial redistribution effect. Further, P_k is characterized as the production term due to interaction of the mean flow and the turbulent stresses. The unknown Reynolds stresses can be modelled by the eddy viscosity hypothesis given in equation 2.15. The last term on the right hand side of equation 2.17 is the dissipative term where ϵ is the viscous dissipation rate of turbulent kinetic energy. Due to viscous stresses, energy is extracted from the turbulence. The energy cascade involve energy transfer from the larger eddies down to the smallest eddies and then to be dissipated. By length scale and dimensional analysis [81] it can be shown that the viscous dissipation cannot be neglected and that the dissipation can be estimated from

$$\epsilon \approx C_d \frac{k^{3/2}}{\mathcal{L}} \tag{2.21}$$

where C_d is an empirical constant and $\mathcal{L}$ is the length scale of the larger eddies.

2.5 Two-equation turbulence models

Two-equation models are characterized by one PDE for the turbulent kinetic energy, k, and one PDE for the length scale of the larger eddies $\mathcal{L}$. Several proposals have been made to obtain a dependent variable. The most used two-equation models are the $k-\epsilon$ and $k-\omega$. Both models are based on the the eddy viscosity hypothesis.

2.5.1 $k-\epsilon$ model

The $k-\epsilon$ model is governed by partial differential equations for both the turbulent kinetic energy, k, and the turbulent dissipation rate, ϵ. Furthermore, an algebraic expression is needed in order to close the system of equations [7]. Based on the work by Prandtl (1945) and Kolmogorov (1942) the eddy-viscosity can be expressed as:

$$\mu_T = \rho C_\mu \frac{k^2}{\epsilon}, \quad \nu_t = \frac{\mu_t}{\rho} \tag{2.22}$$

The standard $k-\epsilon$ model in Fluent is based on the model by Launder and Spalding [44] and is given as:

$$\frac{\partial k}{\partial t} + \overline{u_j}\frac{\partial k}{\partial x_j} = \frac{\partial}{\partial x_j}\left[\left(\nu + \frac{\nu_T}{\sigma_k}\right)\frac{\partial k}{\partial x_j}\right] + P_k - \epsilon \tag{2.23}$$

$$\frac{\partial \epsilon}{\partial t} + \overline{u_j}\frac{\partial \epsilon}{\partial x_j} = \frac{\partial}{\partial x_j}\left[\left(\nu + \frac{\nu_T}{\sigma_\epsilon}\right)\frac{\partial \epsilon}{\partial x_j}\right] + \frac{\epsilon}{k}(C_{\epsilon 1}P_k - C_{\epsilon 2}\epsilon) \tag{2.24}$$

where P_k is the production term defined as:

$$P_k = 2\nu_T S_{ij}\frac{\partial \overline{u_i}}{\partial x_j} \tag{2.25}$$

and where $\sigma_k = 1.0$, $\sigma_\epsilon = 1.3$, $C_{\epsilon 1} = 1.44$, $C_{\epsilon 2} = 1.92$ and $C_\mu = 0.09$ are empirical constants. P_k represent the production of turbulent kinetic energy. The turbulence model, including equations 2.22 -2.24 together with the continuity equation and the momentum equation form a closed set of the governing equations which can be solved numerically with appropriate boundary conditions.

2.5.2 $k-\omega$ model

The $k-\omega$ model include one transport equation of k and one for the specific dissipation rate, ω. The transport equations for k and ω together with an algebraic expression for the turbulent viscosity close the system of equations. The algebraic expression for the turbulent viscosity is given as:

$$\nu_T = \frac{k}{\omega} \tag{2.26}$$

The standard $k-\omega$ model in Fluent is based on Wilcox suggested model [88]. The model has been improved by reducing the freestream sensitivity. The transport equations for the

$k-\omega$ model is given as:

$$\frac{\partial k}{\partial t}+\overline{u_j}\frac{\partial k}{\partial x_j}=2S_{ij}\frac{\partial \overline{u_i}}{\partial x_j}+\frac{\partial}{\partial x_j}\left[\left(\nu+\frac{\nu_T}{\sigma_k}\right)\frac{\partial k}{\partial x_j}\right]-\beta_k k\omega \tag{2.27}$$

$$\frac{\partial \omega}{\partial t}+\overline{u_j}\frac{\partial \omega}{\partial x_j}=2\alpha\nu_T S_{ij}\frac{\partial \overline{u_i}}{\partial x_j}+\frac{\partial}{\partial x_j}\left[\left(\nu+\frac{\nu_T}{\sigma_\omega}\right)\frac{\partial \omega}{\partial x_j}\right]-\beta_\omega\omega^2 \tag{2.28}$$

where $\sigma_k=2.0$, $\sigma_\omega=2.0$, $\beta_k=0.09$, $\beta_\omega=0.075$ and $\alpha=0.56$ are empirical constants in the model. It should be noted that the standard $k-\omega$ model in Fluent is implemented with low-Reynolds number correction. This correction is done by introducing dampening coefficients for the turbulent viscosity and the production of the specific dissipation rate. The details are given in depth in Wilcox [88] and Fluent User Guide [3].

2.5.3 $k-\omega$ SST model

The $k-\omega$ shear-stress transport model is an extension of the standard $k-\omega$ model developed by Menter [53]. As a result the model combines the advantages of the $k-\omega$ and the $k-\epsilon$ model. The transport of turbulent shear stress is obtained by applying a limiter to the eddy viscosity:

$$\nu_t=\frac{k}{\omega}\frac{1}{\max\left[\frac{1}{\alpha^*},\frac{SF_2}{a_1\omega}\right]} \tag{2.29}$$

where

$$F_2=tanh(\phi_2^2),\quad \phi_2=\max\left[\frac{2\sqrt{k}}{0.09\omega y},\frac{500\mu}{\rho y^2\omega}\right] \tag{2.30}$$

and S is the strain rate magnitude and y is the distance to the wall. The model constants are similar as for the standard $k-\omega$ model, described in the previous section.

2.6 Reynolds stress model

The Reynolds stress models are second order closure models and probably the most general of all classical turbulence models. In the two-equation models ($k-\epsilon$ and $k-\omega$) turbulence is represented by a scalar qunatity, k, the turbulent kinetic energy and are implicitly based on the assumption of local isotropy, i.e. $\overline{u'^2}=\overline{v'^2}=\overline{w'^2}$. This is usually not the case in real flows and the turbulence is thereby anisotropic. The RSMs is able to compute the anisotropic turbulence by abandoning the eddy-viscosity hypothesis. The closing of the RANS equations is done by solving transport equations for the individual Reynolds stress components:

$$-\overline{u_i' u_j'} = \begin{bmatrix} -\overline{u'u'} & -\overline{u'v'} & -\overline{u'w'} \\ -\overline{v'u'} & -\overline{v'v'} & -\overline{v'w'} \\ -\overline{w'u'} & -\overline{w'v'} & -\overline{w'w'} \end{bmatrix} \tag{2.31}$$

In two-dimensional problems, five transport equations have to be solved for the Reynolds stresses. As a result this approach is more computationally expensive and in addition no numerical stability from the eddy viscosity is gained. The RSM may be tuned by a parameter study.

2.6.1 Transport equations

The equation for the individual Reynolds stress may be derived from the equation for the fluctuating velocity. The transport equation implemented in Fluent is based on the model by Gibson and Launder [31] and is given as:

$$\underbrace{\frac{\partial}{\partial t}(\rho\overline{u_i' u_j'})}_{\substack{\text{Local time} \\ \text{derivative}}} + \underbrace{C_{ij}}_{\text{Convection}} = \underbrace{-D_{T,ij}}_{\substack{\text{Turbulent} \\ \text{diffusion}}} + \underbrace{D_{L,ij}}_{\substack{\text{Molecular} \\ \text{diffusion}}} \underbrace{-P_{ij}}_{\substack{\text{Stress} \\ \text{production}}} + \underbrace{\phi_{ij}}_{\substack{\text{Pressure} \\ \text{strain}}} - \underbrace{\epsilon_{ij}}_{\text{Dissipation}} \tag{2.32}$$

where

$$C_{ij} = \frac{\partial}{\partial x_k}(\rho u_k \overline{u_i' u_j'}) \tag{2.33}$$

$$D_{T,ij} \equiv -\frac{\partial}{\partial x_k}\left[\rho\overline{u_i' u_j' u_k'} + \overline{p'\left(\delta_{kj}u_i' + \delta_{ik}u_j'\right)}\right] \tag{2.34}$$

$$D_{L,ij} \equiv \frac{\partial}{\partial x_k}\left[\mu\frac{\partial}{\partial x_k}\left(\overline{u_i' u_j'}\right)\right] \tag{2.35}$$

$$P_{ij} \equiv -\rho\left(\overline{u_i' u_k'}\frac{\partial u_j}{\partial x_k} + \overline{u_j' u_k'}\frac{\partial u_i}{\partial x_k}\right) \tag{2.36}$$

$$\phi_{ij} \equiv \overline{p\left(\frac{\partial u_i'}{\partial x_j} + \frac{\partial u_j'}{\partial x_i}\right)} \tag{2.37}$$

$$\epsilon_{ij} \equiv 2\mu\overline{\frac{\partial u_i'}{\partial x_k}\frac{\partial u_j'}{\partial x_k}} \tag{2.38}$$

The turbulent diffusion $D_{T,ij}$, redistribution ϕ_{ij} and dissipation ϵ_{ij} need to be modelled in order to close equation 2.32.

Modelling turbulent diffusion

The turbulent diffusion term $D_{T,ij}$ may be modelled by a generalized gradient-diffusion model proposed by Daly and Harlow [24]. Due to numerical instabilities, the model in Fluent is

simplified and a isotropic model is implemented, where the turbulent viscosity is included, as suggested by Lien And Leschziner [48]:

$$D_{T,ij} = \frac{\partial}{\partial x_k}\left(\frac{\mu_t}{\sigma_k}\frac{\partial \overline{u_i' u_j'}}{x_k}\right) \tag{2.39}$$

where the Prandtl number for turbulence energy is $\sigma_k = 0.82$. Similarly, the turbulent viscosity μ_t is given by equation 2.22 in the $k-\epsilon$ model with $C_\mu = 0.09$.

Modelling redistribution

It may be demonstrated that the terms in ϕ_{ij} do not change the turbulent kinetic energy [7]. However, they tend to redistribute energy between different normal Reynolds stresses. Each normal components in ϕ_{ij}, i.e. ϕ_{11}, ϕ_{22} and ϕ_{33} may be nonzero, but the summation of the normal components is zero. A classical decomposition of the redistribution term is considered:

$$\phi_{ij} = \phi_{ij}^{slow} + \phi_{ij}^{rapid} + \phi_{ij}^{wall} \tag{2.40}$$

The slow part ϕ_{ij}^{slow} is known as the return-to-isotropy term and contains only turbulent velocities, resulting in decreasing anisotropy. In contrast, the rapid part ϕ_{ij}^{rapid} involve terms of the mean velocity gradients. The third part is the wall-reflection term and allow the redistribution of normal stresses near the wall.

The Linear Pressure-Strain model in Fluent is based on the model by Gibson and Launder [31] and Launder [46]. Equation 2.40 is modelled in Fluent as [2]:

$$\phi_{ij}^{slow} \equiv -C_1\rho\frac{\epsilon}{k}\left(\overline{u_i' u_j'} - \frac{2}{3}\delta_{ij}k\right) \tag{2.41}$$

$$\phi_{ij}^{rapid} \equiv -C_2\left(P_{ij} - C_{ij} - \frac{1}{3}\delta_{ij}(P_{kk} - C_{kk})\right) \tag{2.42}$$

$$\begin{aligned}\phi_{ij}^{wall} \equiv & C_1'\frac{\epsilon}{k}\left(\overline{u_k' u_m'}n_k n_m\delta_{ij} - \frac{3}{2}\overline{u_i' u_k'}n_i n_k\right)\frac{C_\mu^{3/4}k^{3/2}}{\kappa\epsilon d} \\ & + C_2'\left(\phi_{km}^{rapid}n_k n_m\delta_{ij} - \frac{3}{2}\phi_{ik}^{rapid}n_j n_k - \frac{3}{2}\phi_{jk}^{rapid}n_i n_k\right)\frac{C_\mu^{3/4}k^{3/2}}{\kappa\epsilon d}\end{aligned} \tag{2.43}$$

where C_{ij} and P_{ij} are defined in equations 2.33 and 2.36, respectively. Here, n_k is the x_k component of the unit normal to the wall and d is the normal distance to the wall, $\kappa = 0.4187$ is the von Kàrmàn constant and $C_\mu = 0.09$. In the derivation of equation 2.41 and 2.42 homogeneous turbulence is assumed, i.e. independent of position. In the vicinity of walls the

assumption of homogeneous turbulence is not valid and a modification of the model must be added. The modification in Fluent is implemented by setting the values of C_1, C_2, C_1' and C_2' as functions of the turbulent Reynolds number Re_t and the Reynolds stress invariants, as described by Launder and Shima [47]:

$$C_1 = 1 + 2.58BB_2^{1/4}\left(1 - exp[-(0.0067Re_t)^2]\right) \tag{2.44}$$

$$C_2 = 0.75\sqrt{B} \tag{2.45}$$

$$C_1' = -\frac{2}{3}C_1 + 1.67 \tag{2.46}$$

$$C_2' = max\left[\frac{\frac{2}{3}C_2 - \frac{1}{6}}{C_2}, 0\right] \tag{2.47}$$

$$Re_t = \frac{k^2}{\nu\epsilon} \tag{2.48}$$

The flatness parameter B and tensor invariants B_2 and B_3 are defined as

$$B \equiv 1 - \frac{9}{8}\left(B_2 - B_3\right) \tag{2.49}$$

$$B_2 \equiv b_{ik}b_{ki} \tag{2.50}$$

$$B_3 \equiv b_{ik}b_{kj}b_{ji} \tag{2.51}$$

Finally, the Reynolds-stress anisotropy b_{ij} tensor is defined as:

$$b_{ij} = \frac{\overline{u_i'u_j'} - \frac{2}{3}\delta_{ij}k}{k} \tag{2.52}$$

Modelling dissipation

A common approach is to consider the dissipation rate tensor ϵ_{ij} to be isotropic and one transport equation for the scalar dissipation rate ϵ. The dissipation of the Reynolds stresses in Fluent is modelled as:

$$\epsilon_{ij} = \frac{2}{3}\delta_{ij}\rho\epsilon \tag{2.53}$$

The assumption of an isotropic dissipation rate is valid for high Reynolds number flows, but anisotropy is more prominent for moderate Reynolds number [36]. The transport equation for the scalar dissipation rate is the same as in the $k - \epsilon$ model, defined in equation 2.24.

2.6.2 Algebraic stress model (ASM)

A simpler version of the Reynolds stress model is the algebraic stress model. This model allow a nonlinear relationship between the Reynolds stresses and the rate of the mean strain without solving the transport equations for the Reynolds stress components. In the ASM the Boussinesq assumption is not invoked directly as in the two-equations models. Instead, the constant turbulent viscosity in the two-equations models is replaced by a function. Nonlinear relationships between the Reynolds stresses and the rate of mean strain have been proposed by several researchers, e.g. Lumley [51] and Speziale [78]. There are many variations of the ASMs and two different approaches are given here. The first approach is a series expansion with the Boussinesq approximation as the lead term based on the work by Zhu et al. [91]. The second approach suggested by Rodi [70] is to deduce a nonlinear algebraic equation for the Reynolds stresses by simplifying the the transport equation for the individual Reynolds stress.

In this study the ASM is based on the $k-\epsilon$ model, and the the solution of the $k-\epsilon$ model is applied as an initial solution for the ASM simulations. The ASM implemented in ANSYS Fluent is a beta version and ANSYS were not able to provide documentation for the mathematical formulation. As a consequence, the formulation is not given. The results of the ASM should not be weighted in the same manner as the other turbulence models, as these are thoroughly documented.

2.7 Turbulent boundary layer

As both viscous and Reynolds stresses are included in the RANS equations, the importance of the stresses is investigated. Prandtl [64] proposed that there is an inner layer near the wall where the mean velocity is determined by viscosity. The no-slip condition at the wall result in negligible Reynolds stresses in the RANS equations and Prandtl's suggestion is valid. The linear region, which is the innermost region, is highly influenced by viscous stresses due to the large velocity gradient. This velocity gradient arises from the no-slip condition at the wall. Due to the low velocities in this region, the Reynolds stresses are of negligible magnitude. In order to determine where the viscous and the Reynolds stresses are dominating, wall coordinates are introduced:

$$y^+ = \frac{yu_\tau}{\nu}, \quad u_\tau = \sqrt{\frac{\tau_w}{\rho}}, \quad u^+ = \frac{\overline{u}}{u_\tau} \tag{2.54}$$

Using the inner variables for u and y described in equation 2.54, the relationship between velocity and distance from the wall is in the linear region is:

$$u^+ = y^+ \tag{2.55}$$

Further, the inner boundary layer is divided into three regions: the linear region, the buffer region and the logarithmic region. The logarithmic region, which is the outermost region in the inner layer, is mostly governed by the Reynolds stresses. Here, as opposed to the linear region, the viscous stresses can be neglected since the velocity gradient multiplied with the viscosity is of a much smaller order of magnitude than the Reynolds stresses. The logarithmic relationship between u^+ and y^+ can be described as

$$u^+ = Alog(y^+) + B \tag{2.56}$$

where A and B are constants determined by the flow. In between the linear and the logarithmic region, the buffer region is located. This is the most complex region in the inner layer, due to the fact that neither the viscous stresses nor the Reynolds stresses can be neglected, and simplification of the governing equation 2.11 is prevented. A visualization of the different regions with their respective models from equation 2.55 and 2.56 is shown in Figure 2.2.

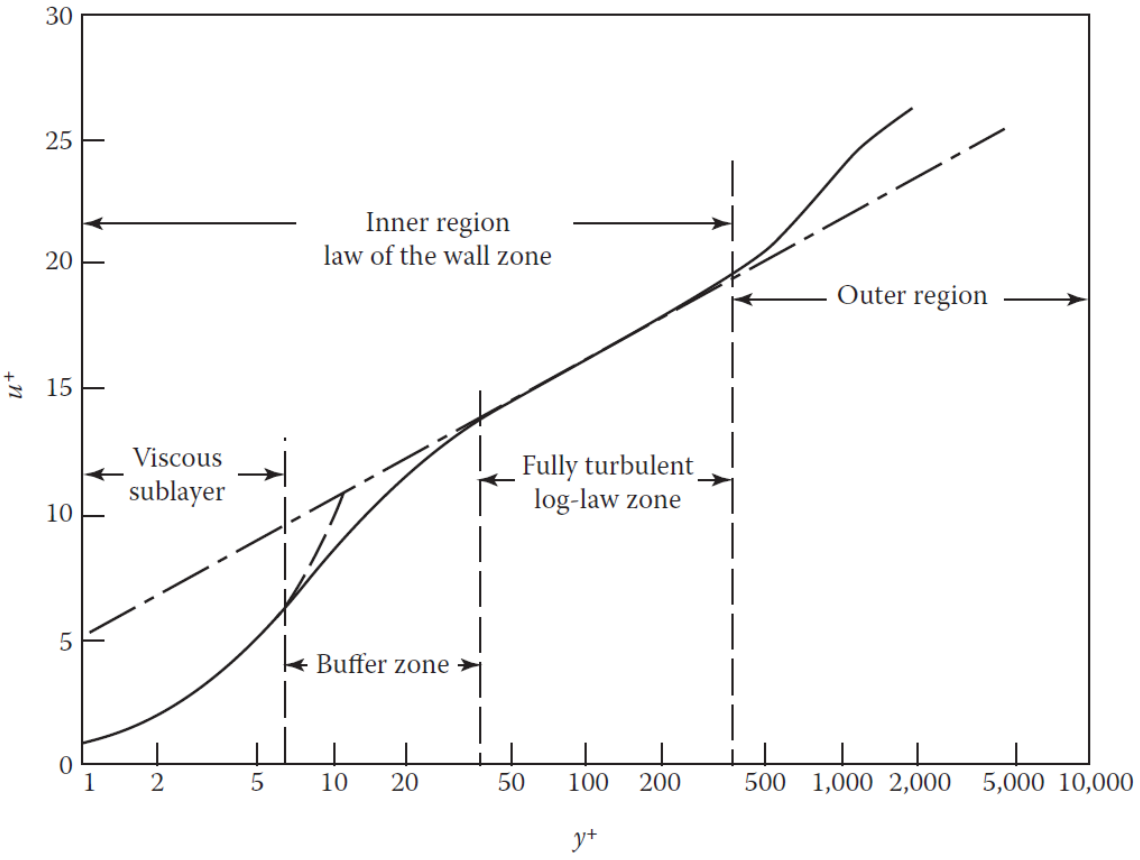

Figure 2.2 The different regions in a turbulent boundary layer for flow over a flat plate. The dashed lines represent the equation 2.55 and 2.56. Adapted from Pletcher [63].

2.8 Near wall treatment

The mean velocity field and the turbulence are significantly affected by the no-slip condition at the wall. In Fluent there are two approaches for the modelling the near-wall region. The first approach do not resolve the inner region but wall functions based on semi-empirical formulas are used. The second approach use modifications of the turbulence models in order to resolve the boundary layer.

2.8.1 Wall functions

As presented in section 2.7 the different layers is divided in three different regions, where the friction velocity u^+ is a function of y^+. By the use of wall functions the region affected by the viscosity is modelled. As the viscous sublayer and the buffer zone is not resolved a coarse mesh is applied when wall functions are used. This is beneficial in terms of computational time. On the other hand, these functions are not accurate for moderate Reynolds number flows and is difficult to apply to complex geometry [76].
In Ansys Fluent wall functions are implemented based on the work by Launder and Spalding [45]. The law-of-wall for the mean velocity is obtained from equation 2.56 with constants $A = \frac{1}{\kappa} = \frac{1}{0.4187}$ and $B = 5.45$. Further, Fluent recommend $y^+ > 30$ in the entire domain [3] For completeness, the law-of-the-wall for the mean velocity is based on the wall unit y^* instead of y^+. Fortunately, these quantities are approximately equal in equilibrium turbulent boundary layers.

2.8.2 Near-Wall model

The second approach resolve the viscous sublayer and the buffer layer using a two layer model for the $k-\epsilon$ model and the RSM, as well as the ASM. In Fluent this is called Enhanced Wall Treatment and based on the work by Chen and Patel [17]. Fluent recommend a structured grid in wall-normal direction and a value of unity for y^+ [3]. The model include modifications of the eddy viscosity and turbulent dissipation rate in the near wall region. A blending function is used to bridge the standard model equations and the new equations introduced. The blending function is dependent on a turbulent Reynolds number

$$Re_y = \frac{\rho y \sqrt{k}}{\mu} \tag{2.57}$$

where y is the distance normal to the wall. The fully turbulent region is defined as $Re_y > 200$ and the standard equations for the $k - \epsilon$ and the RSM are used. For turbulent Reynolds

number $Re_y < 200$ the eddy viscosity is obtained from the equation given by Wolfstein [89]:

$$\mu_{t,wall} = \rho C_\mu l_\mu \sqrt{k} \tag{2.58}$$

where the viscosity length scale l_μ is computed from

$$l_\mu = y C_l^* \left(1 - e^{-Re_y/A_\mu}\right) \tag{2.59}$$

Similarly, the equation for the turbulent dissipation rate ϵ is replaced by ϵ_{wall}:

$$\epsilon_{wall} = \frac{k^{3/2}}{l_\epsilon} \tag{2.60}$$

where the length scale for the dissipation l_ϵ given as

$$l_\epsilon = y C_l^* \left(1 - e^{-Re_y/A_\epsilon}\right). \tag{2.61}$$

Finally, the constants in equations 2.59 and 2.61 are:

$$C_l^* = \kappa C_\mu^{-3/4}, \quad A_\mu = 70, \quad A_\epsilon = 2C_l^* \tag{2.62}$$

2.9 Particle-laden flows

Particle-laden flows are classified in dilute, medium and dense flow regimes according to Varaksin [84]. The volume fraction is an important ratio in determining the correct flow regime of the particle-laden flow:

$$\alpha = \frac{V_s}{V_{cell}} \tag{2.63}$$

The ratio is based on solid volume, V_s, in a specific volume V_{cell}. Elghobashi [28] suggested a classification map of particle-laden flows based on the volume fraction and is given in Figure 2.3. The dilute regime is determined by a volume fraction, $\alpha > 10^{-6}$. In this region the coupling between the dispersed and continuous phase is characterised by one-way coupling. For one-way coupling the carrier fluid effect the particles, but the particles have a negligible effect on the continuous phase. In the medium regime, $10^{-6} < \alpha < 10^{-3}$, the particles have an influence on the turbulence and a two-way coupling is needed. The two way coupling are dependent on the ratio between particle reaction time, τ_P and the Kolmogorov time scale, τ_K from equation 2.13. The particle reaction time is approximated as Stokes flow around the particle so the time scale is given by

$$\tau_P = \frac{\rho_P {d_P}^2}{18\rho\nu} \tag{2.64}$$

In this medium regime small values of τ_P will enhance turbulence dissipation and larger values will enhance turbulence production. In dense particle regimes, $\alpha > 10^{-3}$, also particle-particle collisions must be considered, hence four-way coupling.

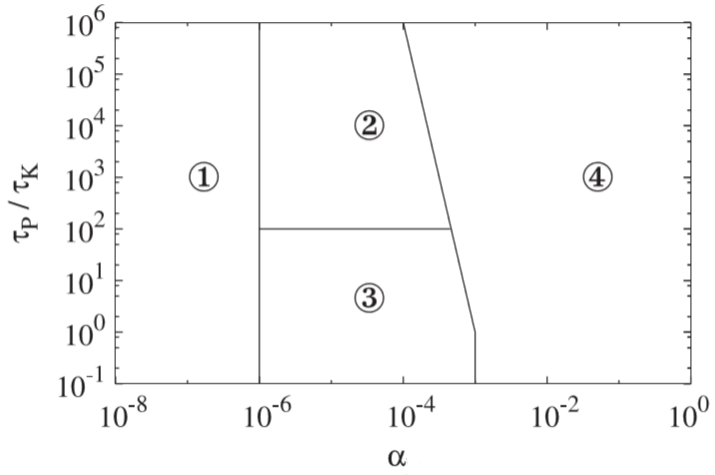

Figure 2.3 Particle-laden flow regimes, including coupling and turbulence effect. (1) one-way coupling, (2) & (3) two-way coupling, (4) four-way coupling. Adapted from [33].

2.9.1 Motion of Solid Particles

The motion of particles can be computed within the frame of the Lagrangian approach or the Eulerian continuum approach. Pletcher [63] state that the in Lagrangian approach the changes to the properties of a fluid element are recorded by an observer moving with the fluid element. A Lagrangian approach for the dispersed phase is done by tracking the particles through the continuous phase. A common method to simplify large number of particles is the point-particle approach. This method do not resolve the particle boundary layer and similar flow considerations on particle scale, instead these are empirically modelled. A relevant review of the point-particle methodology is the paper by Kuerten [52].

The Lagrangian equation of instantaneous motion of a single solid particle is given by:

$$\frac{d\mathbf{x_P}}{dt} = \mathbf{u_p} \tag{2.65}$$

$$m_P \frac{d\mathbf{u_P}}{dt} = \sum \mathbf{F_i} \tag{2.66}$$

where m_P is the particle mass, $\mathbf{x_P}$ is the position vector of the particle and $\mathbf{u_P}$ is the particle velocity. The right hand side of equation 2.66 represent the external forces acting on the particle. The dominating force factors are dependent on the flow problem.

Aerodynamic Drag Force

The influence from aerodynamic drag on the particle trajectory is the most dominant effect, according to Schellander [72]. Due to the difference in velocity for the fluid and the particle, the drag force causes acceleration or deceleration of the particle. Figure 2.4 show the fluid velocity, the particle velocity and the drag force for one particle. The particle is assumed to be spherical.

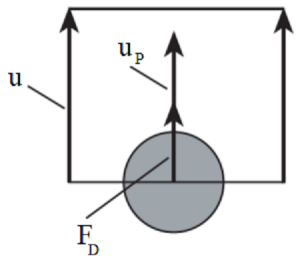

Figure 2.4 Particle motion under the effect of the aerodynamic drag force. Adapted from [84].

Assuming homogeneously distributed spherical particles with the same diameter, the drag

force is given by:

$$\mathbf{F_D} = C_D \rho \frac{\pi {d_P}^2}{4} (\overline{\mathbf{u}} - \mathbf{u_P}) |\overline{\mathbf{u}} - \mathbf{u_P}| \tag{2.67}$$

Where the drag coefficient, C_D, is dependent on the Reynolds number and flow regimes, described in 2.9. The standard drag curve is shown in Figure 2.5 where the Reynolds number is a function of the drag coefficient.

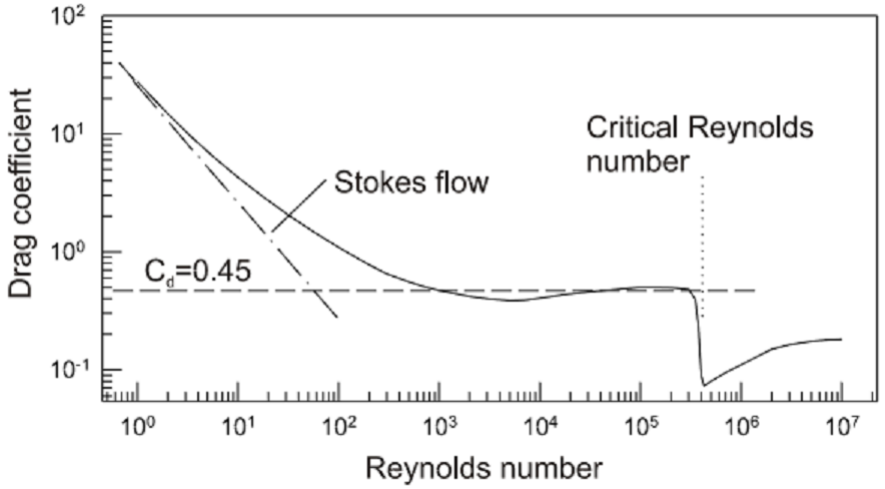

Figure 2.5 The drag coefficient of a sphere and Reynolds number, adapted from [21].

The literature states different empirical relations to describe the drag coefficient. The following correlations are based on recommendations by Crowe et. al. [21]. The Stokes flow regime, where the viscous forces dominate, is present for low Reynolds number, $Re_P < 1$. The Stokes formula is valid for creeping flow:

$$C_D = \frac{24}{Re_P}, \quad Re_P = \frac{|\overline{\mathbf{u}} - \mathbf{u_P}| d_p}{\nu} \tag{2.68}$$

In the inertial range, $750 < Re_P < 3.5 \times 10^5$ the drag coefficient is close to constant, $C_D = 0.445$. The drop in the drag coefficient at the critical Reynolds number ($Re_p \sim 3 \times 10^5$) is due to boundary effects. The boundary layer becomes turbulent and the separation point is moved backward, resulting in a reduced drag coefficient. In this report the Reynolds number based on particle diameter, Re_P, is low because of the particle diameter and small relative particle and fluid velocity.

The spherical drag law in ANSYS Fluent is based on the work by Morsi and Alexander [56]. The drag coefficient is modelled as:

$$C_D = a_1 + \frac{a_2}{Re_P} + \frac{a_3}{Re_P^2} \tag{2.69}$$

where a_1, a_2 and a_3 are constants over several ranges of the Reynolds number. The constants are given for all ranges in appendix A.

Body forces

The gravitational force, $\mathbf{F_G}$, is the product of particle mass and acceleration due to gravity.

$$\mathbf{F_G} = \rho_P \frac{\pi d_P^3}{6} \mathbf{g} \tag{2.70}$$

Buoyancy

The buoyancy force, $\mathbf{F_B}$, is the product of the fluid density, the volume of the particle and the gravitational acceleration.

$$\mathbf{F_B} = -\rho \frac{\pi d_P^3}{6} \mathbf{g} \tag{2.71}$$

Other forces that may influence the particle trajectory are the Basset term, Saffman lift and Magnus lift. These are terms are neglected because the ratio of the density for the particles to the fluid is more than 1000 and may be neglected according to Jin et al. [40]. Further information about the force terms are given by Crowe et al. [21]. To summarize, the right hand side of equation 2.66 can be written as:

$$\sum \mathbf{F_i} = \mathbf{F_D} + \mathbf{F_G} + \mathbf{F_B} \tag{2.72}$$

2.9.2 Turbulent dispersion of particles

Trajectories of particles are predicted using the mean fluid phase velocity. In order to account for the dispersion of particle due to turbulence the fluctuating gas flow velocity is needed. The RANS equations do not provide these fluctuations and a stochastic method is used to estimate the fluctuations. Here the discrete random walk (DRW) model in ANSYS Fluent, also known as the stochastic eddy life time, is applied. In this model the fluctuating velocity is obtained by a Gaussian distribution function as:

$$u' = \gamma \sqrt{\overline{u'^2}} \tag{2.73}$$

where γ is a normally distributed random number. The local root mean square value is calculated on the assumption of isotropic turbulence for the two equations models:

$$\sqrt{\overline{u'^2}} = \sqrt{\overline{v'^2}} = \sqrt{\overline{w'^2}} = \sqrt{\frac{2}{3}k} \tag{2.74}$$

Further, the characteristic eddy lifetime τ_e is the time scale the particle is assumed to interact with the continous phase eddy [65]. In this model the characteristic lifetime of the eddy is

defined as:

$$\tau_e = 0.3\frac{k}{\epsilon} \tag{2.75}$$

2.9.3 Stokes number

The Stokes number is an important dimensionless parameter and gives useful information about the behavior of particles suspended in a fluid flow. The Stokes number is defined as

$$St = \frac{\tau_P}{\tau_F} \tag{2.76}$$

where τ_P is the particle response time and τ_F is the time characteristic of the flow field. Stokes [80] found that for small particles with negligible Reynolds number the particle response time is

$$\tau_{P,Stokes} = \frac{(2\rho_P + \rho_F){d_P}^2}{36\mu} \tag{2.77}$$

A simplification of equation 2.77 when the fluid density is negligible, i.e. for solid particles in gaseous medium, equation 2.64 is obtained. As this time constant is only valid for low Reynolds number a correction for the drag coefficient can be used. This can be done my applying a Reynolds dependent drag coefficient, e.g. equation 2.69. For low Stokes number, $St << 1$, the particle response time is less than the characteristic time of the flow field. In this type of particle-laden flow the particles will have time to respond to velocity changes in the flow. As a result the velocity of particle and the fluid will be in equilibrium. In contrast, for higher Stokes number, i.e. $St >> 1$, the particle response time is larger than the characteristic time of the flow field and the fluid will only have a small effect on the particle velocity.

Chapter 3

Numerical Method

Computational Fluid Dynamics (CFD) is applied to the governing equations to obtain an approximate numerical solution. By discretization the aforementioned PDEs are reduced to a set of algebraic equations. Both time and space are discretized into small control volumes or cells. The continuous solution of the flow field is represented by the approximation of each cell. According to Ferziger [29], the components of a numerical method are:

- Mathematical model
- Discretization
- Coordinate and basis vector system
- Numerical grid
- Finite approximation
- Solution method
- Convergence criteria

3.1 Level of modelling

In numerical simulations the level of modelling need to be considered. The output of the simulation is dependent on the level of modelling. The choice is often limited because of computational power and time. Spalart [77] attempted to clarify and size up the levels of modelling for a numerical simulation of a complete airplane in turbulent flow.
Figure 3.1 give an overview of modelling particle-laden flows and the information abstracted from the simulation. When modelling large scale system an Eulerian-Eulerian model also called a two-fluid model is often preferred. This method model both the fluid and particles as a continuous fluid. Another approach is the Eulerian-Lagrangian where a discrete model

is applied for the particles. RANS, LES and DNS may be used for the continuous phase. The level of modelling is greatly dependent on the particle-laden flow regime, discussed in section 2.9, this will also be highlighted in the discussion of the results.
Vegendla et al. [85] conducted a numerical simulation of a dilute gas-solid flow and compared the Eulerian-Lagrangian and Eulerian-Eulerian approach to experimental data. The Eulerian-Eulerian simulation deviated considerably from the experimental data, while the Eulerian-Lagrangian method compared well with the experimental data. Vegendla et al. [85] explained the deviations are mainly due to the diffusive nature of the Eulerian-Eulerian method.

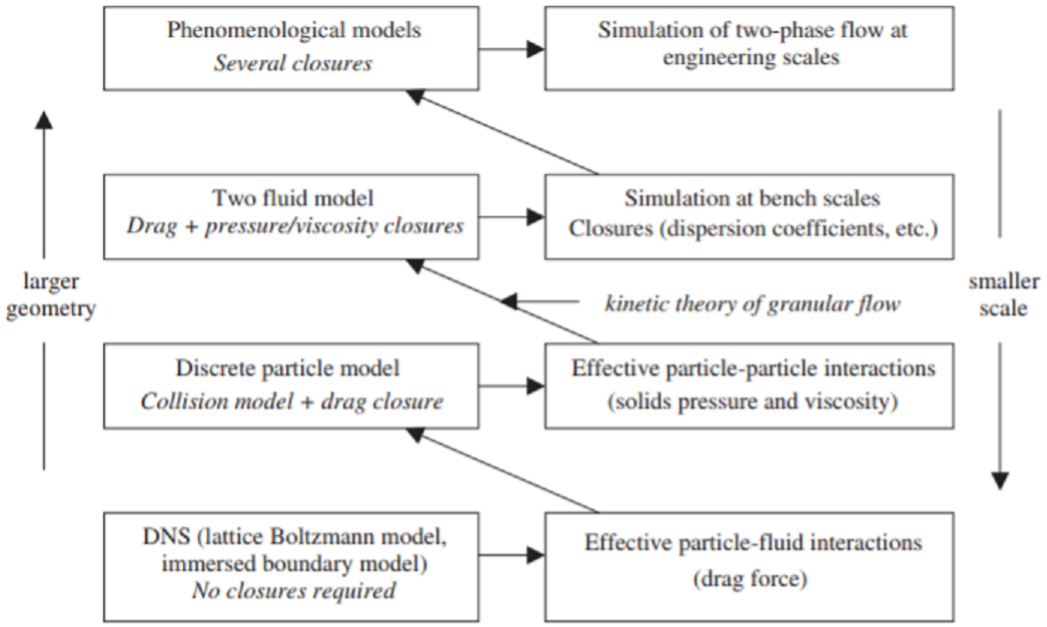

Figure 3.1 Modelling scheme of particle-laden flows, adapted from Deen et al. [26].

3.2 ANSYS Fluent

In the present study, the commercial CFD software ANSYS Fluent 19.2 is used. A wide range of turbulence models are implemented in Fluent. The presented $k-\epsilon$, $k-\omega$, $k-\omega$ SST, ASM and RSM in chapter 2 are applied. The two equations models were considered due to the simplicity and limited computational resources. However, the two equations models struggle to capture the effects of streamline curvature, flows with zones of recirculation and rotating flows [20]. This effect will be investigated in the first test case, i.e. turbulent flow in a concentric annulus. Then the obvious choice is to use the ASM formulation where anisotropy in the normal stresses is computed by algebraic expressions. Unfortunately, the ASM in Fluent is a beta version and not fully developed and validated. Therefore, ANSYS

was not able to provide documentation of the model and its mathematical formulation. As a result, the more complex turbulence modelling, i.e the RSM described in section 2.6, were considered. Firstly, the ϵ-based RSM is used. This is because the ω-based Reynolds stress models are not compatible with the Eulerian muliphase model in Fluent, thus not applicable for a future RSM model for the scrubber. Secondly, the linear pressure-strain model was chosen because the quadratic model by Speziale et al. [79] is only available with standard wall functions.

The discrete particle model (DPM) in Fluent is utilized for modelling particle-laden gas flows in this study. The model is a Euler-Lagrangian approach and the dispersed phase may exchange momentum, mass and energy with the continuous phase. The DPM is limited by a maximum volume fraction $\alpha = 0.1$. The equations of motion for particles given in section 2.9.1 are implemented in the DPM. One-way and two-way coupling between the dispersed and continuous phase are available within the DPM. In addition, the discrete random walk model for particle dispersion described in section 2.9.2 is used in the confined bluff body test case.

Three-dimensional and two-dimensional axisymmetric simulations were performed. The momentum equations for each velocity component, the Poisson equation for pressure and the transport equation for the turbulent variables were solved using ANSYS Fluent. The pressure-based coupled solver was used in all computations. The SIMPLE (Semi-Implicit Method for Pressure Linked Equations) scheme is used for the pressure equation and it is based on the work by Patankar and Spalding [61]. Further, the default second-order scheme for pressure was chosen. Gradients are discretized by the Least Square Cell Based scheme. The second order upwind scheme was applied for all other quantities. The relaxation factors were chosen based on recommendations by [3], hence the following relaxation factors for momentum and pressure are $\alpha_U = 0.7$ and $\alpha_P = 0.3$, respectively. A convergence criteria of 10^{-6} for the scaled residual for all variables was set.

The built-in processing tool CFD-Post in Fluent is used in processing data and for visualization. In addition, the Matlab software is used for data processing and to create various figures.

3.3 Initial and boundary conditions

3.3.1 Inlet and outlet

In order to have a correct physical modelling of the flow, boundary conditions are needed for velocities, pressure, turbulent kinetic energy, turbulent dissipation rate and turbulent

viscosity at the inlet and outlet. At the outlet zero gauge pressure is usually specified. The turbulent kinetic energy, k is given at the inlet by

$$k = \frac{3}{2}(U_b I)^2 \tag{3.1}$$

where I is the turbulent intensity and defined as the ratio of the root mean square of the velocity fluctuations to the bulk velocity. The turbulence intensity is given after the recommended equation [3]

$$I = 0.16(Re_{D_h})^{-1/8} \tag{3.2}$$

Further, the turbulent dissipation rate, ϵ is given at the inlet by

$$\epsilon = C_\mu^{3/4}\frac{k^{3/2}}{l} \tag{3.3}$$

where $C_\mu = 0.09$ is an empirical constant and the l is the turbulence length scale. The recommended approximation of the turbulence length scale is used:

$$l = 0.07D_h \tag{3.4}$$

When the $k-\omega$ model is applied, an initial condition for turbulent dissipation rate is needed. The turbulent dissipation rate is determined by:

$$\omega = \frac{k^{1/2}}{C_\mu^{1/4} l} \tag{3.5}$$

Finally the eddy-viscosity is obtained from equation 2.22 and 2.26 in section 2.4 for the $k-\epsilon$ and $k-\omega$ model, respectively.
Reynolds stresses need to be specified when using the Reynolds stress model. The initial turbulence is assumed to be isotropic for initial conditions:

$$\overline{u_i' u_j'} = 0 \tag{3.6}$$

and the normal stresses are determined by

$$\overline{u_k' u_k'} = \frac{2}{3}k \tag{3.7}$$

3.3.2 Walls

The no-slip condition is applied for solid walls and will result in a boundary layer near the walls. The boundary layer theory were presented in 2.7 and subsequently wall modelling.

Boundary condition for the turbulent kinetic energy k imposed at the wall is

$$\frac{\partial k}{\partial n} = 0 \tag{3.8}$$

where n is local normal to the wall. However, the boundary conditions for the solution variables are set according to wall functions both for standard wall functions and enchanced wall treatment [3].

3.4 Mesh

The mesh is a result of the discretization of the domain. The governing equations must hold for all cells. A wide range of meshes have been suggested to satisfy an accurate discretization. The main differences are geometry and topology in different mesh types. In general, meshes are divided into two categories, structured and unstructured grid system. Examples of a structured grid and an unstructured grid is shown in Figure 3.2. Structured mesh has advantages in coding and efficiency because of its simplicity. The structured mesh follows a structured indices convention. As a result the structured mesh system require less computer memory. In contrast, additional topological information is needed for unstructured mesh, which add complexity according to Moukalled [57]. This is because the cells are arranged arbitrary. The flexibility in fitting a domain with a complicated geometry is where the unstructured mesh is superior to the structured mesh, according to Bern et al. [13]. In this study all meshes are constructed using ANSYS Fluent Meshing. The meshes used in the three cases are presented within the related chapters.

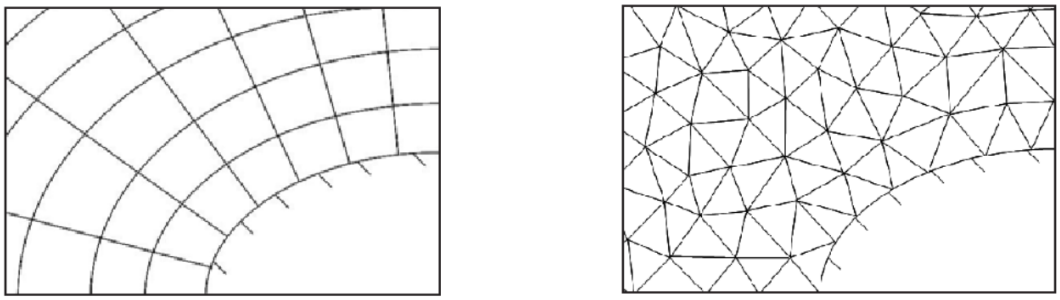

(a) Structured mesh (b) Unstructured mesh

Figure 3.2 Mesh types, adapted from [75].

Chapter 4

Concentric Annulus

The first test case in this study is turbulent flow in a concentric annulus. This test case is considered because the same flow is present in the venturi scrubber. Flow in concentric annulus is encountered in many engineering problems such as heat exchangers and drilling operations in the oil and gas industry. Fully developed turbulent flow in a concentric annulus is more complex than pipe flow due to nonlinear radial variation of total shear stress. Among researchers there is a discussion of whether the position of maximum and zero shear stress coincide at the same location. Rehme [66] experimentally investigated the flow with hot-wire anemometry and found non-coincidence between zero shear stress and maximum velocity. Kjellstrøm and Hedberg [42] showed by a theoretical analysis that the assumption of zero shear and maximum velocity are coincident is not necessarily true. However, experiments by Kjellstrøm and Hedberg [42] showed no difference. Nouri et al. [59] conducted measurements by the use of LDA in a fully developed concentric annulus flow at $Re_{D_h} = 8900$. Chung et al. [18] performed a direct numerical simulation with the radius ratio of 0.1 and 0.5 and Reynolds number, $Re_{D_h} = 8900$ of a concentric annulus flow and found no coincident. Chung et al. [18] made comparisons to the experimental data by Nouri et al. [59].

However, Boersma & Breugem [14] investigated turbulent flow in a concentric annulus by means of direct numerical simulation (DNS) and concluded that the radial position for the maximum axial velocity is the same as the position where the Reynolds shear stress is zero. According to Boersma & Breugem [14] the discussion is important as the eddy viscosity model would be invalid for the non-coincident case. Gretler and Meile [34] stated that the standard eddy-viscosity hypothesis yields good results in most engineering problems, but fails to predict the shear stress distribution in asymmetric turbulent flows in the vicinity of the maximum velocity. Azouz and Shirazi [8] evaluated several turbulence models for turbulent flow in concentric annulus and reported good agreement with the available experimental data. More recently, new measurement techniques have been applied. Corredor et al [71] investigated turbulent flow in a concentric annular geometry using high resolution particle

image velocimetry (PIV). Radial position of zero shear stress and maximum velocity where found to be slightly (2%) different. Xiong et al. [90] conducted a RANS based numerical analysis and compared the results to experimental and numerical data. Furthermore, all investigations of flow in concentric annulus a asymmetric velocity profile, tilting toward the inner wall, is found. In the literature study it is found that the position of the maximum velocity is less dependent on the Reynolds number than the radius ratio.

In this study the goal is to identify differences between different turbulence models, types of grids, near wall treatment and validation of simulations by experimental and numerical data available in the literature. This serve as a first test case of the later numerical analysis of the venturi scrubber. The concentric annulus is chosen because similar geometry is present in the venturi scrubber. In addition, the pressure drop in the scrubber is strongly dependent on the turbulence in a annulus flow. Firstly, from Moody's diagram an increase in the Reynolds number result in a decreased friction factor and subsequently the pressure drop. Secondly, the Reynolds stress is greater for an higher Reynolds number flow and cause an increase in the pressure drop.

4.1 Case description

The flow in a concentric annulus is confined by an inner and outer wall and the geometry is shown in Figure 4.1. Simulations were performed at three Reynolds numbers $Re_{D_h} = 8900, 38700, 56400$ based on the hydraulic diameter, $D_h = 2(R_2 - R_1)$. Parameters of the annulus are listed in Table 4.1, e.g. the radius ratio $\theta = R_1/R_2$. A two-dimensional axisymmetric geometry were considered, due to less computational cost compared to a full three-dimensional geometry.

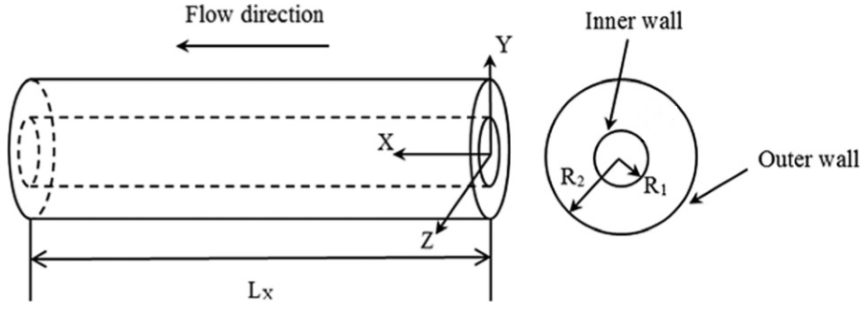

Figure 4.1 Geometry of concentric annulus, adapted from [90].

Table 4.1 Annulus parameters

Fluid	Water		
Density	998.2 kg/m^3		
Kinematic viscosity, ν	$1.005 \cdot 10^{-6}$ m^2/s		
Reynolds number, Re_{D_h}	8900	38700	56400
Hydraulic diameter , D_h	0.038 m	0.057 m	0.057 m
Length, L_x	2 m	2, 3.5 m	2, 3.5 m
Radius ratio, θ	0.5	0.4	0.4
Bulk velocity, U_b	0.2353 m/s	0.6822 m/s	0.9942 m/s

4.2 Numerical setup

Investigation of the turbulent flow in the concentric annulus is based on the RANS equations, described in section 2.3. Steady-state simulations with several turbulence models were performed. Wall functions were applied for the $k-\epsilon$, $k-\omega$ and $k-\omega$ SST model. In addition, the viscous sublayer were resolved using $k-\omega$ SST, ASM and RSM. The $k-\epsilon$ solution was used as an initial solution for both the ASM and RSM computations for faster convergence [3]. Initial and boundary conditions described in section 3.3 are considered. At the inlet a uniform velocity profile is given by the bulk velocity U_b, see Table 4.1.

4.3 Mesh

The mesh type is structured and two-dimensional in all computations. Two different mesh were considered, mesh A and mesh B. The length of the computational domain is 3.5 m for mesh A. Mesh A is defined by 105000 cells and stretched in both x- and y-direction. The mesh is refined in the centre in order to determine the position of the maximum velocity. Standard wall functions are considered for mesh A and the wall adjacent cell size ensure $y^+ > 30$ as recommended by Fluent [2].

As fully developed flow is considered the maximum streamwise velocity were monitored for $x = 3.5m$ and $x = 2.0m$. The obtained difference for the maximum streamwise velocity was 0.01 %. As a result the length of the computational domain for mesh B is 2m. Further, Mesh B is constructed to resolve the near wall boundary layer and is defined by 180000 quadrical cells. The grid is stretched in the y-direction to allow smaller cells in near-wall region. A grid convergence study for mesh B is presented in section 4.4.3.

Mesh B is used for Reynolds number in the range $Re_{D_h} = 8900 - 56400$. The velocity gradients are greater for higher Reynolds number flows. Thus, there are fewer cells in the viscosity-affected region for the higher Reynolds number flows. The wall coordinate y^+ is

shown in Figure 4.2. Increased values of y^+ are computed for higher Reynolds numbers, but is acceptable as $y^+ < 4$ according to the Fluent [3]. Precursor computation were performed for $Re_{D_h} = 56400$ to ensure $y^+ \approx 1$. A fully developed velocity profile and turbulent quantities, from a similar annulus flow, were applied as the inlet conditions.

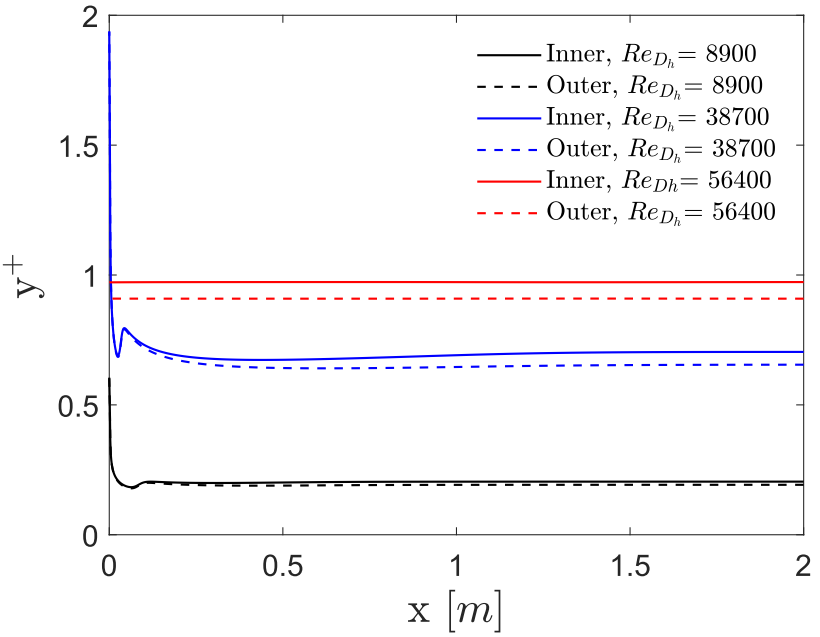

Figure 4.2 Values of y^+ for mesh B for $k-\omega$ SST simulations.

4.4 Results and discussion

4.4.1 Overview simulations and literature

Several simulations for different Reynolds number, mesh type and radius ratios have been performed and an overview of the simulations is given in Table 4.2. A radius ratio $\theta = 0.4$ is considered for all simulations except for $Re_{D_h} = 8900$.

Table 4.2 Overview of simulations

Turbulence model	Mesh	Re_{D_h}	$\theta = R_1/R_2$
$k-\epsilon$	A	38700, 56400	0.4
$k-\omega$	A	38700, 56400	0.4
$k-\omega\ SST$	A, B	8900, 38700, 56400	0.5, 0.4
ASM	B	37800, 56400	0.4
RSM	B	8900, 37800	0.5, 0.4

4.4.2 Validation

The Reynolds numbers and radius ratios are chosen in terms of relevance to the later investigation of the scrubber in chapter 6. Further, data from the literature is available for these parameters and the literature is presented in Table 4.3.

Table 4.3 Overview of literature for comparison

Author	Type	Re_{D_h}	$\theta = R_1/R_2$
Chung et al.	Numerical, DNS	8900	0.5
Corredor et al.	Experimental, PIV	38700, 56400	0.4
Nouri et al	Experimental, LDA	8900	0.5
Japper-Jaafar et al.	Experimental, LDA	30600, 61400	0.506
Bizhani et al.	Experimental, PIV	57000	0.4
Xiong et al.	Numerical, RANS	38700	0.4

As a first validation a simple force balance is considered. Newton's second law simplify to $\sum F = 0$ for fully developed and steady state flow. The force balance is

$$\Sigma F_x = \int (P_{in} - P_{out}) dA - \int_0^L (\tau_{inner} + \tau_{outer}) dx = 0 \tag{4.1}$$

where pressure forces and forces due to the shear stress are considered. The control volume analysis is given in Appendix C. The error for this simple force balance is within 3% for all simulations.

The skin friction coefficient defined as $C_f = \frac{\tau_W}{\frac{1}{2}\rho U_b^2}$ is shown in Table 4.4 for radius ratio $\theta = 0.4$ and $Re_{D_h} = 387000$. Here, the fine mesh, i.e mesh B, simulations computed an overall greater skin friction coefficient compared to the simulations obtained with mesh B and the experimental data.

Table 4.4 Skin friction coefficient, $Re_{D_h} = 38700$

	$C_{f,i}$, Inner	$C_{f,o}$, Outer
Corredor et al.	0.0062	0.0054
Xiong et al.	0.0065	0.0056
$k-\epsilon$ Mesh A	0.0061	0.0055
$k-\omega$ Mesh A	0.0066	0.0058
$k-\omega$ SST Mesh A	0.0066	0.0057
$k-\omega$ SST Mesh B	0.0069	0.0060
ASM Mesh B	0.0068	0.0059
RSM Mesh B	0.0068	0.0060

Nouri et al. [59] developed an expression for the average skin friction coefficient in the annulus based on a least square fit for Reynolds numbers from 4000 to 30000. The expression by Nouri et al. [59] is

$$C_{f,avg} = 0.36 Re_{D_h}^{-0.39} \tag{4.2}$$

and for $Re_{D_h} = 38700$ the value is 0.0058. The computed average skin friction coefficient is estimated as $C_{f,avg} = \frac{R_1}{R_1+R_2} C_{f,i} + \frac{R_2}{R-1+R_2} C_{f,o}$ and is equal to 0.0057 and 0.0062 for the $k-\epsilon$ and RSM simulation respectively.

4.4.3 Mesh convergence

A mesh convergence test was conducted to investigate the solution sensitivity in terms of grid resolution. Here, mesh B is considered at $Re_{D_h} = 38700$ with the $k-\omega$ SST model. The presented approach is based on the work by Roache [69]. Three different grid resolutions are tested: fine (1), medium (2) and coarse (3). The refinement ratio, r_g, between each step in the refinement process is set to 1.5. When refining the mesh special considerations are needed regarding the clustering and stretching of the elements in the mesh. This is an unwanted consequence that can occur when refining the mesh and will lead to a reduced overall quality. In example the aspect ratio will increase for mesh refinement only in one direction. For comparing the different resolutions, the maximum streamwise velocity in the middle of the annulus $\overline{u}_{x,m}$ and the average wall shear stress $\tau_{W,avg}$ of the inner and outer wall are monitored. The grid convergence shows how much the solution is affected by the grid refinement. This can be used to evaluate the choice of grid resolution for later computations. The grid convergence process show that there is a difference for the ratio $\overline{u}_{x,m}/U_b$ and the average skin friction coefficient, $\tau_{W,avg}$ for the different meshes. A summary of parameters in

the grid refinement procedure is given in Table 4.5, where N_x and N_y are the number of cells in the streamwise and radial direction. In addition, the wall coordinate y^+ is given for the inner and outer wall.

Table 4.5 Grid refinement

Mesh	N_x	N_y	N_{tot}	$\overline{u}_{x,m}/U_b$	$\tau_{W,avg}$	y_i^+	y_o^+
Coarse	160	500	80000	1.12368	2.45064	1.05	0.98
Medium	240	740	180000	1.12344	2.46029	0.74	0.65
Fine	360	1125	405000	1.12332	2.46180	0.47	0.44

Following the procedure suggested by Roache [69] the order of grid convergence is $p_{grid} = 1.8$, based on the maximum streamwise velocity $\overline{u}_{x,m}$. The grid convergence index (GCI) is a standardized parameter to determine grid convergence quality and is given by

$$GCI = \frac{F_s|e|}{r_g^{p_{grid}} - 1} \tag{4.3}$$

where e is the error between two grids and F_S is a safety factor. The value $F_s = 1.25$ suggested by Roache [69] is used. At the medium refinement level the grid convergence index is $GCI_{2,3} = 0.03\%$, while $GCI_{1,2} = 0.01\%$ at the last refinement level. In addition, it is needed to check that a asymptotic range of convergence is achieved. The asymptotic range is achieved if

$$GCI_{2,3} \simeq r^p GCI_{1,3} \tag{4.4}$$

As $\frac{GCI_{2,3}}{r_g^p GCI_{1,2}} = 0.9999$ the asymptotic range of convergence is achieved. However, a mesh independent solution is not obtained because of a change in the maximum velocity. A fine mesh compared to the medium mesh introduce extra computational time. Therefore, the medium mesh is chosen for the later computations.

4.4.4 Axial velocity

At first, solutions obtained with mesh B for $k-\omega\ SST$, ASM and RSM are presented. The axial mean velocity in wall coordinates for the inner and outer wall is given in the figures 4.3, 4.4 and 4.5 at $Re_{D_h} = 8900$, 38700 and 56400 respectively. The velocity profile obtained from the experimental data by Nouri et al. [59] and Corredor et al. [71] in addition to the numerical simulations follows the universal wall law. In the logarithmic layer ($y^+ > 30$) the numerical and experimental data are similar to the values computed by equation 2.56 which is the log law. The constants $A = 2.5$ and $B = 5.5$ in equation 2.56 are considered and are described in detail by Eggels et al. [27]. Numerical results is in better agreement with the proposed law of the wall for increased Reynolds numbers. The velocity profile obtained by $k-\omega\ SST$ at $Re_{D_h} = 8900$ is slightly lower than the proposed logarithmic equation, while good agreement is obtained by the RSM compared to the experimental data by Nouri et al. [59].

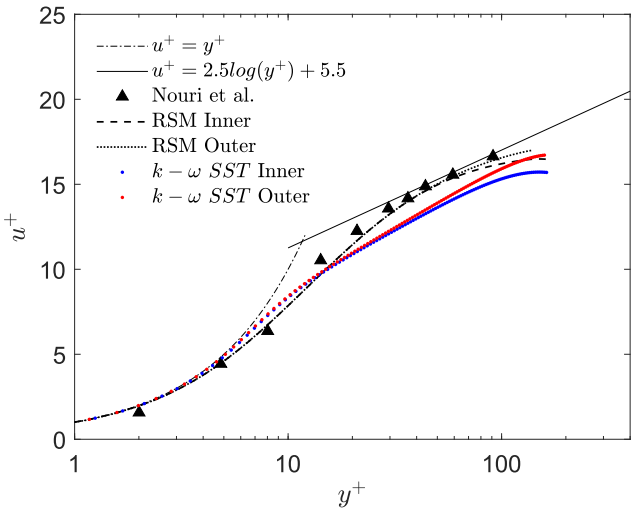

Figure 4.3 Axial velocity at the wall $Re_{D_h} = 8900$.

The experimental data by Corredor et al. [71] have slightly higher values in both the viscous sublayer and logarithmic layer in Figure 4.4. The velocities near the outer pipe wall in the logarithmic layer is higher compared to the velocities near the inner pipe wall. This discrepancy is consistent with the literature [18], [14] and it is due to the curvature effect.

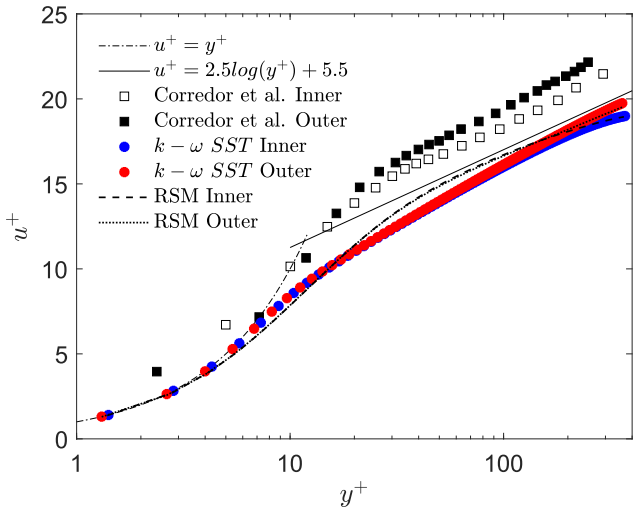

Figure 4.4 Axial velocity at the wall $Re_{D_h} = 38700$.

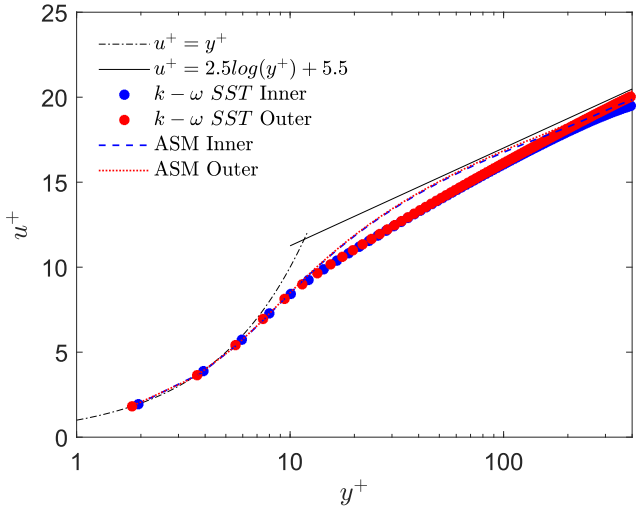

Figure 4.5 Axial velocity at the wall $Re_{D_h} = 56400$.

The mean streamwise velocity profile is shown in figures 4.6, 4.7 and 4.8 for the three different Reynolds numbers. Here, the simulations of both mesh A and B are presented. Normalization by the bulk velocity, U_b were performed. In addition, the dimensionless distance from the inner wall, $\xi = (y - R_1)/(R_2 - R_1)$ is used. The computed velocity profile is asymmetric and the position of the maximum velocity is closer to the inner pipe wall and similar results are reported in the literature [18], [14], [39], [66]. The experimental data by Nouri [59] in Figure 4.6 is rescaled as integration of the measured profiles in the radial direction did not yield a value of unity. This was reported by Chung et al. [18] and Azouz & Shirazi [8] and the rescaled values of Chung et al. [18] are given in Figure 4.6. Both RSM and $k - \omega$ SST simulations are in agreement with the DNS by Chung [18] and the rescaled experimental data by Nouri [59].

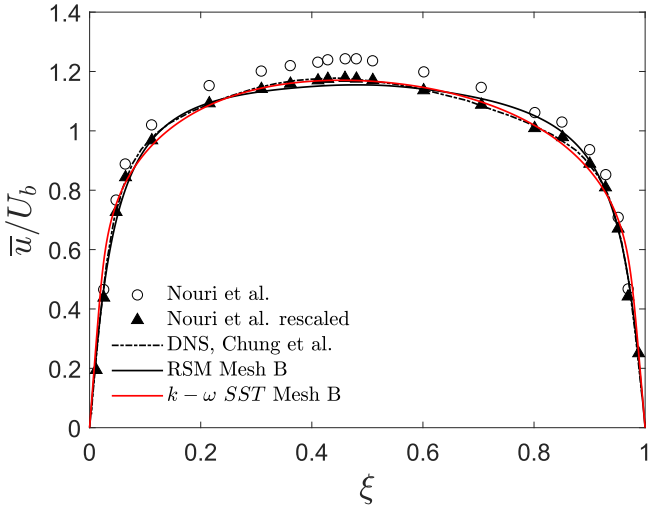

Figure 4.6 Axial mean velocity at $Re_{D_h} = 8900$.

A difference between computed and experimental data by Corredor [71] profile is clearly visible in Figures 4.7 and 4.8, but better agreement is obtained with the experimental data by Japper-Jafafar et al. [39]. However, Japper-Jaafar et al. [39] performed experiments at $Re_{D_h} = 30600$ and 61400 and a radius ratio, $\theta = 0.506$ as summarized in Table 4.3. The maximum velocity to bulk velocity, u_{max}/U_b was found to lower at higher Reynolds number by Corredor et al. [71] and Japper-Jaafar [39]. In Figure 4.7 the position of the maximum velocity is shifted closer to the inner wall as the radius ratio θ is decreased and this is also reported by Chung et al. [18], Xiong et al. [90] and Boersma & Breugem [14]. The velocity profile in Figure 4.8 is slightly flatter due to an increased Reynolds number compared to Figure 4.7.

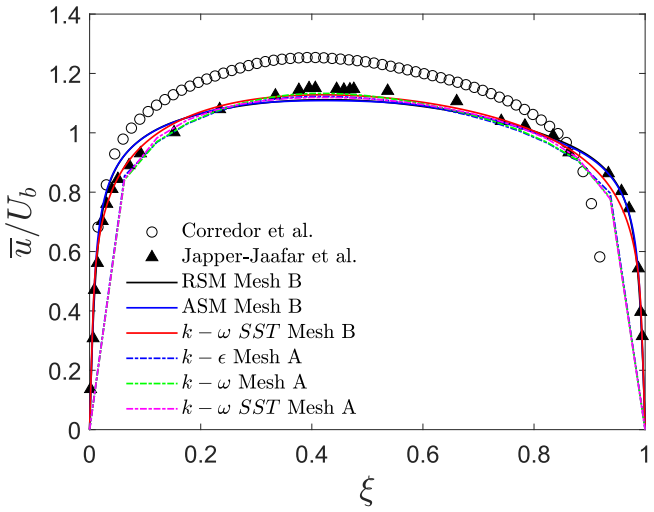

Figure 4.7 Axial mean velocity at $Re_{D_h} = 38700$. Note: Japper-Jaafar at $Re_{D_h} = 30600$, $\theta = 0.5$

In the near wall regions the computed velocity profile from the three different turbulence models, $k-\epsilon$, $k-\omega$ and $k-\omega$ SST with Mesh A, deviations from the experimental and the fine mesh computations are visible in Figures 4.7 and 4.8. Here, the limitations of the wall functions described in section 2.8.1 are prominent.

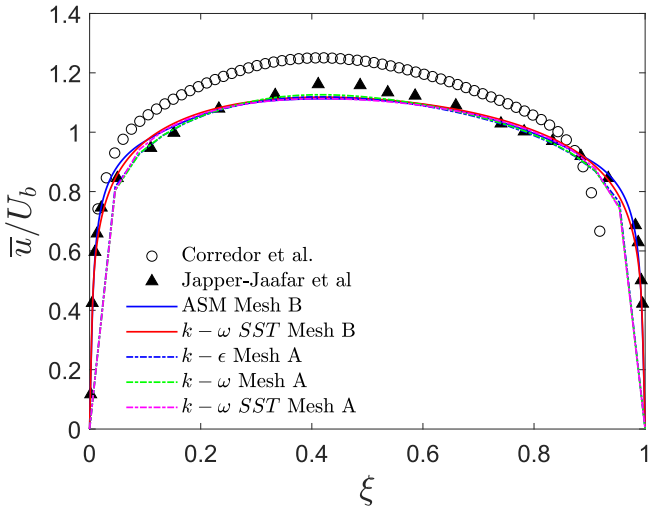

Figure 4.8 Axial mean velocity at $Re_{D_h} = 56400$. Note: Japper-Jaafar at $Re_{D_h} = 61400$, $\theta = 0.5$.

4.4.5 Turbulence intensity

The root mean square (rms) of the fluctuating velocities are regarded as a good measure of the turbulent intensity. For the RSM computations the rms of the fluctuating velocities are recovered from the Reynolds stresses, e.g. $u'_{rms} = \sqrt{\overline{u'u'}}$. The rms velocities in the axial, radial and tangential direction computed by the RSM at $Re_{D_h} = 8900$ and $\theta = 0.5$ are given in Figure 4.9. Here, the fluctuation velocities are normalized by the bulk velocity U_b. The anisotropy is clearly visible, i.e. $\overline{u'u'} \neq \overline{v'v'} \neq \overline{w'w'}$. The behaviour of the fluctuation velocities is as expected with a decrease in magnitude from axial, to tangential, to radial components. An overall agreement is obtained with the experimental values of Nouri et al. [59].

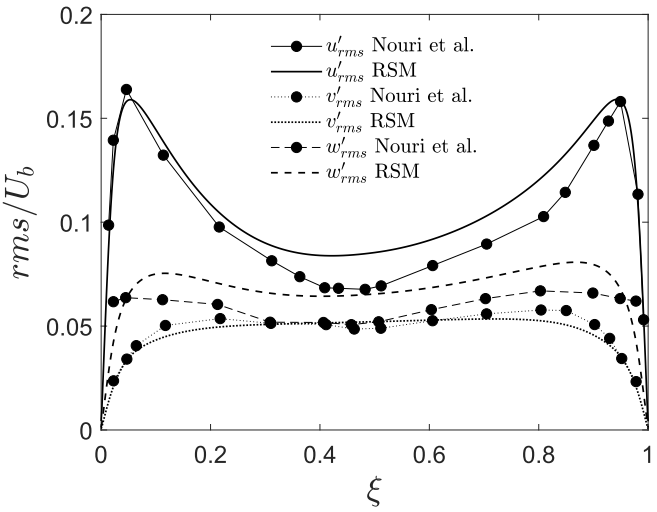

Figure 4.9 Rms of fluctuation velocities at $Re_{D_h} = 8900$.

A comparison of the fluctuation velocities computed by the RSM and ASM at $Re_{D_h} = 38700$ and $\theta = 0.4$ is shown in Figure 4.10. The tangential component w'_{rms} is computed quite similarly by the two turbulence models. However, greater anisotropy is computed by the RSM. As the Reynolds number is increased the fluctuating velocities peak closer to the wall. In Figure 4.10 the peak values are greater at the inner wall than at the outer wall and this is also reported by Liu & Lu [49]. Note the the ASM computed the same value for all the fluctuation velocities at approximately $\xi = 0.45$.

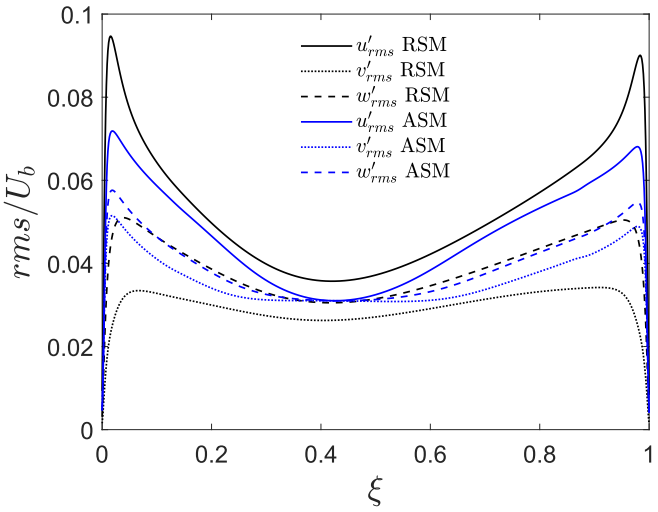

Figure 4.10 Rms of fluctuation velocities at $Re_{D_h} = 38700$.

The rms of the fluctuating velocities in wall coordinates close to the inner and outer wall are given in Figures 4.11a, b, c, d, e, f at $Re_{D_h} = 38700$. The velocities are nondimensionalized by the local friction velocity u_τ, note that the friction velocity at the inner wall is greater than at the outer wall as presented in terms of the skin friction coefficient in Table 4.4. The fine mesh, i.e. mesh B, is used for the RSM, ASM and $k-\omega$ SST model, while mesh A is used for $k-\epsilon$ model. As the two-equations models assume isotropic turbulence, the rms values are computed from the turbulent kinetic as $u'_{rms} = v'_{rms} = w'_{rms} = \sqrt{\frac{2}{3}k}$. The assumption of isotropic turbulence for the $k-\omega SST$ and the $k-\epsilon$ model is shown by comparing the axial and radial velocity fluctuations at the inner wall, e.g. see Figure 4.11c and 4.11e. The two profiles of the velocity fluctuations are identical. In contrast, the ASM and the RSM are capable of estimating the anisotropy of the turbulence. In addition, experimental data by Corredor et al. [71] and Japper-Jaafar et al. [39] are included. Firstly, the rms values are higher near the outer wall compared to the inner wall and is more prominent in the axial direction. The smaller rms values near the inner wall is due to the small surface area at the inner wall to support turbulent energy. This transverse curvature effect is reported by Chung et al. [18]. Secondly, the limitations of the wall functions are visible in all figures for simulations with the $k-\epsilon$ and mesh A. Thirdly, a tendency in the $k-\omega$ SST simulations is that the peak values are closer to the wall than the computations with the RSM.

In Figure 4.11b the maximum value of the normalized axial velocity fluctuations computed by the RSM simulation is 2.41, while Japper-Jaafar and Corredor measured 2.86 and 2.46 respectively. The DNS by Boersma & Breugem [14] computed the maximum to 2.7 and is consistent with the survey of the streamwise velocity fluctuations in wall bounded flows by Mochizuki & Nieuwstadt [55]. Location of peak values for the experimental data is within the buffer layer between 10 and 15 wall units. The $k-\omega$ SST and the $k-\epsilon$ model underestimate

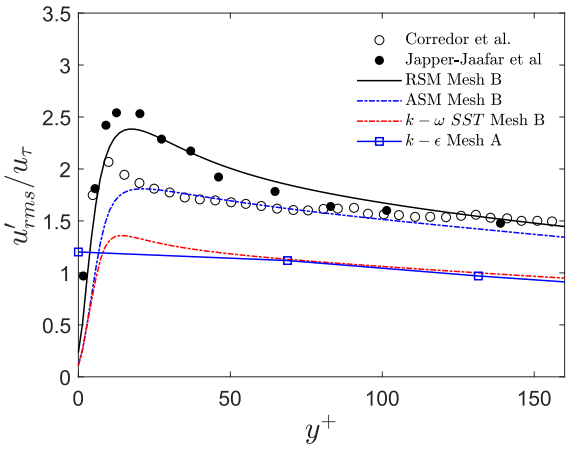

(a) Inner wall

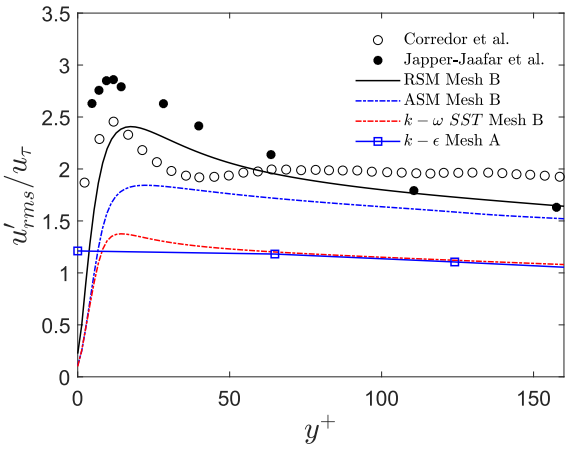

(b) Outer wall

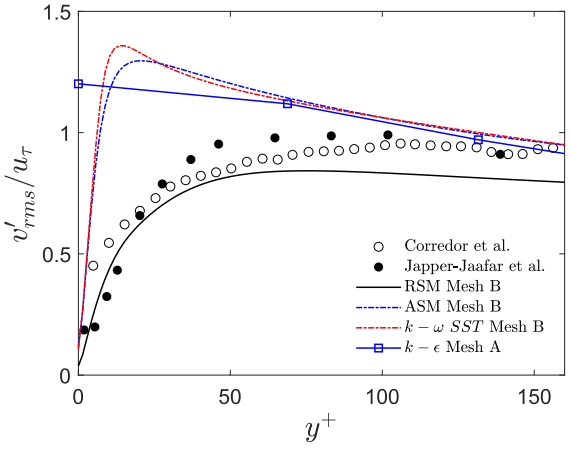

(c) Inner wall

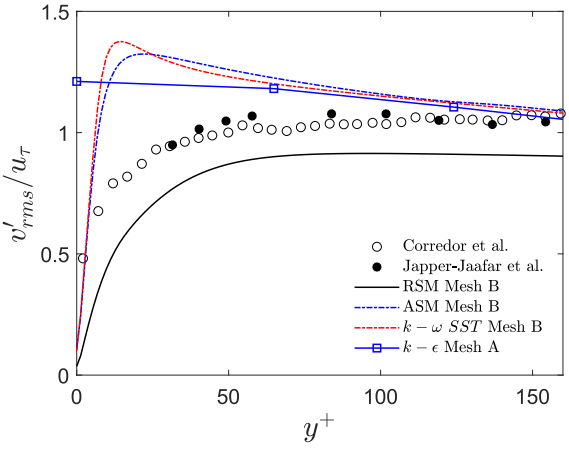

(d) Outer wall

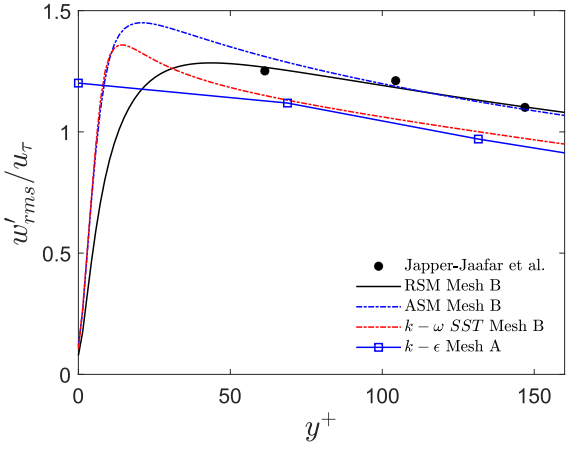

(e) Inner wall

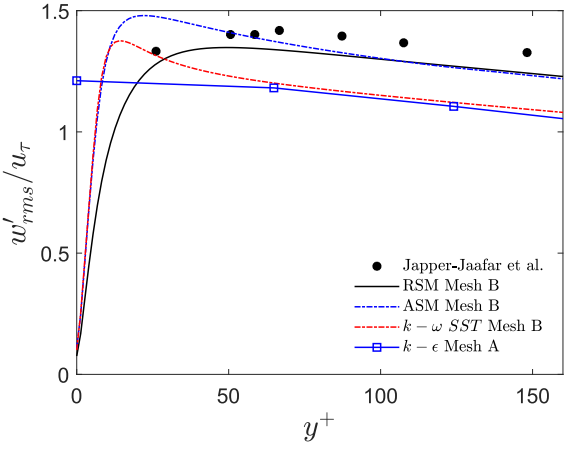

(f) Outer wall

Figure 4.11 Fluctuation velocities at $Re_{D_h} = 38700$. Note: rms of the fluctuating velocities for the two-equation models are estimated from $u'_{rms} = v'_{rms} = w'_{rms} = \sqrt{\frac{2}{3}k}$.

the axial velocity fluctuations and no peak is obtained by the $k-\epsilon$ model with Mesh A. A discrepancy between the experimental data by Corredor et al. [71] and simulations is noticeable in the range from 20 to 60 wall units where a drop in the streamwise velocity fluctuations is measured by Corredor et al. [71]. This drop is not consistent with the experimental data by Japper-Jaafar et al. [39] and Nouri et al. [59] or numerical data obtained by Boersma & Breugem [15] and Chung et al. [18].

4.4.6 Turbulent kinetic energy

The turbulent kinetic energy computed by the RSM and $k-\omega$ SST model for $Re_{D_h} = 8900$ and $\theta = 0.5$ is shown in Figure 4.12. Based on the comparisons of computed fluctuating velocities and experimental data it is reason to believe that computed turbulent kinetic energy by the RSM is more accurate than the $k-\omega$ SST model. The RSM computed slightly greater value of k near the outer wall than near the inner wall, this it not the case for the $k-\omega$ SST model. Furthermore, the $k-\omega$ SST model computed greater peak values of the turbulent kinetic energy than the RSM. Chung et al. [18] reported that the turbulent intensities of the inner wall are smaller than those of the outer wall for this case. The tendency is more prominent for smaller radius ratios. Another effect reported by Boersma & Breugem [14] is the Reynolds number dependency. Increased Reynolds number result in higher turbulent intensity near the inner wall, while the effect is absent at the outer wall.

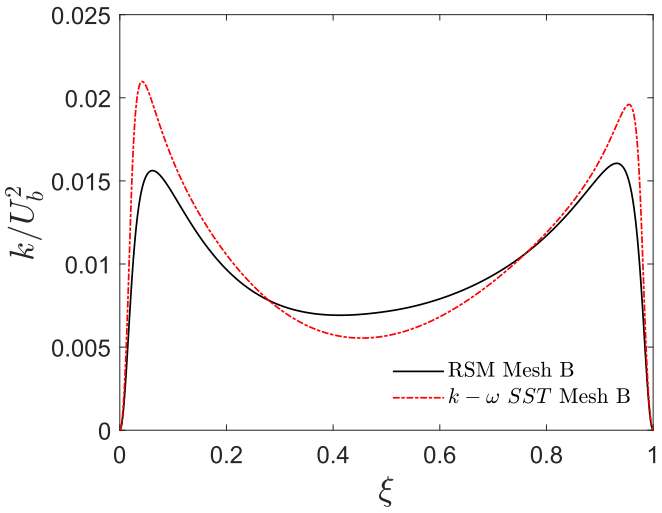

Figure 4.12 Turbulent kinetic energy at $Re_{D_h} = 8900$.

Next, the turbulent kinetic energy is shown in Figure 4.13 and 4.14 at the two higher Reynolds number flows and radius ratio $\theta = 0.4$. Here, computed values by the two-equations turbulence models are included. In the near wall region the turbulent kinetic energy is modelled when wall functions are used and do not approach zero at the wall. As the Reynolds number

is increased, better agreement between simulations with wall functions and the fine mesh simulations is obtained. Corredor et al. [71] did not measure the tangential velocity component

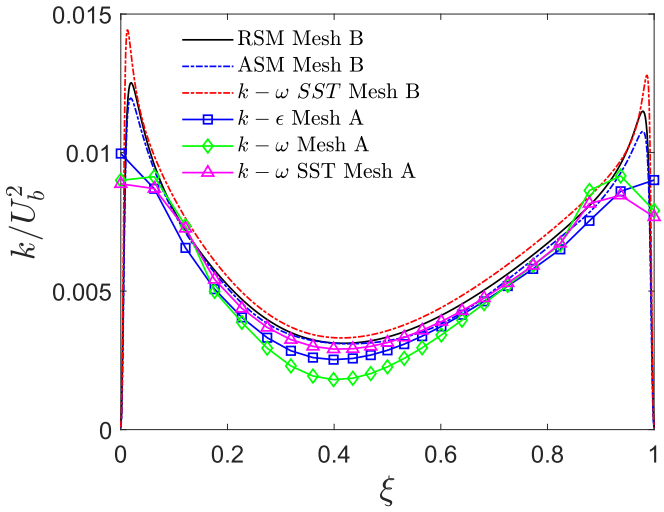

Figure 4.13 Turbulent kinetic energy at $Re_{D_h} = 38700$.

and the experimental values in Figure 4.14 are based on velocity fluctuations in the radial and axial direction. As seen in the previous section the tangential component is larger than the radial component and smaller than the axial component. Based on this the turbulent kinetic energy is expected to be higher than the experimental data provided by Corredor et al. [71]. Significant discrepancies are found at approximately $\xi = 0.1$ and 0.9 where the experimental data has a drop in the turbulent kinetic energy and is due to the measurement of the axial velocity fluctuations. Corredor et al. [71] obtained similar measurements for $Re_{D_h} = 38700$ discussed in section 4.4.5.

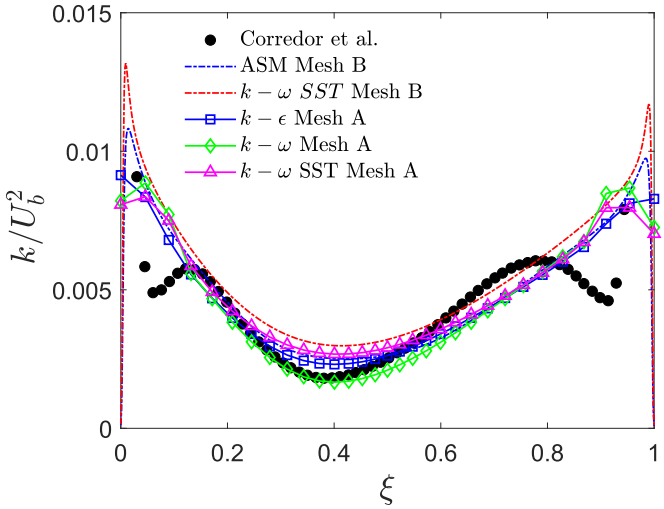

Figure 4.14 Turbulent kinetic energy at $Re_{D_h} = 56400$.

4.4.7 Reynolds stresses

The Reynolds stress distribution nondimensionalized by the outer wall friction velocity for the annular section is given in Figure 4.15 at $Re_{D_h} = 8900$. For the $k-\omega$ SST model the Reynolds stress is estimated from the Boussinesq's approximation in equation 2.15. Comparisons are made to the DNS by Chung et al. [18]. The distribution of the Reynolds shear stress is asymmetric. The Reynolds stress is greater close to the outer wall than close to the inner wall. Regarding the discussion whether the position of maximum streamwise velocity and zero Reynolds stress coincide, here the RSM simulations give no coincidence of these points. This is consistent with the DNS by Chung et al. [18] but not with the DNS by Boersma & Breugem [14]. As expected, the simulations with the $k-\omega$ SST model show coincidence of these points and is due to the eddy viscosity model. However, this study cannot be decisive for such a fundamental behaviour in turbulent flows.

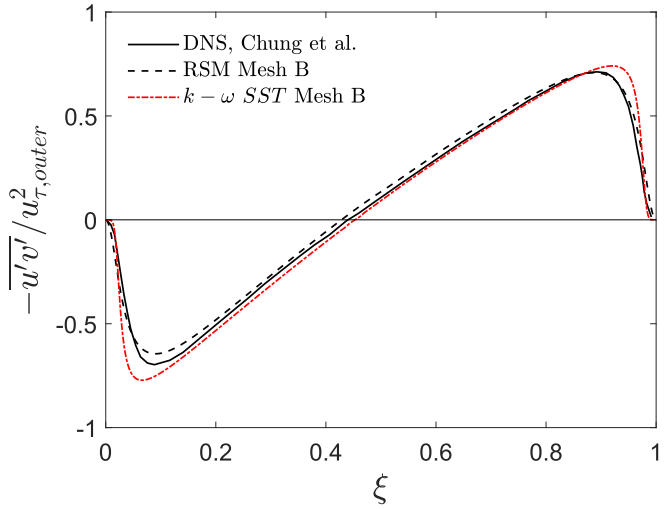

Figure 4.15 Reynolds stress distribution at $Re_{D_h} = 8900$. Note: the Reynolds stress for the two-equation model is computed from the Boussinesq approximation, equation 2.15.

The Reynolds stress close to the inner and outer wall in wall coordinates are given in Figure 4.16 and 4.17 respectively. Here, the Reynolds stress is normalized by the local friction velocity. The $k-\omega$ SST model peak closer to the wall compared to the RSM and the DNS by Chung [18]. Kim et al. [41] performed a DNS for a turbulent fully developed channel flow and the data is included in Figure 4.17. It is evident that the Reynolds stress distribution in the outer wall region is similar to the channel flow by Kim et al. [41].

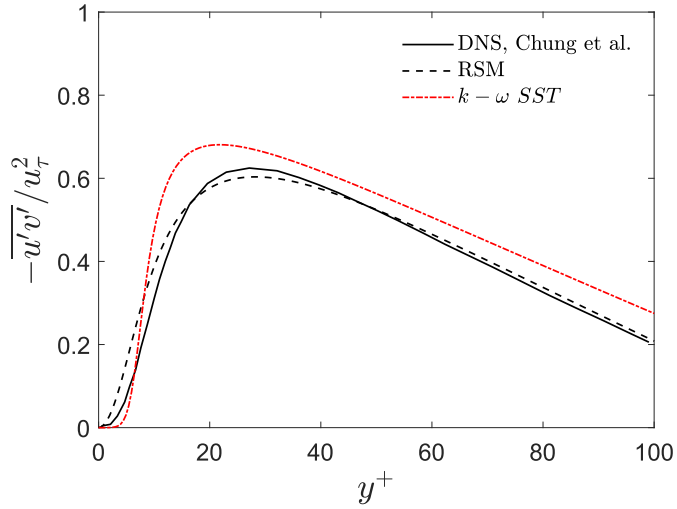

Figure 4.16 Reynolds stress distribution close to the inner wall at $Re_{D_h} = 8900$. Note: the Reynolds stress for the two-equation model is computed from the Boussinesq approximation, equation 2.15.

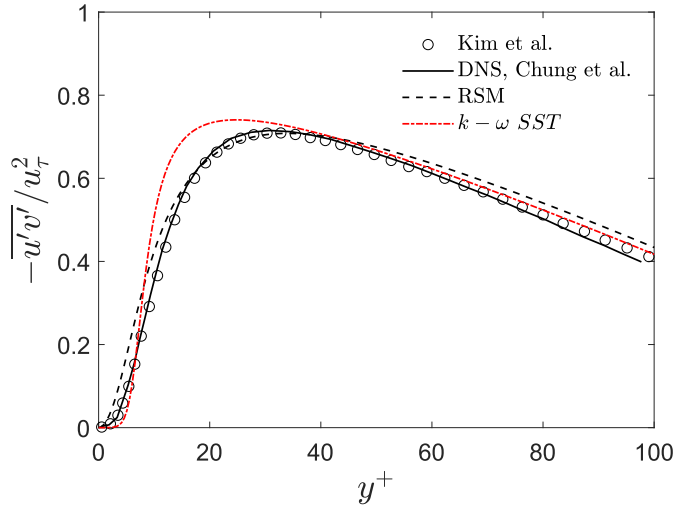

Figure 4.17 Reynolds stress distribution close to the outer wall at $Re_{D_h} = 8900$. Note: the Reynolds stress for the two-equation model is computed from the Boussinesq approximation, equation 2.15.

The distributions of the Reynolds stress at $Re_{D_h} = 38700$ and 56400 are given in Figure 4.18 and 4.19. Also here the Reynolds stress is estimated from the Boussinesq's approximation in equation 2.15 for the two-equation turbulence models. The peak value of Reynolds stress is moved closer to the wall as the Reynolds number is increased. At both Reynolds numbers the fine mesh simulations are in good agreement. The results from the $k-\epsilon$ model are in agreement the fine mesh simulations and the experimental data, except close to the wall.

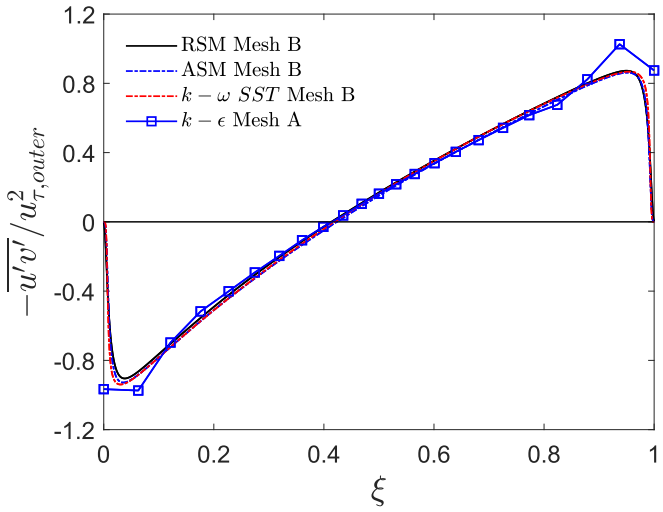

Figure 4.18 Reynolds stress distribution at $Re_{D_h} = 38700$. Reynolds stress distribution close to the inner wall at $Re_{D_h} = 8900$. Note: the Reynolds stress for the two-equation models are computed from the Boussinesq approximation, equation 2.15.

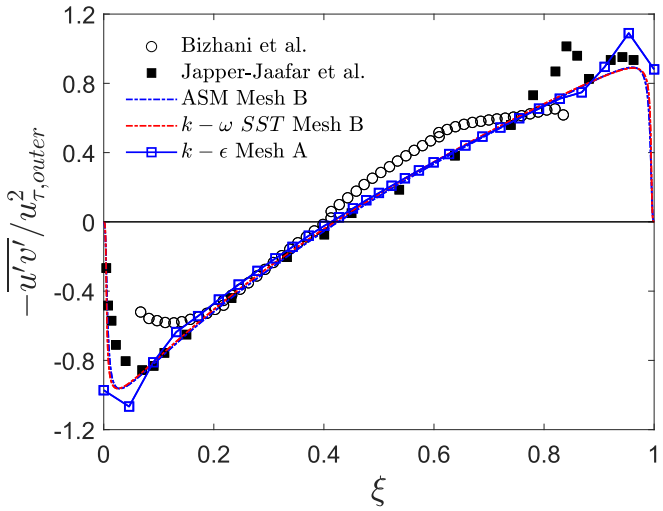

Figure 4.19 Reynolds stress distribution at $Re_{D_h} = 56400$. Note: the Reynolds stress for the two-equation models are computed from the Boussinesq approximation, equation 2.15.

The Reynolds stress ($\tau_{Re} = -\overline{u'v'}$) and the total shear stress ($\tau_{Tot} = -\overline{u'v'} + \nu\frac{\partial \overline{u}}{\partial y}$) close to the inner and outer wall at $Re_{D_h} = 38700$ are shown in Figure 4.20. Both stresses are normalized by the local friction velocity. The distribution of the total shear stress is slightly curvilinear due to the curvature. At the wall the total shear stress is equal to unity, i.e $\tau_w = \mu\frac{\partial \overline{u}}{\partial y}$. Here, the viscous stresses are dominant in the viscous sublayer. Both Reynolds and viscous stresses are present in the buffer region, while the Reynolds stresses are dominant in the logarithmic region. This is consistent with the theory given in section 2.7.

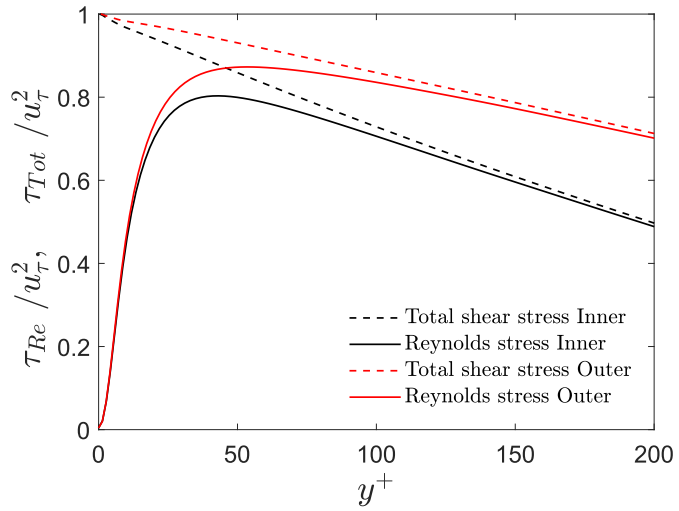

Figure 4.20 Reynolds stress and total shear stress at $Re_{D_h} = 38700$ computed by the RSM.

4.5 First test case conclusion

Turbulent flow in a concentric annulus at three Reynolds numbers and two radius ratio were investigated numerically by ANSYS Fluent. Two-equation turbulence models, ASM and RSM simulations were performed for both standard wall functions and near wall modelling. The mean streamwise velocity profile is asymmetric and skewed to the inner wall. The mean axial velocity for the fine mesh ($y^+ \approx 1$) was found to follow the classical law of the wall. Both RSM and ASM resemble the fluctuation velocities, as evidenced by comparisons with experimental data by Nouri et al. [59], Corredor et al. [71] and Japper-Jaafar et al. [39]. It is found that the RSM produce greater anisotropy than the ASM. Nevertheless, the beta version of the ASM in ANSYS Fluent has potential, due to less computational cost.

A tendency is observed, i.e. as the Reynolds number increased the turbulence models produced more similar results for the turbulent kinetic energy and the Reynolds stress. Acceptable concurrence was found between the two-equation turbulence models and the RSM outside the inner region of the turbulent boundary layer. In addition, the two-dimensional axisymmetric simulations in this test case are found to be acceptable when comparing to the DNS by Chung [18] and the experimental data.

Chapter 5

Confined Bluff Body

The second test case is the flow downstream of a bluff body confined by an outer pipe wall. This test case is relevant to the venturi scrubber due to the modelling of particles. In addition, similar geometry is present in the venturi scrubber. The confined bluff body (CBB) flow is a well-known model validation of particle-laden gas flows and the mixing of solid particles. The CCB represents a simple geometric flow. Nevertheless, it contains many important features of more complex industrial particle-laden flows. Borèe et al. [15] investigated the CBB flow experimentally by Phase Doppler Anemometry (PDA) and the experimental data is used for validation of numerical computations. The CBB flow by Borèe et al. [15] is numerically investigated by Riber et al. [68] using several LES approaches. Riber et al. [68] obtained best agreement with the Euler-Lagrangian approach and concluded that the most critical parameters in terms of accuracy are the grid and the convective schemes. Alletto & Breuer [6] also performed a LES with more grid points than the study of Riber et al. [68] which allowed wall-resolved predictions. Furthermore, a high mass loading case including four-way coupling was considered by Alletto & Breuer [6]. Greifzu et al. [33] performed RANS simulations and investigated the effect of the dispersion model in ANSYS Fluent. Simulations were compared the to the experiment by Boreè et al. [15] and solutions obtained from the CFD program OpenFOAM. In this study the goal is to identify differences between different 2D axisymmetric and 3D mesh. Validation of simulations is obtained by comparison to experiment by Boreè et al. [15] and the numerical analysis by Greifzu et al. [33].

5.1 Case description

5.1.1 Geometry

The flow is confined by an outer pipe wall. The bluff body separate the central particle-laden jet and the annular jet. The geometry and geometric parameters are given in Figure 5.1. The radius of the central jet R_j is 10 mm and the length of the pipe is 1500 mm to ensure no

disturbance from the outflow. The radius of the outer pipe is $R_o = 15R_j = 150mm$ while the inner radius of the annular region is $R_i = 7.5R_j$ The blockage ratio is $BR = R_i^2/R_o^2 = 0.25$. The geometric dimensions are expressed in terms of the radius of the central jet, R_j, in Figure 5.1.

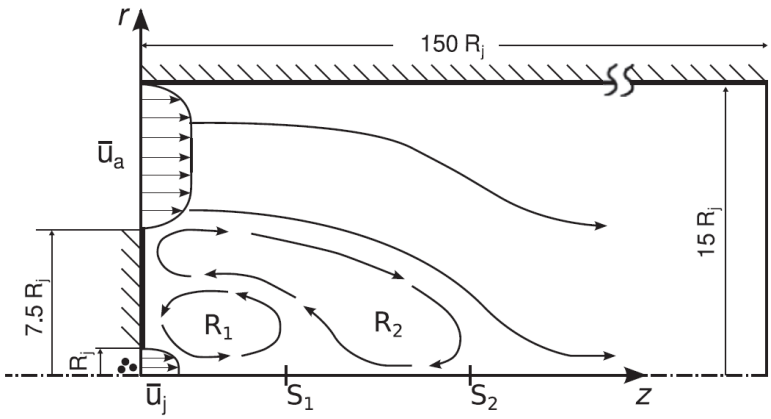

Figure 5.1 Geometry of the confined bluff body, adapted from [33].

5.1.2 Flow characteristics

The flow consists of two stagnation points, where S_1 is the mean stagnation point of the central jet and S_2 is the stagnation point where the two jets come in contact. A vortex pair, R_1 and R_2, separate the central and the annular jet. Downstream of stagnation point $S2$, where the central and annular jet is merged together, a wake-like region is observed by Boreè et al [15].

Following the approach suggested by Elghobashi [28] described in section 2.9, the volume fraction of particles is moderate $\alpha = 2 \cdot 10^{-6}$. Hence, the flow regime is categorized as medium according to Figure 2.3 and a two-way coupling is needed. The injected particles are assumed to be spherical and the particle diameter is $d_P = 63\ \mu m$. The relaxation time from equation 2.64 is $\tau_P = 27.6$ ms and was obtained by Riber et al. [68]. The time characteristic of the flow field, τ_F, is estimated by the fluid most energetic eddies and is estimated as:

$$\tau_F = \frac{2R_o/3}{u_F'^{max}} \tag{5.1}$$

where $u_F'^{max}$ is the maximum fluctuating velcoity in the pipe. Based on estimations by Riber et al. [68] the time characteristic of the fluid flow is $\tau_F \approx 7$ ms. The ratio of the particle relaxation time and the time characteristic of the fluid flow result in a Stokes number, $St = \frac{\tau_P}{\tau_F} = 3.9$. Flow characteristics are given in Table 5.1. The Reynolds number based on the hydraulic diameter of the annular duct is $Re_{D_h} = 20000$.

Table 5.1 Flow characteristics

Continuous phase		Dispersed phase	
Fluid	Air	Material	Glass beads
Central jet		Particle diameter	$d_P = 63\ \mu m$
Inlet velocity profile	$\overline{u}_{j,avg} = 3.01$ m/s	Particle density	$\rho_P = 2470\ kg/m^3$
Annular jet		Particle mass flow rate	$\dot{m}_p = 2.78 \cdot 10^{-4}$ kg/s
Inlet velocity profile	$\overline{u}_{a,avg} = 5.36$ m/s	Injection velocity	$u_{P,z} = 4.08$ m/s
Kinematic viscosity	$\nu = 1.5 \cdot 10^{-5} m^2/s$		
Reynolds number	$Re_{D_h} = 20000$		

5.2 Numerical setup

Investigation of the turbulent particle-laden flow is based on the RANS equations, described in section 2.3. The dispersed phase is solved with the discrete particle model (DPM) and the discrete random walk model in Fluent. The discrete particle model (DPM) is described in section 3.2. As a two-way coupling is considered the momentum exchange is obtained through the term for body forces. The particle motion of the dispersed phase is solved in a Lagrangian frame, obtained from equation 2.66 and equation 2.72. The $k - \epsilon$ turbulence model was chosen as Greifzu [33] stated that this eddy viscosity model were able to predict the position of the stagnation points in agreement with experimental data. In addition, the performance of the $k - \epsilon$ model was investigated in detail in the first test case.

A velocity profile obtained from a 1/7 power law with a maximum centre velocity in the streamwise direction $U_{j,z} = 3,4m/s$ is given for the central jet. To match the experimental setup the average mean streamwise velocity is $\overline{u}_{j,avg} = 3,01m/s$. Similarly, a velocity profile with a average mean streamwise velocity $\overline{u}_{a,avg} = 5.36m/s$ is given for the annular jet at the inlet. The particles are injected in the streamwise direction with a uniform velocity $\overline{u}_{P,avg} = 4,08m/s$. Initial and boundary conditions for other quantities were given in section 3.3.

5.2.1 Mesh

Firstly, a two-dimensional orthogonal structured mesh is used to ensure $y^+ > 30$ in order to apply standard wall functions. The computational domain is discretized by 125000 quadrilateral cells. The mesh is stretched in the negative radial direction to capture the region of the inner jet. The maximum aspect ratio for the two-dimensional mesh is 6.7.

Secondly, a three dimensional structured mesh is used. The mesh consists of 299520 hexahedral cells. In the centre of the pipe there is a Cartesian mesh and a cylindrical mesh outside the core. This mesh is known as a butterfly grid. The mesh is shown in Figure 5.2 in the

streamwise direction. Hernandez-Perez et al. [37] investigated different mesh structures for two-phase flow and validated simulations against experimental results. The best agreement with experimental data was obtained with a butterfly grid. Due to the structure of the mesh, refinement in the near wall region may be applied, while the singularity at the centre of the pipe is prevented. Here, the mesh is not refined in the wall region and standard wall functions are applied for simulations with the butterfly grid. As for the evaluation of the mesh quality, the maximum aspect ratio is 15, the average skewness is 0.07 with a maximum skewness of 0.5. In addition, the minimum orthogonality of the mesh is 0.78.

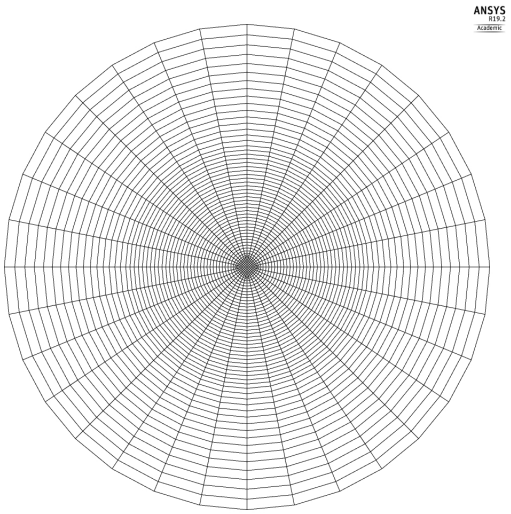

Figure 5.2 Three-dimensional mesh.

Mesh validation - Laminar pipe flow

To check the quality of the 3D mesh a separate laminar pipe flow simulation is performed. The classical Poiseuille flow is characterized by steady laminar flow of an incompressible Newtonian fluid induced by a pressure difference with a pipe length L and radius R << L. By a simple force balance on a volume element and applying boundary conditions the analytical solution of the velocity profile may be obtained:

$$u(r) = 2V_{avg}\left(1 - \frac{r^2}{R^2}\right) \tag{5.2}$$

A simulation with a $Re_D = 30$ and an average velocity $U_{avg} = 1m/s$ is computed for a pipe diameter $D = 0,3m$. The computed and analytical streamwise velocity is shown in Figure 5.3. Overall the computed profile is matching the analytical profile and the mesh is deemed acceptable for this laminar flow.

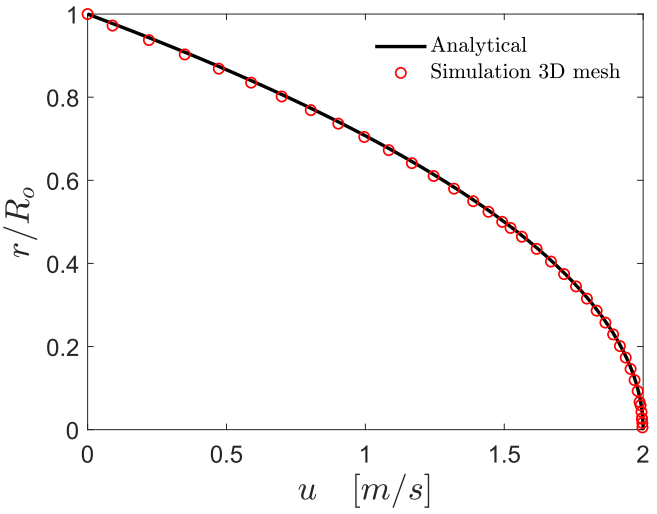

Figure 5.3 Laminar velocity profile at $Re = 30$.

5.3 Results and discussion

The flow characteristics, i.e the development of the central and annular jet, the stagnation points and the vortex pair are shown in the vector plot in Figure 5.4. Here, the vectors are coloured by the velocity magnitude and the solid lines black lines represent zero streamwise velocity of the gas phase, $\overline{u}_z = 0$. In addition, the locations of $z/R_j = 8, 16, 24, 32$ and 40 are shown. The central jet is stopped rapidly and the main contributors to the decrease are the high turbulent shear stress and the axial pressure gradient according to Boreè et al. [15]. The central jet is surrounded by a recirculation flow. A annular shear layer is developed at the edge of the bluff body.

Two stagnation points S_1 and S_2 develop in the streamwise direction at the centre of the pipe. The positions of the stagnation points are summarized in Table 5.2. Here, the experimental data by Boreè et al. [15] and the numerical data by Greifzu et al [33] are included. Greifzu et al. [33] performed three-dimensional RANS simulations with the standard $k-\epsilon$ model, similar to the present study, but discretized the computational domain by 2.01 million hexahedral cells. The two-dimensional simulation predict the position of S_1 accurate but fail to accurately predict the second stagnation point, S_2. In contrast, the opposite is true for the three-dimensional simulation.

Table 5.2 Location of stagnation points

	S_1 [mm]	S_2 [mm]
Boreè et al.	121	217
Greifzu et al.	95	235
$k-\epsilon$ 3D	99	229
$k-\epsilon$ 2D	119	249

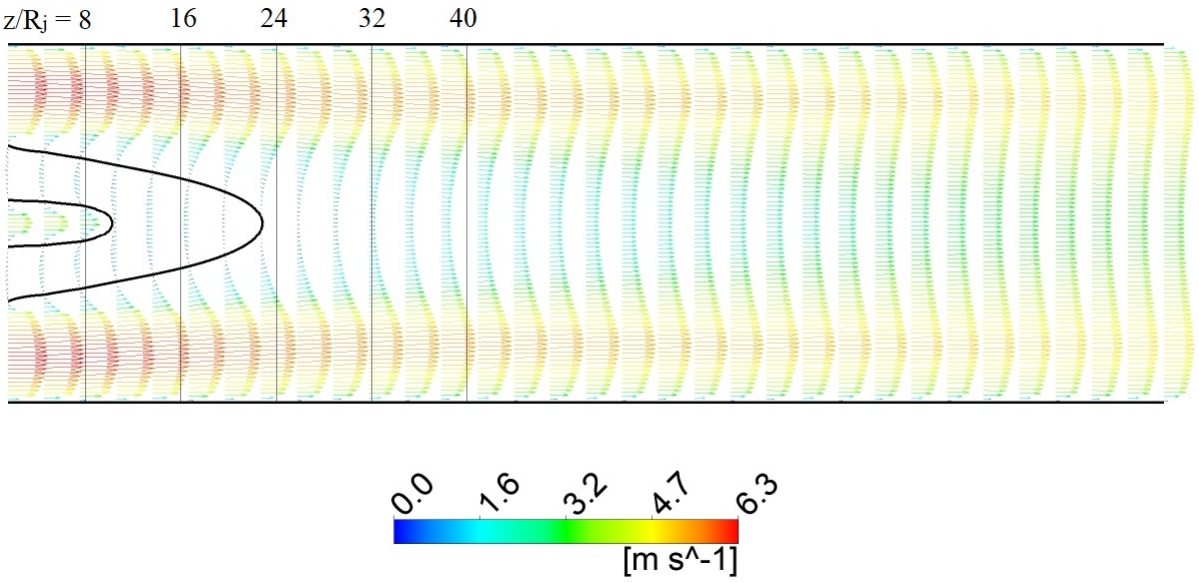

Figure 5.4 Vector plot of the confined bluff body flow.

Next, the streamwise gas velocity along the symmetry line is given in Figure 5.5. The velocity is normalized by the maximum streamwise jet velocity $U_{j,z}$. The stagnation points are located at the intersections with the line $\overline{u}_z/U_{j,z} = 0$. As the stagnation points are not accurately predicted the results of the velocity development downstream suffer and more prominent for the two-dimensional simulation. Clear similarities between the three-dimensional simulation and the results of Greifzu et al. [33] are observed. Greifzu et al. [33] predicted a higher negative axial velocity than the present simulations. The finer mesh by Greifzu et al. [33] may contribute to these differences.

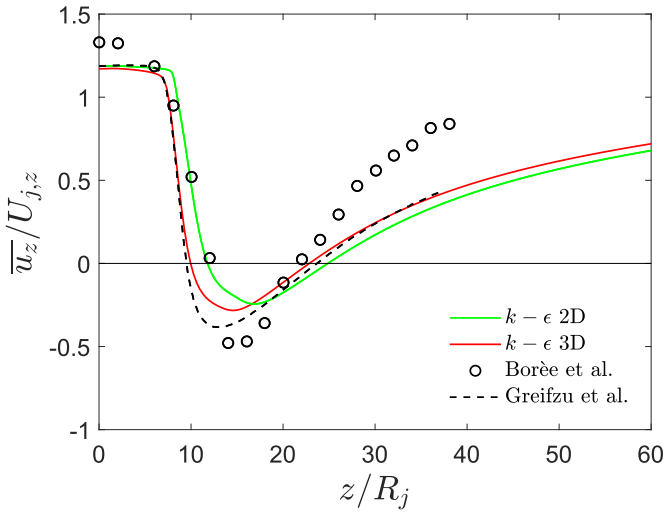

Figure 5.5 Axial velocity along the symmetryline.

The development of the velocity profiles in the streamwise direction as a function of the span-wise coordinate is shown in Figure 5.6. Note that the normalized velocity profiles are amplified in order to highlight deviations. The streamwise velocity profiles are given at $z/R_j = 0.3, 8, 16, 24, 32$ and 40. In accordance with the results in 5.5, the numerical simulations lag behind the experimental data by Boreè et al. [15] downstream of the second stagnation point S_2. The flow near the symmetry axis the acceleration of the flow is underpredicted by the simulations. Therefore, the momentum transfer from the outer region to the central region is underestimated. It is assumed that this wrongful momentum transfer is due to the steady-state RANS modelling of wake flows and is also reported by Iaccarino et al. [38]. The inlet conditions are specified in order to obtain good agreement with the experiment at the location $z/R_j = 0.3$. However, setting appropriate inflow boundary conditions are challenging, see velocity profile at $z/R_j = 0.3$. In this study, the simple $k - \epsilon$ and wall function are considered and accurately inflow conditions are difficult to set. The influence of the boundary conditions was reported by both Riber et al. [68] and Alletto & Breuer [6] and considerably work were done to obtain an accurately inflow boundary conditions. Alletto & Breuer performed two LES for the solely purpose of generate reasonable inflow data.

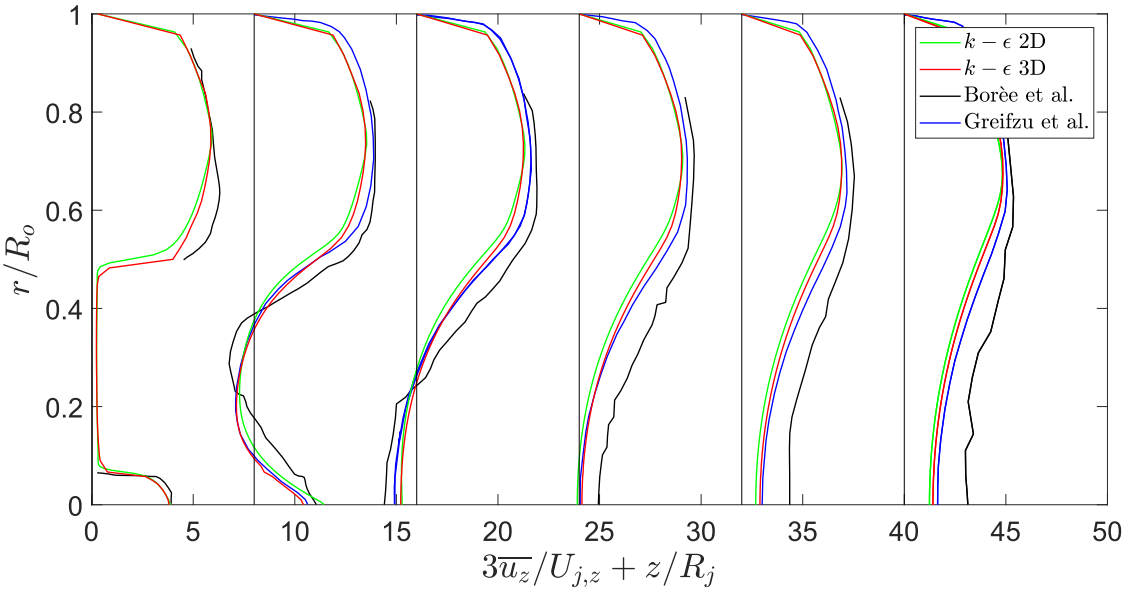

Figure 5.6 Mean axial velocity of the gas phase.

The streamwise velocity profiles of the dispersed phase at $z/R_j = 0.3, 8, 16, 24, 32$ and 40 are given in Figure 5.7. Here, a good overall agreement between simulated and experimental profiles are obtained. Also here, the simulations lag behind the experimental data. In the present study, a dependency on the total number of tracked particles was found. A greater number of tracked particles resulted in a more accurate representation of the particle velocity profile. The simulated dispersion of the particles are slightly smaller than in the experiment by Boreè et al. [15].

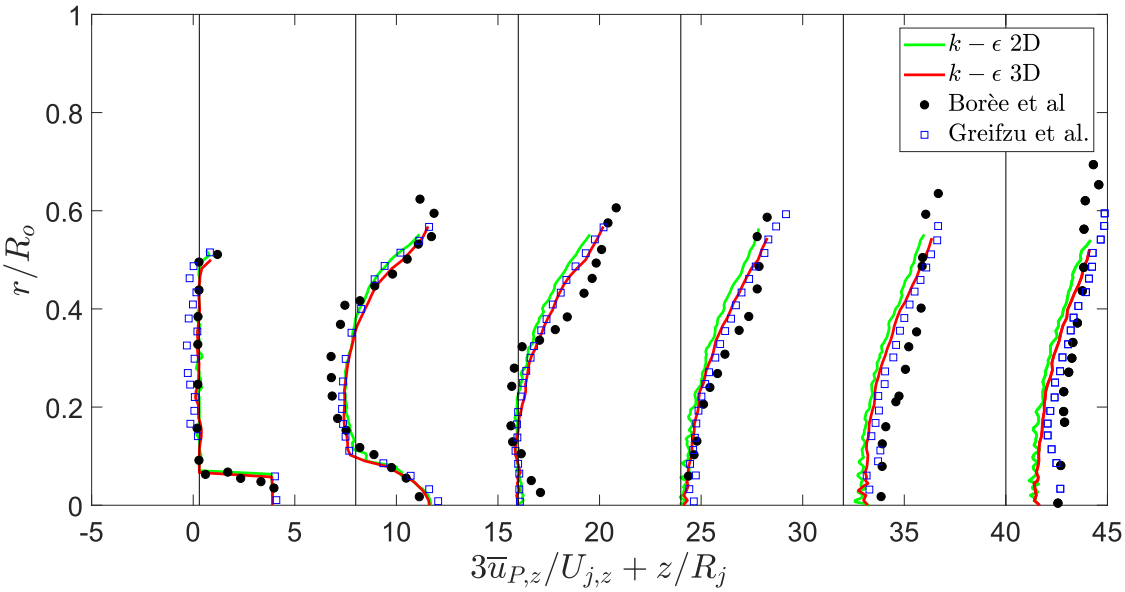

Figure 5.7 Axial velocity of particles.

The particle trajectories downstream of the bluff body are given in Figure 5.8. The trajectories are 20% of the total number of tracked particles. Here, results of the two-dimensional axisymmetric model are presented and the trajectories are coloured by the streamwise particle velocity. It is evident that the trajectories are influenced by the turbulent dispersion computed from the discrete random walk model. Due to this model particles may be found close to the centre of the pipe as well as in the region close to the annular flow. In the present study no particles are trapped in the recirulation regions, while the LES by Alletto & Breuer [6] indicated a mean rotatory motion of the particles in recirculation region R_1, see Figure 5.1.

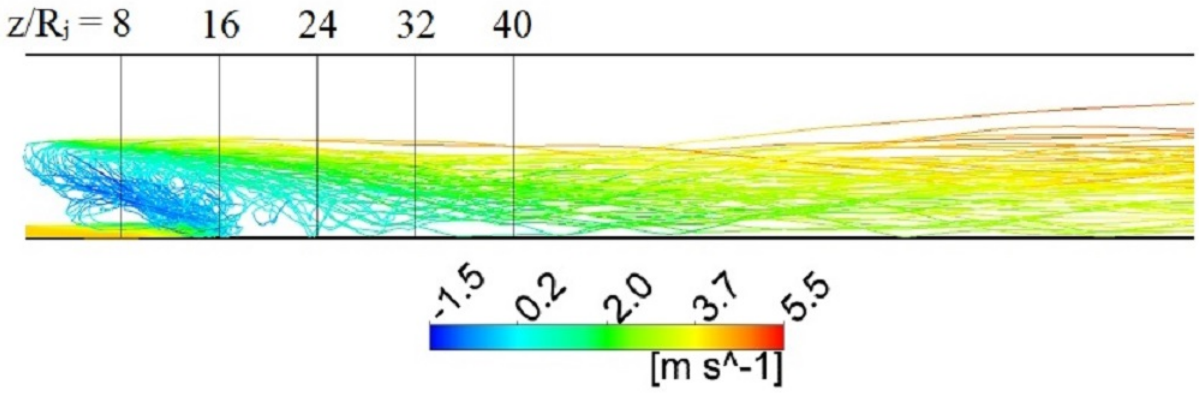

Figure 5.8 Particle trajectories computed by the axisymmetric model, coloured by the streamwise particle velocity.

5.4 Second test case conclusion

In the present study, turbulent particle-laden flow downstream of a confined bluff body was investigated. Simulations are based on the RANS equations for the continuous phase, while the discrete particle model (DPM) with two-way coupling in ANSYS Fluent was used for the dispersed phase. Both three-dimensional and two-dimensional axisymmetric simulations of the continuous phase are adequately captured, as evidenced by the comparison with the experimental data by Boreè [15]. However, the two stagnation points are computed somewhat different compared to the experiment. In addition, the axial velocity development of the the gas phase in the centre region is underpredicted and it is expected due to insufficient momentum transfer from the annular flow to the central region. This is one of the shortcomings of the applied RANS modelling of the flow.

The results of the dispersed phase are in agreement with experimental data. Only small differences between of the three-dimensional and two-dimensional simulations were observed. Based on the present study, a two-dimensional axisymmetric model and the RANS approach with the DPM are capable to model particle-laden gas flows and may be used in the numerical analysis of the venturi scrubber.

Chapter 6

Venturi Scrubber

Glencore Nikkelverk AS is currently using a venturi scrubber to clean the pollutant gas from a pilot processing plant. Solid particles of copper is present in the pollutant gas. The venturi scrubber is an air pollution control device that is designed to remove copper particles in a pollutant gas from a stationary point source. The permit of emission to open air given by the Norwegian Environment Agency state that the level of copper concentration in the cleaned gas cannot be more dense than $5 \cdot 10^{-6}\ kg/m^3$. The fluid dynamics in the installed scrubber is desired due to a planned scale-up of the current pilot processing plant. Similarly, the pollutant gas from new full-scale processing plant needs to be cleaned.

This chapter will investigate both the installed and full-scale scrubber. The findings in previous test cases will be utilized to establish a numerical analysis of the particle-laden gas flow in the installed scrubber. The results are compared to the measurements by Glencore Nikkelverk AS for the pilot scrubber. Finally, a scale-up of the installed scrubber is performed and the results of the full-scale scrubber are presented.

6.1 Process description

The schematic of the gas cleaning system is given in Figure 6.1. The schematic include all elements in the system from the pollutant source to the stack and discharge to the open air, e.g. scrubber, entrainment separator, recirculation tank, pump, fan and stack. This investigation will only consider the fluid dynamics of the particle-laden gas, where scrubbing liquid is not considered. Furthermore, the entrainment separator downstream of the scrubber is not investigated. Including these limitations, the flow in the scrubber is expected to be a particle-laden gas. The scrubber performance suffers greatly as these limitations are introduced and is described in depth in section 6.3.

Another simplification is the particle deposition downstream of the scrubber to the stack.

Firstly, in the entrainment seperator a demister is installed. The liquid droplets containing copper particles will seperate from the gas. Secondly, in the entrainment separator a portion of droplets and particles will settle due to gravity. Therefore, the particle collection is enhanced in the entrainment separator. In addition, some particles will stick to the pipe wall and elbows downstream of the scrubber.

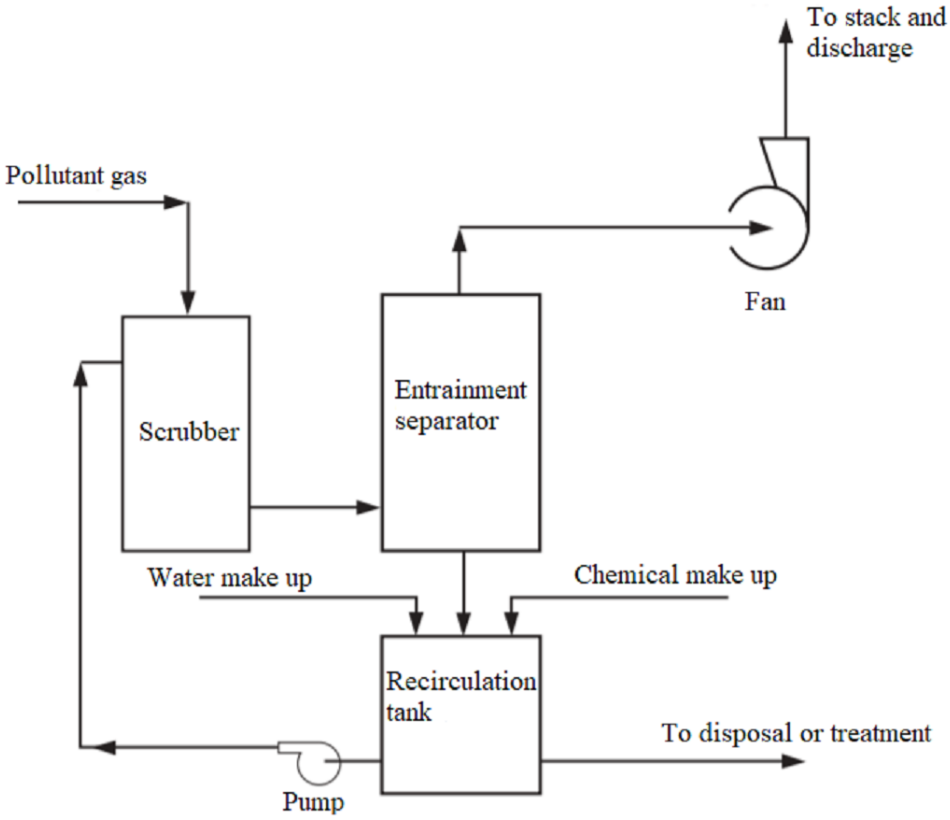

Figure 6.1 Scrubber schematic.

6.2 Scrubber design

The venturi scrubber is chosen due to its flexibility, simplicity and the ability to collect fine as well as coarse particles. It is one of the most used types of particluate scrubbers [62]. In addition, wet scrubbers have lower capital cost than other cleaning devices and approximately equal operation and maintenance costs [58]. The current design of the venturi scrubber is based on in-house experience from design and operation of several scrubber systems at Glencore Nikkelverk. A three-dimensional representation of the scrubber design is shown in Figure 6.2a. The pollutant gas enters the scrubber from the upper pipe, while the gas exit the scrubber from the lower pipe. The venturi scrubber has a converging-diverging geometry. An internal view of the pilot scrubber is shown in Figure 6.2b, where the axis of symmetry is

included. The throat is where the cross-sectional area is the smallest and the gas velocities the greatest. The position of the plug is adjustable along the vertical axis. The annular clearance between the plug and the wall of the scrubber may be reduced or increased by the position of the plug and thereby changing the velocity of the gas in the scrubber. This design provides control over the gas velocities and pressure drop. The flow in the annular clearance present in the scrubber is similar to the concentric annulus flow investigated in chapter 4.

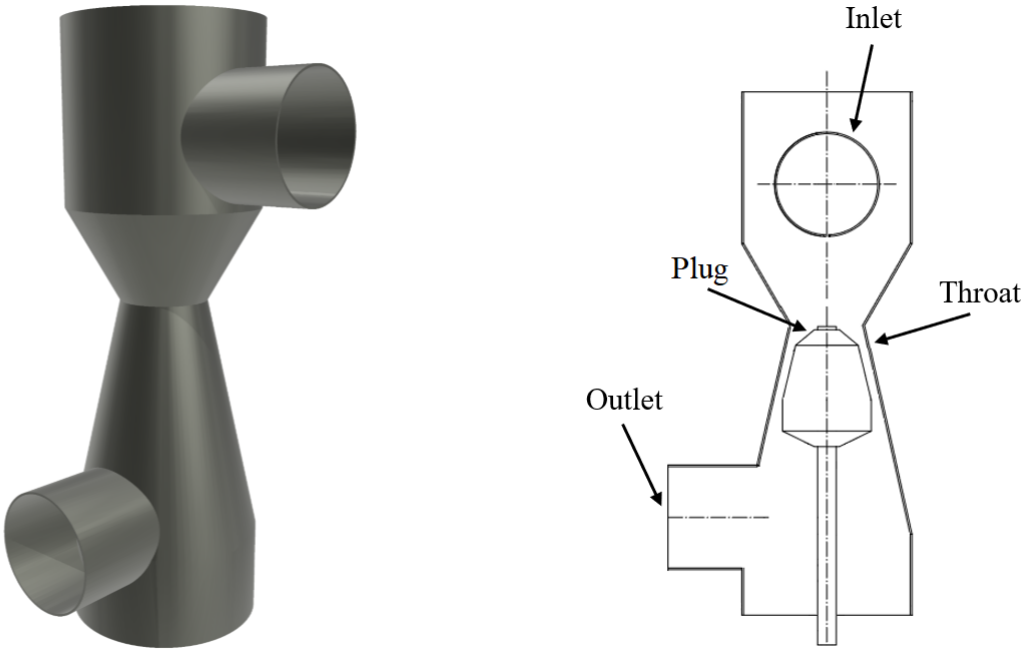

(a) External view

(b) Internal view

Figure 6.2 Scrubber design.

6.3 Scrubber performance

The overall performance of a venturi scrubber is it ability to remove particles from the pollutant gas, this is called the particle collection efficiency. The pollutants are removed through impaction, diffusion, interception and/ or absorption of the particles onto droplets of liquid. This thesis will not include the liquid phase and the corresponding physics as stated in section 1.3. However, according to Perry [62] and Miller [54] the predominant particle collection mechanism is impaction. This mechanism can be explained by considering a particle that is carried along the gas stream and it tends to follow the streamlines but may impact an approaching droplet because of its inertia. As this study only consider the particle-laden gas flow other flow characteristics are desired.

The overall performance of the pilot scrubber is affected by parameters such as:

- pressure drop
- particle size distribution
- mass loading
- gas flow rate
- temperature
- humidity
- residence time

In addition, the turbulence in the scrubber is crucial for the performance, as Danielson [25] stated that turbulence enhances particle collection by impaction. Due to turbulence the scrubbing liquid is atomized and improves the contact time between the gas and the liquid.

Firstly, a key flow parameter is the pressure drop across the venturi. The pressure drop is caused by a decrease in overall energy due to friction and other mechanical losses. The pressure drop is measured across the converging-diverging section. Higher gas velocity will increase the momentum of the particles and the collection efficiency. According to Hesketh [73] the collection efficiency does not improve when increasing the pressure drop above 11200 Pa for most venturi scrubbers. An increase in gas velocity increases the pressure drop and energy demand and generate higher operating costs for the scrubber. To minimize the pressure drop the diverging section is designed to recover most of the pressure. The gas velocity is closely linked to the pressure drop. An increase in the relative velocity between the gas and the liquid droplets increases the momentum of the particles, enabling smaller particles to be collected by impaction.

Azzopardi and coworkers [11], [9], [10] provided insight of the mechanisms at work and stated that five components contribute to the total pressure drop. The components are frictional pressure drop (I), accelerational pressure drop of the gas (II), accelerational pressure drop of the droplets (III), acceleration pressure drop of the film (IV) and gravitional pressure drop (V). The frictional pressure drop is due to the shear stress acting on the gas at the wall. The second component (II) is due to change in the kinetic energy of the gas in the converging and diverging section. The components are given in Figure 6.3 as a function of the streamwise distance. Note that there is no plug in this geometry, in contrast to the venturi scrubber at Glencore Nikkelverk and there is a wetted wall injection.
Secondly, the performance of the scrubber is dependent on the particle size distribution of the solids particles in the pollutant gas. The solid particles have varies shapes and densities.

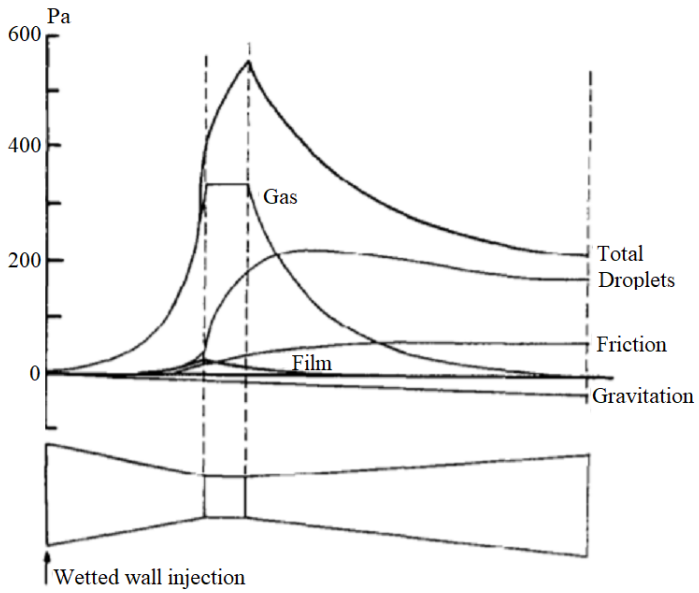

Figure 6.3 Components of venturi scrubber pressure drop, adapted from [5].

It is common to express the particle size as aerodynamic diameter. The aerodynamic diameter of a particle is the diameter of a sphere with the density of water and with the same settling velocity as the particle of interest. Proposed particle size distribution is the logarithmic, Rosin-Rammler, Gaudin-Meloy and Gates-Gaudin-Schumann distribution. A typical particle size distribution is given in Figure 6.4 where the data is similar to the log-normal distribution. Both cumulative and relative distribution are plotted with the particle size in microns (μm). The collection efficiency is a function of the particle diameter and higher pressure drops are need to collect smaller particles [62].

Other flow characteristics are the effect of gravity and residence time. In previous work [74] gravitational settling increased with increased residence time and the findings are consistent with Perry [62]. Increased residence time increases the contact time between the liquid and solid particles.

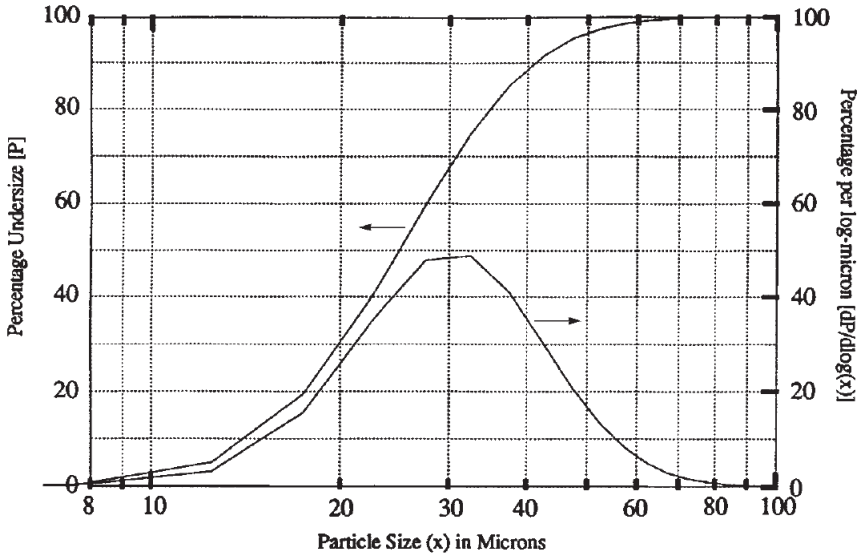

Figure 6.4 Typical particle diameter distribution, adapted from Perry [62].

6.4 Measurements by Glencore Nikkelverk

Glencore Nikkelverk AS has provided measurements of the inlet and outlet conditions of the pilot scrubber. The measurements were obtained by only considering the particle-laden gas flow and no usage of water. The measurements were obtained during steady state operation. The position of the plug was constant for all measurements. The measurements include volumetric flow rate, pressure drop over the venturi and concentration of the copper particles. The measurements by Glencore Nikkelverk are presented in section 6.8.3.

6.5 Future full-scale plant

The current processing plant, which is the source of the pollutant gas, is a pilot project where a new copper electrolysis process is tested. The pilot project has proven to be both efficient and profitable. Therefore, a new processing plant is planned to be built in 2022. The new processing plant is based on a scale-up of the pilot processing plant. In the full-scale plant the particle concentration is expected to be equal to the pilot plant. The volumetric flow rate of the pollutant gas is expected to increase from 1000 m^3/h for the pilot plant to 70000 m^3/h for the full-scale plant. The dimensions of the full-scale scrubber are approximately scaled up by a factor of ten. Results of this scrubber is presented in section 6.8.5.

6.6 Findings from test cases

The numerical analysis of the scrubber is based on the two test cases, i.e turbulent flow in concentric annulus and the flow downstream of a confined bluff body. The relevance of the test cases is shown in Figure 6.5 where the locations of the annulus and the geometry similar to the confined bluff body are shown. These classical test cases have been performed in order to validate the CFD modelling and enhance the reliability of the numerical analysis of the venturi scrubber.

Firstly, turbulence modelling where investigated in the first test case. For high Reynolds number flows the $k - \epsilon$ model is capable to resemble the turbulent flow in a concentric annulus. When wall functions are considered the near-wall region is modelled and introduce limitations to the solution as described theoretically in section 2.8.1 and shown by the results of the concentric annulus in section 4.4. Considering that the details of the flow in the scrubber is not know, a first approximation with the $k - \epsilon$ model is beneficial in terms of computational resources.

Secondly, two-dimensional axisymmetric and three-dimensional simulations have been performed. The two-dimensional axisymmetric simulations in both test cases proved to be sufficient. Thirdly, the DPM model in ANSYS Fluent is able to accurately predict particle-laden gas flows as shown in the confined bluff body case. Furthermore, the appropriate coupling between the continuous and dispersed phase can be determined by the approach by Elghobashi [28]. The approach by Elghobashi [28] was investigated for particle-laden flows in previous work [74].

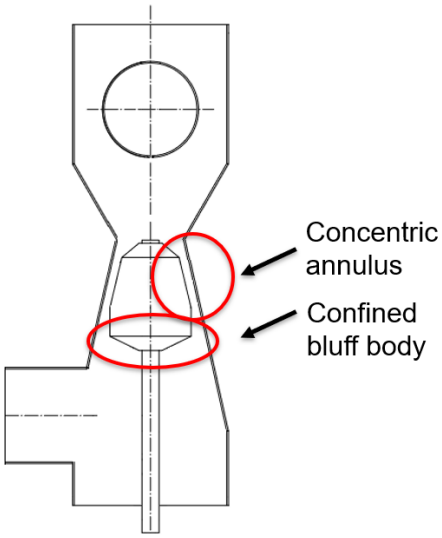

Figure 6.5 Relevance of test cases for the venturi scrubber.

6.7 Case description

6.7.1 Geometry

The geometry of the scrubber was presented in Figure 6.2, while the dimensions are given in Appendix B. The height of the scrubber is 0.841 m and the inner diameter of the inlet and outlet pipe is 0.162 m. The concentric annulus in the scrubber is defined by the radius ratio $\theta = R_2/R_1 = 0.68$ and the gap between the scrubber wall and the plug is $R_2 - R_1 = 23$ mm. Here, a two-dimensional axisymmetric model is used and is described in section 6.7.4

6.7.2 Flow characteristics

The particle-laden gas is accelerated in the converging section of the scrubber. A stagnation point is located on the tip of the plug. The maximum velocity is at the throat in the concentric annulus where the cross-sectional area is the smallest. The flow is turbulent as the Reynolds number $Re_{D_h} = 45000 - 80000$ where the hydraulic diameter is $D_h = 2(R_2 - R_1)$ evaluated in the annulus section. The range of Reynolds number is due to the different uniform velocity profiles given at the inlet. Various uniform inlet velocity profiles are given to match the volumetric flow rates for the installed venturi scrubber.

Following the approach suggested by Elghobashi [28] described in section 2.9, the volume fraction is approximately $\alpha = 8 \cdot 10^{-7}$ based on measurements by Glencore Nikkelverk. Hence, the flow regime is categorized as dilute according to Figure 2.3 and a one-way coupling is sufficient. Thus, the particles have negligible effect on the continuous phase. The injected particles are assumed to be spherical and a Rosin-Rammler diameter distribution was used. The scrubber is designed to capture particles with diameter $D_P \geq 1\mu m$. Therefore, a distribution with a minimum diameter of $1\mu m$ and a maximum diameter of $24\mu m$ is injected. The diameter distribution is shown in the histogram in Figure 6.6.

The relaxation time from equation 2.64 is $\tau_P = 0.03 - 16ms$ based on the diameter distribution. The characteristic time of the fluid flow is estimated based on the proposal by Riber et al. [68] where $\tau_F = \frac{D_h/3}{u_F'^{max}}$ evaluated in the annulus section. The maximum velocity fluctuation is estimated from

$$u_F'^{max} = \sqrt{\frac{2}{3}k^{max}} \tag{6.1}$$

where k^{max} is the maximum turbulent kinetic energy. The maximum velocity fluctuation is 5.2 m/s fot the installed scrubber. Finally, the characteristic time of the fluid flow is $\tau_F = 2.9ms$, which result in Stokes numbers in the range $St = 0.01 - 5.5$. A summary of the flow characteristics are shown in Table 6.1.

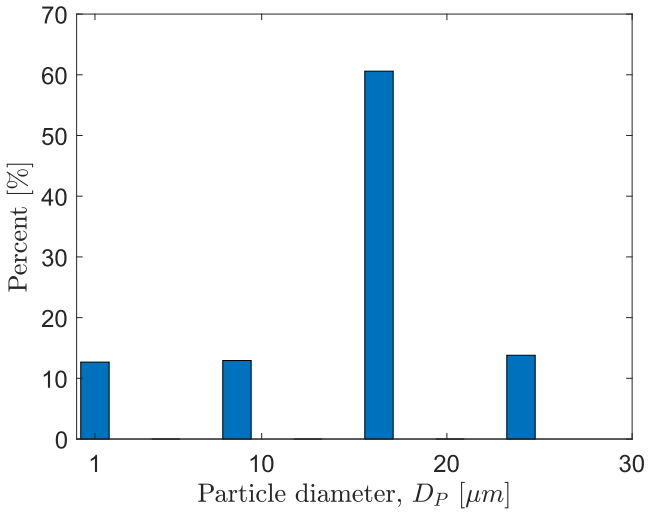

Figure 6.6 Particle diameter distribution.

Table 6.1 Flow characteristics

Continuous phase		Dispersed phase	
Fluid	Air	Material	Copper
Kinematic viscosity	$\nu = 1.5 \cdot 10^{-5} m^2/s$	Diameter	d_P = 1-24 μm
Uniform inlet profile	U_{in} = 1.0-2.2 m/s	Density	$\rho_P = 8800\ kg/m^3$
Reynolds number	$Re_{D_h} = 45000 - 80000$	Mass flow rate	$\dot{m}_p = 2.77 \cdot 10^{-7}$ kg/s

6.7.3 Numerical setup

Investigation of the turbulent particle-laden flow is based on the RANS equations, described in section 2.3. The dispersed phase is solved with the discrete particle model (DPM) in Fluent. One-way coupling is considered and the momentum exchange is obtained through the term for body forces. First a steady state solution of the continuous phase is obtained. In the next step the steady state solution of the continuous phase is fixed and the particles are injected. The particle motion of the dispersed phase is solved in a Lagrangian frame, obtained from equation 2.66 and equation 2.72. The standard $k - \epsilon$ turbulence model was chosen as discussed in section 6.6. Initial and boundary conditions were set according to section 3.3.

6.7.4 Mesh

A two-dimensional axisymmetric mesh was constructed using ANSYS Meshing. The mesh is shown in Figure 6.7. The mesh is quadrilateral dominant and a proximity size function is used to specify the minimum number of cells in the annulus section where the cross-sectional area is the smallest. The mesh in this region is based on the coarse mesh in the first test case, i.e. the concentric annulus. Furthermore, the mesh is constructed to ensure the recommendation

of $y^+ > 30$ for standard wall functions [3]. However, a two-dimensional aixsymmetric model is considered and implies that there are no circumferential gradients in the flow. The length of the outlet pipe is extended to minimize the effects of the outlet boundary conditions. As a axisymmetric model is considered a large recirculation zone is present in the outlet pipe. The total number of cells is 19348 and the maximum skewness is 0.48, while the maximum aspect ratio is 2 and the minimum orthogonality is 0.79.

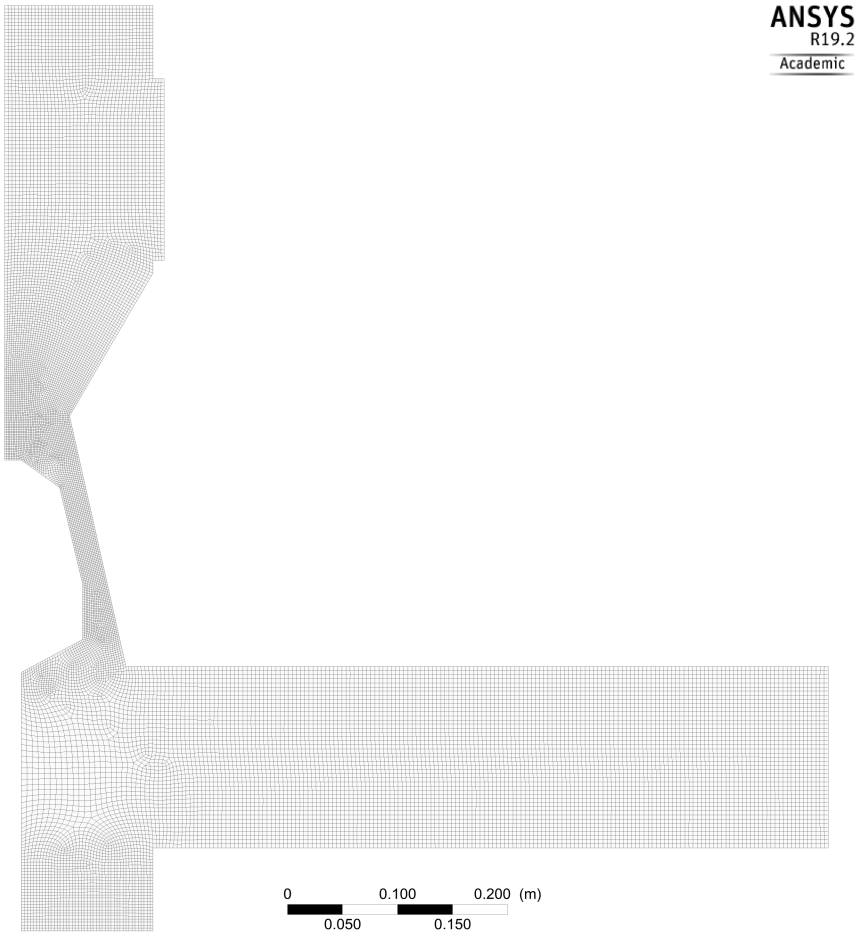

Figure 6.7 Two-dimensional axisymmetric mesh for the installed scrubber.

6.8 Results and discussion

6.8.1 Mesh convergence

A grid refinement was performed for a fixed volumetric flow rate $Q = 0.2631m^3/s$ and the pressure drop ΔP was monitored. The interpolated experimental pressure drop for the same flow rate is equal to $244.5Pa$. A summary of the grid refinement is shown in Table 6.2, where N_{cells} is the total number of cells. As the mesh is refined the computed pressure drop approach the experimental value. The convergence study is similar to the one conducted for the concentric annulus in section 4.4.3 and is based on the approach suggested by Roache [69]. Three different grids were considered: fine (1), medium (2) and coarse (3). For all mesh the requirement $y^+ > 30$ is fulfilled. The mesh is unstructured and som modifications in the mesh convergence study are needed. The grid refinement ratio r_g is estimated with the effective ratio r_{eff} defined as

$$r_{eff} = (N_1/N_2)^{1/D} \tag{6.2}$$

where D is the dimensionality of the problem. N_1 and N_2 is the number of elements for the fine and coarse mesh respectively. The order of grid convergence is $p_{grid} = 1.3$. At the medium refinement level the grid convergence index is $GCI_{2,3} = 2.3\%$, while the index for the finest refinement level is $GCI_{2,3} = 0.6\%$. Finally, the asymptotic range of convergence is $\frac{GCI_{2,3}}{r_{eff}^{p_{grid}} GCI_{1,2}} = 0.99$. However, Roache [69] stated that the convergence study for unstructured grids may significantly underestimate or overestimate the accuracy, depending on the refinement algorithm. The medium mesh is used in later computations due to computations with different volumetric flow rates.

Table 6.2 Grid refinement

Mesh	N_{cells}	ΔP $[Pa]$
Coarse	4841	262.6
Medium	19348	248.9
Fine	43519	245.5

6.8.2 Streamlines

To give an overview of the flow in the scrubber streamlines of the gas phase are plotted in Figure 6.8. The streamlines are computed at volumetric flow rate $Q = 0.2631\ m^3/s$, corresponding to an uniform inlet velocity of 1.75 m/s. In addition, the streamlines are coloured by the velocity magnitude. As expected several recirculation zones are present, i.e. in the uppermost region of the scrubber, downstream of the plug and in the outlet pipe. The particle-laden gas is accelerated in the converging section and decelerated downstream of the throat. The velocity magnitude and the turbulent kinetic energy for the installed scrubber are given in Appendix D.

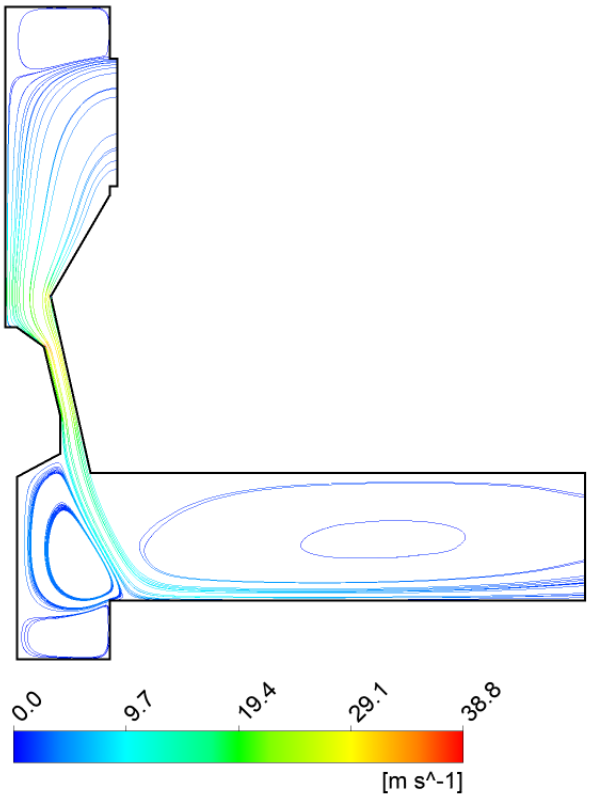

Figure 6.8 Streamlines for the installed venturi scrubber, coloured by the gas phase velocity magnitude. Computed at volumetric flow rate $Q = 0.2631\ m^3/s$.

6.8.3 Pressure drop

The static pressure for the venturi scrubber is shown in Figure 6.9 for the volumetric flow rate $Q = 0.2631\ m^3/s$. The pressure drop is determined by probe 1 and 2. The positions of the probes are based on the physical positions for the installed scrubber at Glencore Nikkelverk. The locations of the measured pressure drop for the installed scrubber are shown in Ap-

pendix E. The pressure is lowest at the throat where the gas velocities are greatest. A high pressure region is found near the top of the plug where there is a stagnation point. In the diverging section there is pressure recovery, while the velocity decreases. The pressure in the venturi scrubber at Glencore Nikkelverk is similar to the behaviour reported by Azzopardi and coworkers [11], [9], [10], see Figure 6.3. At the outlet the applied zero gauge pressure boundary condition is fulfilled.

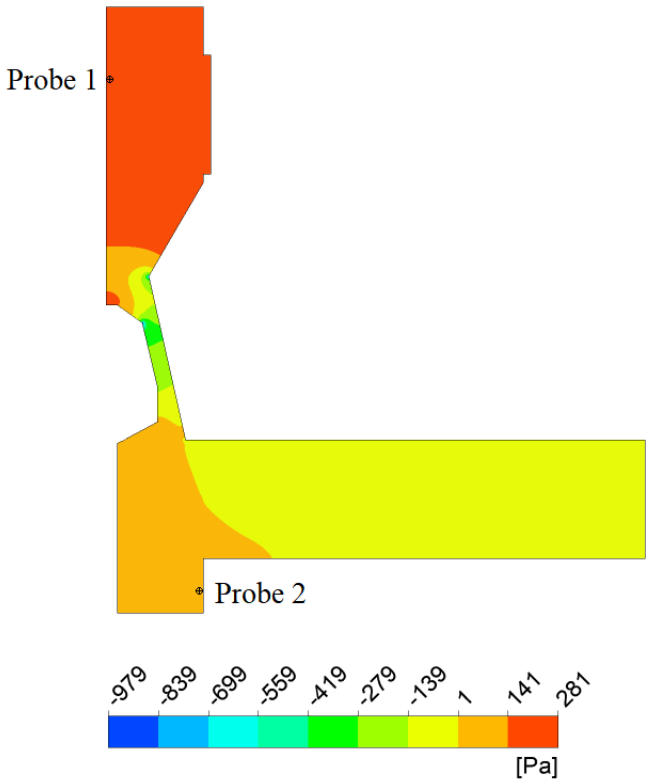

Figure 6.9 Static pressure for $Q = 0.2631\ m^3/s$.

An initial objective of the project was to compute the pressure drop across the scrubber and compare to experimental data. The pressure drop is presented in Figure 6.10, both measurements by Glencore Nikkelverk and results of the present model are included. The standard deviations of the measurements are included, in addition to a 95% confidence interval. The computed pressure drop from the numerical model show good agreement with the experimental data. The computed pressure drops are within the standard deviations of the measurements by Glencore Nikkelverk. The largest deviation from the experimental value is found at the lowest volumetric flow rate. The frictional pressure drop is due to the shear stress acting on the continuous phase at the wall and is proportional to the surface roughness and the square of the gas velocity. Therefore, the loss occurs primarily in the vicinity of the

throat. As the volumetric flow rate increases the shear stress increases and result in a greater pressure drop.

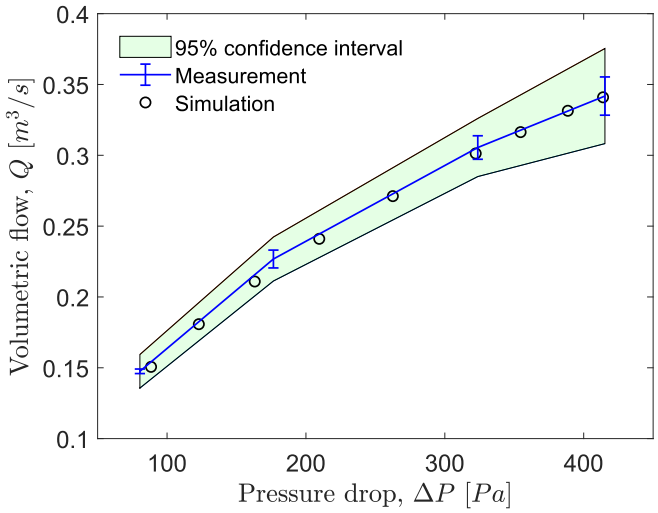

Figure 6.10 Measured and simulated pressure drop for the installed venturi scrubber at Glencore Nikkelverk

As shown in the literature survey, a number of workers have produced empirical pressure drop correlations and most designers use these correlations when developing venturi scrubber systems. In addition, analysis based on the Bernoulli's principle is often applied by designers. However, Allen et al. [5] reported that the empirical pressure drop correlations are frequently expressed as

$$\Delta P = \frac{1}{2}\psi \rho_g v_{gt}^2 \tag{6.3}$$

where v_{gt} is the throat velocity, i.e. the ratio of volumetric flow rate to cross-sectional area at the throat. Note that equation 6.3 represents the dynamic pressure at the throat multiplied by the pressure drop factor ψ. The pressure drop factor is determined by the parameters such as geometry, liquid to gas ratio and other operating conditions. In the design process of venturi scrubbers it is difficult to set an accurately pressure drop factor. Here, the factor is considered to be a constant. The pressure drop estimations from equation 6.3 with $\psi = 1$ and $\psi = 0.5$ are shown in Figure 6.11. The pressure drop is overestimated for $\psi = 1$, while acceptable estimations are obtained with $\psi = 0.5$. It is evident that a priori prediction of pressure drop is difficult and strongly dependent on the an accurate pressure drop factor, ψ.

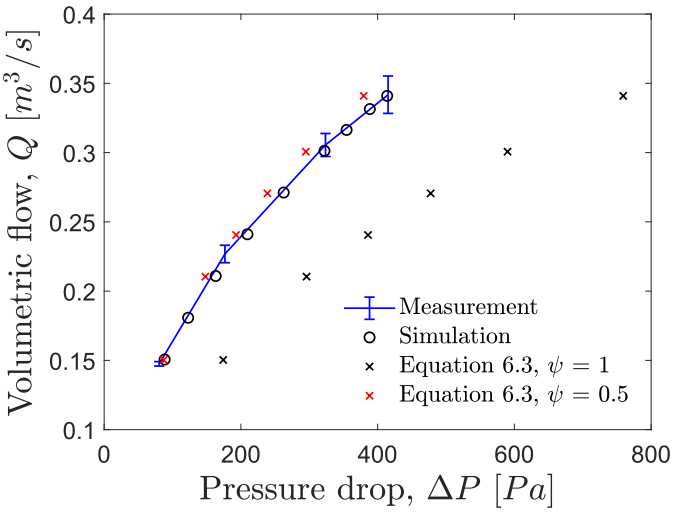

Figure 6.11 Comparisons of empirical correlations, simulations and experimental data for the pressure drop.

6.8.4 Particle path

Based on the flow characteristic of the installed scrubber described in section 6.7.2 the estimated Stokes number is within $St = 0.01 - 5.5$ depending on the particle diameter. The copper particle paths downstream of the plug with diameter $D_P = 1\ \mu m$ are shown in Figure 6.12. In addition, streamlines of the gas phase are included as black solid line. It is observed that the particle response time is less than the characteristic time of the flow field, i.e. the particles have time to respond to velocity changes and follow the fluid flow. None of the particles are captured in the recirculation zones. The smaller particles are more difficult to separate from the gas and it is consistent with the literature, e.g. see [62] and [60]. In Figure

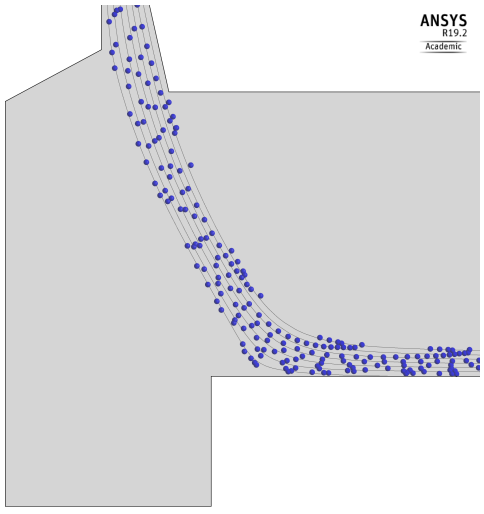

Figure 6.12 Particle path for $D_p = 1\ \mu m$, black lines are gas streamlines.

6.13 the particle path for the larger particles are shown. Here, the particles diameters are $D_P = 16.3\mu m$ (yellow) and $D_P = 24\mu m$ (red), in concurrence with the particle diameter distribution shown in Figure 6.4. The Stokes number is higher for these particles and the inertia is greater. The particles do not follow the fluid flow in the same manner as the smaller particles. Some particles are trapped inside the recirculation zones. It is reason to expect accumulation in the bottom of the scrubber due to the effect of gravity.

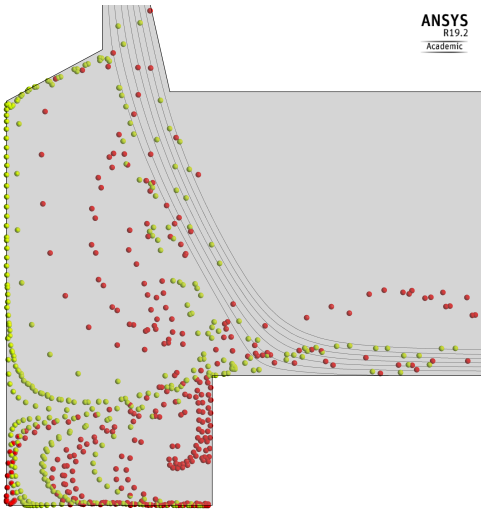

Figure 6.13 Particle path for $D_p = 10 - 24\ \mu m$, black lines are gas streamlines.

6.8.5 Full-scale scrubber

As stated earlier, Glencore Nikkelverk plan to expand the processing plant, hence a larger venturi scrubber is needed. The dimensions of the new scrubber is scaled up by a factor of ten. At the throat the gap between plug and scrubber wall is $0.23m$. The volumetric flow rate for the full-scale venturi scrubber of the gas phase is 19.44 m^3/s. The particle concentration is identical to the previous case, hence one-way coupling is considered. The Reynolds number at the throat based on the hydraulic diameter is $Re_{D_h} = 660000$. The setup in ANSYS Fluent is similar as the previous investigation of the installed venturi scrubber, see section 6.7. The mesh is also generated in the same manner and the total number of cells is 136970. Here, the estimated Stokes number is within $St = 0.0006 - 0.3$, where the approach in section 6.7.2 is used. Tropea et al. [82] stated that seed particles in the measurements techniques LDA and PIV the condition $St < 0.1$ returned an acceptable flow tracing accuracy with errors below 1%.

The copper particle paths in the full-scale scrubber for the complete diameter distribution are shown in Figure 6.14. The particles are represented by a constant diameter. However, the particles are coloured according to the different particle diameters. In this case the copper

particles follow the fluid flow in the same manner as in the installed scrubber for the smallest particles, see Figure 6.12. This particle behaviour is expected as the Stokes number is small. It is found that the dimensions of the scrubber affect the particle paths. Here, new considerations may be considered to change the particle path. In example, the position of the plug may be used to change the cross-sectional area at the throat and hence the throat velocity. In this manner, higher Stokes number may be obtained. However, the pressure drop will increase according to the analysis of the installed scrubber. The velocity magnitude, the static pressure and the turbulent kinetic energy for the full-scale scrubber are given in Appendix F.

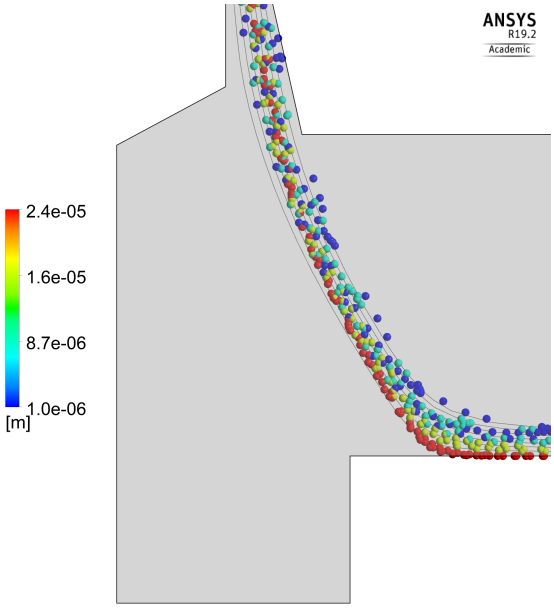

Figure 6.14 Particle path in full-scale scrubber, black lines are gas streamlines.

Chapter 7

Conclusion

A numerical study of the installed venturi scrubber at Glencore Nikkelverk was conducted. Firstly, two test cases were performed to validate turbulence modelling, mesh and the modelling of particle-laden gas flows. In the first test case, i.e. flow in a concentric annulus, it was found that the standard $k-\epsilon$ model resembles the turbulent flow as evidenced by comparisons to RSM simulations and experimental data in the literature. Furthermore, in the second test case, i.e. confined bluff body flow, the results of a two-dimensional axisymmetric simulation were sufficient when compared to three-dimensional simulation and experimental data. In the confined bluff body flow the limitations of the $k-\epsilon$ model were revealed. The computed position of the second stagnation point was 15% downstream of the experimental position. However, better results were obtained for the dispersed phase in the second test case. The discrete particle model (DPM) in ANSYS Fluent is deemed able to simulate particle-laden gas flow, since good agreement between experimental data and simulations were obtained.

Secondly, two-dimensional axisymmetric simulations for the installed venturi scrubber was conducted. The numerical model was based on the findings of the two test cases. The computed pressure drop across the venturi scrubber was within the standard deviations of measurements obtained by Glencore Nikkelverk. In the present study, the CFD simulation predicted the pressure drop more accurately than empirical correlations and without the need of carefully choosing the correct factors and constants within the correlations. In the installed scrubber it is found that the largest particles may separate from the gas phase due to the high inertia and Stokes number. Finally, in the analysis of the planned full-scale venturi, it was found that all copper particles follow the gas phase to a large extent, caused by lower Stokes numbers. As a final point, the numerical model developed in this study is a good starting point for a future multiphase model in order to accurately predict the particle collection efficiency.

Chapter 8

Suggestions for Further Work

Based on the present study of turbulent flow in a concentric annulus it is evident that the RSM yields a more accurate representation of the flow than the two-equation turbulence models. The $k - \epsilon$ model was considered for the venturi scrubber as the details of the flow are not known from experiments. Therefore, more advanced measurements, e.g. PIV measurements, may contribute to a better overall understanding of the fluid dynamics in the venturi scrubber and enhance validation of the numerical simulations.

The proposed two-dimensional axisymmetric model imposes limitations on particle dispersion, turbulence modelling and swirling effects. Therefore, three-dimensional computations may be considered. In addition, a more comprehensive mesh study for the venturi scrubber is desired due to the findings in the first test case. The findings of this test case also indicated that resolving the turbulent boundary layer yields more accurate results.

Considerations outside the scope of this thesis are needed to accurately predict the collection efficiency. Firstly, based on the conducted literature study the most important collection mechanism is impaction. Therefore, the liquid phase should be included in the numerical model. The newly implemented VOF to DPM CFD spray model in ANSYS Fluent may be considered, in addition to the interaction between the droplets and particles. By introducing a liquid phase in the numerical model, parameters such as the liquid-to-gas ratio, pressure drop components and droplet size may be studied. Another suggestion is to investigate different operating conditions, e.g. plug settings. The position of the plug determines the cross-sectional area at the throat, thus the throat velocity and the pressure drop are affected.

Chapter 9

References

[1] Forurensningsloven, LOV-1981-03-13-6. https://lovdata.no/dokument/NL/lov/1981-03-13-6.

[2] ANSYS Fluent Theory Guide. https://www.sharcnet.ca/Software/Ansys/18.2.2/en-us/help/flu_th/flu_th.html, 2018.

[3] ANSYS Fluent User's Guide. https://www.sharcnet.ca/Software/Ansys/18.2.2/en-us/help/flu_ug/flu_ug.html, 2018.

[4] M. Ali, Y. C. Qi, and K. Mehboob. A Review of Performance of a Venturi Scrubber. *Research Journal of Applied Sciences, Engineering and Technology*, 4(19):3811–3818, 2012.

[5] R. Allen and A. van Santen. Designing for Pressure Drop in Venturi Scrubbers: The Importance of Dry Pressure Drop. *The Chemical Engineering Journal and the Biochemical Engineering Journal*, 61(3):203 – 211, 1996.

[6] M. Alletto and M. Breuer. One-way, two-way and four-way coupled LES predictions of a particle-laden turbulent flow at high mass loading downstream of a confined bluff body. *International Journal of Multiphase Flow*, 45:70–90, 2012.

[7] H. I. Andersson. *Introduction to turbulence modelling*. NTNU, Trondheim, 1988.

[8] I. Azouz and S. Shirazi. Evaluation of several turbulence models for turbulent flow in concentric and eccentric annuli. *Journal of Energy Resources Technology*, 120(4), 1998.

[9] B. Azzopardi. Gas-liquid flows in cylindrical venturi scrubbers: Boundary layer separation in the diffuser section. *The Chemical Engineering Journal*, 49(1):55–64, 1992.

[10] B. Azzopardi. Liquid distribution in venturi scrubbers: the importance of liquid films on the channel walls. *Chemical Engineering Science*, 48(15):2807–2813, 1993.

[11] B. Azzopardi, S. Teixeira, A. Govan, and T. Bott. Improved model for pressure drop in venturi scrubbers. *Process Safety and Environmental Protection: Transactions of the Institution of Chemical Engineers, Part B*, 69(4):237–245, 1991.

[12] T. Barth and D. Jespersen. The design and application of upwind schemes on unstructured meshes. In *27th Aerospace sciences meeting*, page 366, 1989.

[13] M. Bern and D. Eppstein. Mesh generation and optimal triangulation. *Computing in Euclidean geometry*, 1:23–90, 1992.

[14] B. Boersma and W.-P. Breugem. Numerical simulation of turbulent flow in concentric annuli. *Flow, Turbulence and Combustion*, 86(1):113–127, 2011.

[15] J. Boree, T. Ishima, and I. Flour. The effect of mass loading and inter-particle collisions on the development of the polydispersed two-phase flow downstream of a confined bluff body. *Journal Of Fluid Mechanics*, 443:129–165, 2001.

[16] S. Calvert. Venturi and other atomizing scrubbers efficiency and pressure drop. *AIChE Journal*, 16(3):392–396, 1970.

[17] H. Chen and V. Patel. Near-wall turbulence models for complex flows including separation. *AIAA journal*, 26(6):641–648, 1988.

[18] S. Y. Chung, G. H. Rhee, and H. J. Sung. Direct numerical simulation of turbulent concentric annular pipe flow: Part 1: Flow field. *International Journal of Heat and Fluid Flow*, 23(4):426–440, 2002.

[19] J. R. Couper, W. R. Penney, J. R. Fair, and S. M. Walas. Solid-liquid separation. In *Chemical Process Equipment - Selection and Design*, pages 709–717. Elsevier, 3rd edition edition, 2012.

[20] T. Craft, B. Launder, and K. Suga. Development and application of a cubic eddy-viscosity model of turbulence. *International Journal of Heat and Fluid Flow*, 17(2):108 – 115, 1996.

[21] C. T. Crowe, J. D. Schwarzkopf, M. Sommerfeld, and Y. Tsuji. *Multiphase flows with droplets and particles*. CRC Press Inc, Boca Raton, 2nd ed. edition, 2012.

[22] P. A. Cundall and O. D. L. Strack. A discrete numerical model for granular assemblies. *Geotechnique*, 29(1):47–65, 1979.

[23] G. Cusano, M. R. Gonzalo, F. Farrell, R. Remus, S. Roudier, and L. D. Sancho. Best Available Techniques (BAT) Reference Document for the Non-Ferrous Metals Industries, Industrial Emissions Directive 2010/75/EU. Technical report, Seville, Spain, 2017.

[24] B. J. Daly and F. H. Harlow. Transport equations in turbulence. *Physics of Fluids*, 13(11):2634–2649, 1970.

[25] J. A. Danielson, editor. *Air Pollution Engineering Manual*. U.S. Enviromental Protection Agency, Los Angeles, 2nd ed. edition, 1973.

[26] N. Deen, M. Sint Annaland, van, M. Hoef, van der, and J. Kuipers. Review of discrete particle modeling of fluidized beds. *Chemical Engineering Science*, 62(1-2):28–44, 2007.

[27] J. Eggels, F. Unger, M. Weiss, J. Westerweel, R. Adrian, R. Friedrich, and F. Nieuwstadt. Fully-developed turbulent pipe-flow - a comparison between direct numerical-simulation and experiment. *Journal Of Fluid Mechanics*, 268:175–209, 1994.

[28] S. Elghobashi. On predicting particle-laden turbulent flows. *Applied Scientific Research*, 52(4):309–329, 1994.

[29] J. H. Ferziger. *Computational Methods for Fluid Dynamics*. Springer-Verlag Berlin and Heidelberg GmbH Co. K, Berlin, Heidelberg, 3rd ed. edition, 2002.

[30] J. R. Fessler and J. K. Eaton. Turbulence modification by particles in a backward-facing step flow. *Journal of Fluid Mechanics*, 394:97–117, 1999.

[31] M. M. Gibson and B. E. Launder. Ground effects on pressure fluctuations in the atmospheric boundary layer. *Journal of Fluid Mechanics*, 86(3):491–511, 1978.

[32] C. Goniva, Z. Tukovic, C. Feilmayr, T. Burgler, and S. Pirker. Simulation of offgas scrubbing by a combined eulerian-lagrangian model. In *Seventh International Conference on CFD in the Minerals and Process Industries, CSIRO, Melbourne, Australia*, pages 09–11, 2009.

[33] F. Greifzu, C. Kratzsch, T. Forgber, F. Lindner, and R. Schwarze. Assessment of particle-tracking models for dispersed particle-laden flows implemented in OpenFOAM and ANSYS FLUENT. *Engineering Applications of Computational Fluid Mechanics*, 10(1):30–43, 2016.

[34] W. Gretler and W. Meile. Shear stress calculation in asymmetric turbulent flows: a combined ars-model. *Fluid Dynamics Research*, 14(6):289–311, 1994.

[35] V. Guerra, R. Bettega, J. Goncalves, and J. Coury. Pressure drop and liquid distribution in a venturi scrubber: Experimental data and cfd simulation. *Industrial & Engineering Chemistry Research*, 51(23):8049–8060–8049–8060, 2012.

[36] M. Hallbäck, J. Groth, and A. V. Johansson. An algebraic model for nonisotropic turbulent dissipation rate in reynolds stress closures. *Physics of Fluids A: Fluid Dynamics*, 2(10):1859–1866, 1990.

[37] V. Hernandez-Perez, M. Abdulkadir, and B. Azzopardi. Grid Generation Issues in the CFD Modelling of Two-Phase Flow in a Pipe. *The Journal of Computational Multiphase Flows*, 3(1):13–26, 2011.

[38] G. Iaccarino, A. Ooi, P. Durbin, and M. Behnia. Reynolds averaged simulation of unsteady separated flow. *International Journal of Heat and Fluid Flow*, 24(2):147 – 156, 2003.

[39] A. Japper-Jaafar, M. Escudier, and R. Poole. Laminar, transitional and turbulent annular flow of drag-reducing polymer solutions. *Journal of Non-Newtonian Fluid Mechanics*, 165(19-20):1357–1372, 2010.

[40] H. Jin, Y. Chen, J. Fan, and K. Luo. LES/FDF simulation of a gas-particle backward-facing step flow. *Chemical Engineering Science*, 66(16):3692–3700, 2011.

[41] J. Kim, P. Moin, and R. Moser. Turbulence statistics in fully developed channel flow at low reynolds number. *Journal of Fluid Mechanics*, 177(-1):133–166, 1987.

[42] B. Kjellstroem and S. Hedberg. On shear stress distributions for flow in smooth or partially rough annuli. Technical report, Technical Report No. AE-243, AB Atomenergi, Nykoeping, Sweden, 1966.

[43] R. Kristoffersen. Engineering Fluid Mechanics TEP4545, 2018.

[44] B. Launder and D. Spalding. *Mathematical models of turbulence*. Academic Press, London, 1972.

[45] B. Launder and D. Spalding. The numerical computation of turbulent flows. *Computer Methods in Applied Mechanics and Engineering*, 3(2):269–289, 1974.

[46] B. E. Launder. Second-moment closure: present and future. *International Journal of Heat and Fluid Flow*, 10(4):282 – 300, 1989.

[47] B. E. Launder and N. Shima. Second-moment closure for the near-wall sublayer - Development and application. *AIAA Journal*, 27(10):1319–1325, 1989.

[48] F. Lien and M. Leschziner. Assessment of turbulence-transport models including non-linear RNG eddy-viscosity formulation and second-moment closure for flow over a backward-facing step. *Computers and Fluids*, 23(8):983–1004, 1994.

[49] N.-S. Liu and X.-Y. Lu. Large eddy simulation of turbulent flows in a rotating concentric annular channel. *International journal of heat and fluid flow*, 26(3):378–392, 2005.

[50] H. Lu and W. Zhao. Numerical study of particle deposition in turbulent duct flow with a forward- or backward-facing step. *Fuel*, 234:189–198, 2018.

[51] J. L. Lumley. Toward a turbulent constitutive relation. *Journal of Fluid Mechanics*, 41(2):413–434, 1970.

[52] J. M. Kuerten. Point-Particle DNS and LES of particle-laden turbulent flow - a state-of-the-art review. *Flow, Turbulence and Combustion*, 97(3):689–713, 2016.

[53] F. R. Menter. Two-equation eddy-viscosity turbulence models for engineering applications. *AIAA Journal*, 32(8):1598–1605, 1994.

[54] B. Miller. 3 - particulate formation and control technologies. In B. Miller, editor, *Fossil Fuel Emissions Control Technologies*, pages 145 – 196. Butterworth-Heinemann, 2015.

[55] S. Mochizuki and F. Nieuwstadt. Reynolds-number-dependence of the maximum in the streamwise velocity fluctuations in wall turbulence. *Experiments in Fluids*, 21(3):218–226, 1996.

[56] S. Morsi and A. Alexander. An investigation of particle trajectories in two-phase flow systems. *Journal of Fluid mechanics*, 55(2):193–208, 1972.

[57] F. Moukalled. The finite volume method in computational fluid dynamics : An advanced introduction with OpenFOAM and Matlab, 2016.

[58] D. Mussatti and P. Hemmer. *EPA Air Pollution Control Cost Manual, EPA/452/B-02-001.* U.S. Envirmoental Protection Agency, Office of Air Quality Planning and Standards, 6th ed. edition, 2002.

[59] J. Nouri, H. Umur, and J. Whitelaw. Flow of newtonian and non-newtonian fluids in concentric and eccentric annuli. *Journal Of Fluid Mechanics*, 253:617–641, 1993.

[60] S. Pak and K. Chang. Performance estimation of a venturi scrubber using a computational model for capturing dust particles with liquid spray. *Journal of Hazardous Materials*, 138(3):560–573, 2006.

[61] S. Patankar and D. Spalding. A calculation procedure for heat, mass and momentum transfer in three-dimensional parabolic flows. *International Journal of Heat and Mass Transfer*, 15(10):1787–1806, 1972.

[62] R. H. Perry. *Perry's Chemical Engineers' Handbook.* McGraw-Hill, New York, 7th edition, 1997.

[63] R. H. Pletcher. Computational Fluid Mechanics and Heat Transfer, 2013.

[64] L. Prandtl. 7. Bericht über Untersuchungen zur ausgebildeten Turbulenz. *ZAMM-Journal of Applied Mathematics and Mechanics/Zeitschrift für Angewandte Mathematik und Mechanik*, 5(2):136–139, 1925.

[65] V. Ranade and D. Gupta. *Computational Modeling of Pulverized Coal Fired Boilers*. Taylor & Francis, 2014.

[66] K. Rehme. Turbulent flow in smooth concentric annuli with small radius ratios. *Journal of Fluid Mechanics*, 64(2):263–288, 1974.

[67] C. M. Rhie and W. L. Chow. Numerical study of the turbulent flow past an airfoil with trailing edge separation. *AIAA Journal*, 21(11):1525–1532, 1983.

[68] E. Riber, V. Moureau, M. Garcìa, T. Poinsot, and O. Simonin. Evaluation of numerical strategies for large eddy simulation of particulate two-phase recirculating flows (book review). *Journal of Computational Physics*, 228(2):539–564, 2009.

[69] P. Roache. Perspective - a method for uniform reporting of grid refinement studies. *ASME, Transactions, Journal of Fluids Engineering (0098-2202)*, 116(3):405–413, 1994.

[70] W. Rodi. A new algebraic relation for calculating the Reynolds stresses. *Gesellschaft Angewandte Mathematik und Mechanik Workshop Paris France*, 56, Mar. 1976.

[71] F. E. Rodriguez-Corredor, M. Bizhani, M. Ashrafuzzaman, and E. Kuru. An experimental investigation of turbulent water flow in concentric annulus using particle image velocimetry technique. *Journal of Fluids Engineering*, 136(5), 2014.

[72] D. Schellander. *CFD simulations of particle laden flows: Particle transport and separation*. Anchor Academic Publishing, 2014.

[73] K. Schifftner and H. Hesketh. *Wet Scrubbers*. Technomic Publishing, Lancaster, PA, 2nd ed. edition, 1996.

[74] J. G. Slettedal. Numerical Investigation of Gas Flow with Particles, 2018.

[75] A. Sobachkin and G. Dumnov. Numerical basis of CAD-embedded CFD. In *NAFEMS World Congress*, pages 9–12, 2013.

[76] D. L. Sondak. Wall functions for the $k-\epsilon$ turbulence model in generalized nonorthogonal curvilinear coordinates. 1992.

[77] P. Spalart. Strategies for turbulence modelling and simulations. *International Journal of Heat and Fluid Flow*, 21(3):252–263, 2000.

[78] C. Speziale. On nonlinear $k - l$ and $k - \epsilon$ models of turbulence. *Journal of Fluid Mechanics*, 178:459–475, 1987.

[79] C. G. Speziale, S. Sarkar, and T. B. Gatski. Modelling the pressure-strain correlation of turbulence: an invariant dynamical systems approach. *Journal of Fluid Mechanics*, 227:245–272, 1991.

[80] G. G. Stokes. On the effect of internal friction on the motion of a pendulum. *Trans. Camb. Phil. Soc.*, 9:8–16, 1851.

[81] H. Tennekes and J. L. Lumley. *A first course in turbulence*. MIT Press, Cambridge, 1972.

[82] C. Tropea, A. L. Yarin, and J. F. Foss. *Springer Handbook of Experimental Fluid Mechanics*. Springer Verlag, 2007.

[83] M. A. van der Hoef, M. van Sint Annaland, N. Deen, and J. Kuipers. Numerical simulation of dense gas-solid fluidized beds: a multiscale modeling strategy. *Annu. Rev. Fluid Mech.*, 40:47–70, 2008.

[84] A. Y. Varaksin. *Turbulent Particle-Laden Gas Flows*, volume 41 of *Atomic, optical, and plasma physics*. Springer, Berlin, Heidelberg, 2007.

[85] S. P. Vegendla, G. J. Heynderickx, and G. B. Marin. Comparison of Eulerian-Lagrangian and Eulerian-Eulerian method for dilute gas-solid flow with side inlet. *Computers & Chemical Engineering*, 35(7):1192–1199, 2011.

[86] S. Viswanathan. Development of a pressure drop model for a variable throat venturi scrubber. *Chemical Engineering Journal*, 71(2):153–160, 1998.

[87] L. K. Wang, N. C. Pereira, and Y.-T. Hung. *Air Pollution Control Engineering*, volume 1 of *Handbook of Environmental Engineering ;*. Humana Press, Totowa, NJ, 2004.

[88] D. C. Wilcox et al. *Turbulence modeling for CFD*, volume 2. DCW industries La Canada, CA, 1998.

[89] M. Wolfshtein. The Velocity and Temperature Distribution of One-Dimensional Flow with Turbulence Augmentation and Pressure Gradient. *International Journal of Heat and Mass Transfer*, 12:301–318, 03 1969.

[90] X. Xiong, M. Rahman, and Y. Zhang. RANS Based Computational Fluid Dynamics Simulation of Fully Developed Turbulent Newtonian Flow in Concentric Annuli. *Journal of Fluids Engineering, Transactions of the ASME*, 138(9), 2016.

[91] J. Zhu, T.-H. Shih, and J. L. Lumley. A New Reynolds Stress Algebraic Equation Model - NASA-TM-106644. Technical report, NASA, 1994.

Appendices

Appendix A

The drag coefficient for spherical particles

The drag coefficient equations used in equation 2.69 are:
$C_D = \frac{24}{Re_P}$ for $Re_P < 0.1$
$C_D = 3.69 + \frac{22.73}{Re_P} + \frac{0.0903}{Re_P^2}$ for $0.1 < Re_P < 1.0$
$C_D = 1.222 + \frac{29.1667}{Re_P} - \frac{3.8889}{Re_P^2}$ for $1.0 < Re_P < 10.0$
$C_D = 0.6167 + \frac{46.5}{Re_P} - \frac{116.67}{Re_P^2}$ for $10.0 < Re_P < 100.0$
$C_D = 0.3644 + \frac{98.33}{Re_P} - \frac{2778}{Re_P^2}$ for $100.0 < Re_P < 1000.0$
$C_D = 0.357 + \frac{148.62}{Re_P} - \frac{4.75 \cdot 10^4}{Re_P^2}$ for $1000.0 < Re_P < 5000.0$

Appendix B

Installed venturi scrubber geometry

See next page.
Note:

1. All dimensions in mm.
2. The bushing for the plug axle is not considered in the geometry in this study.
3. The nozzle is not present in the geometry in the CFD simulations.

Installed venturi scrubber geometry

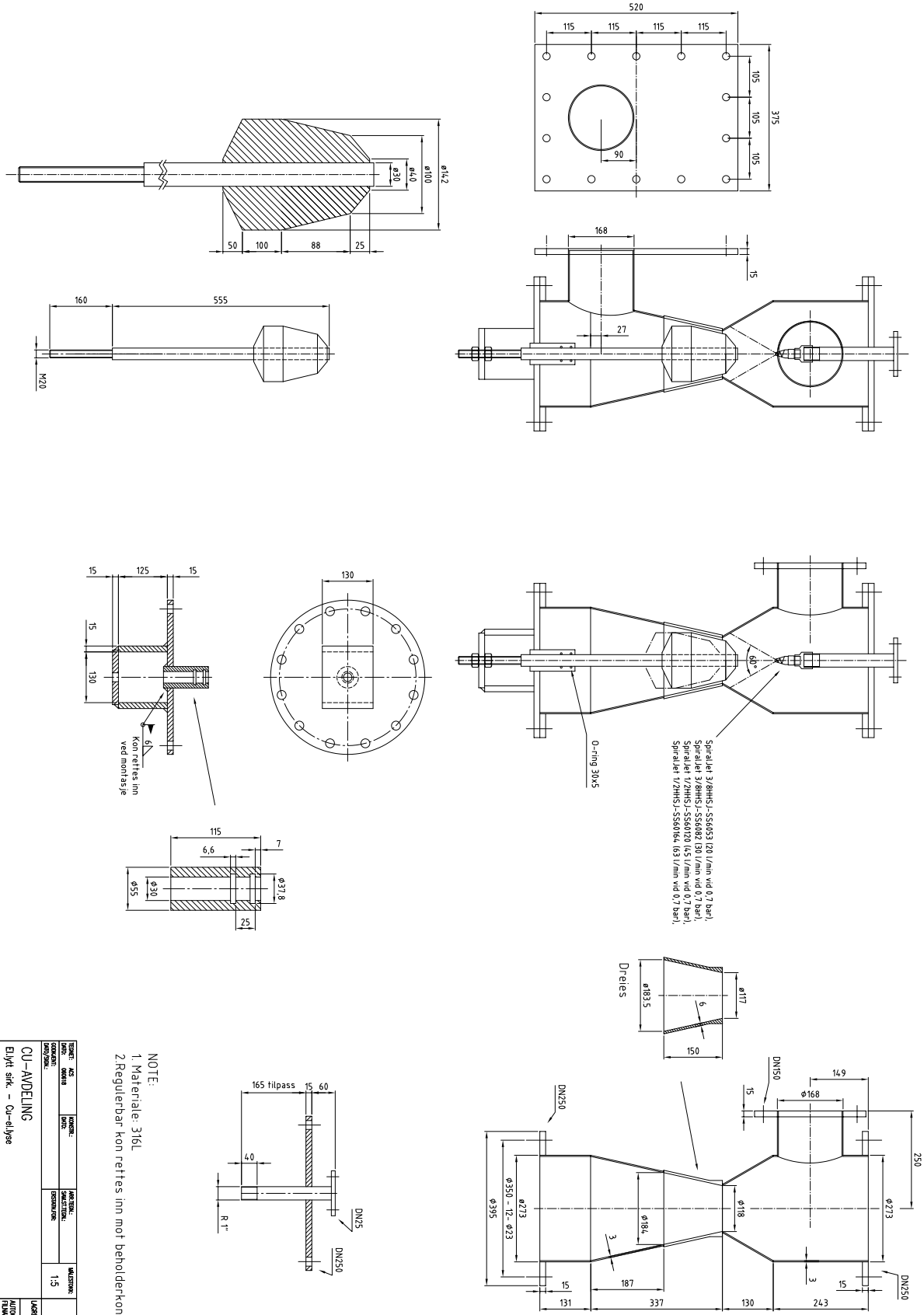

NOTE:
1. Materiale: 316L
2. Reguleerbar kon rettes inn mot beholderkon.

MERKS	FORANDR.	DATO	SIGN.	TEGNET: AKS 060618	KONTR.: DATO:	ARK.TEGN.: SAKSTEGN.:	MÅLESTOKK: 1:5
				KOPIERT: DATO:			
						ERSTATTER:	

CU-AVDELING
Elykt sirk. - Cu-elyse
Long pilotonk i Cu 6
Ny forsøksskrubber

Pos. 58110
Detalj

NIKKELVERK
A GLENCORE COMPANY

LAGRET: A57\058\11D\MEK
AUTOCAD-FILNAVN: 058110-0240
TEGN.NR.: 1-25757
REV.:

Appendix C

Force balance for concentric annulus

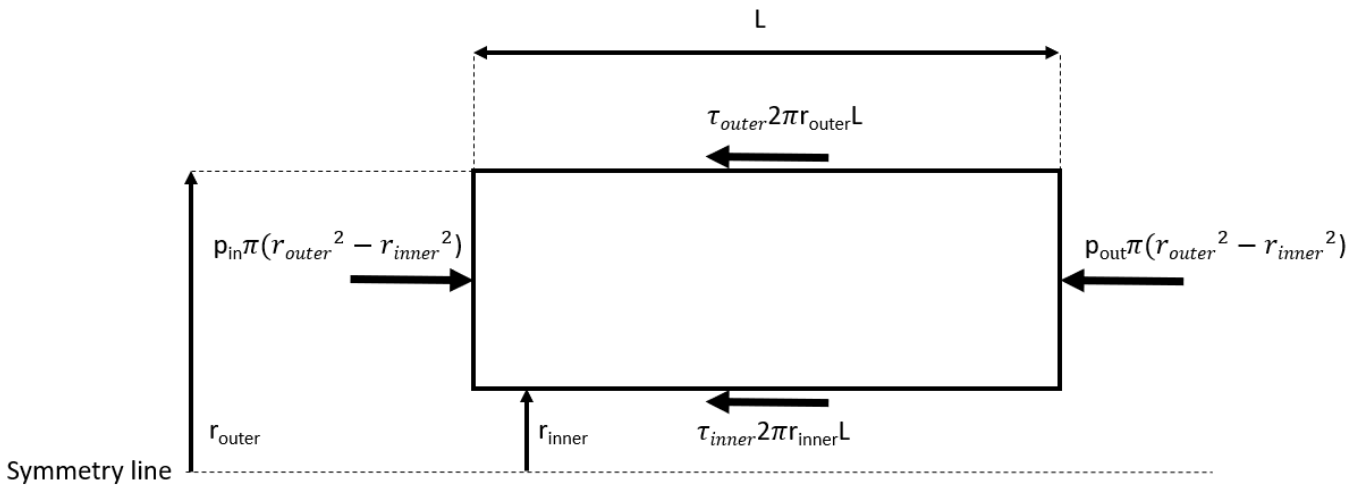

Figure C.1 Annulus force balance.

Appendix D

Installed scrubber results

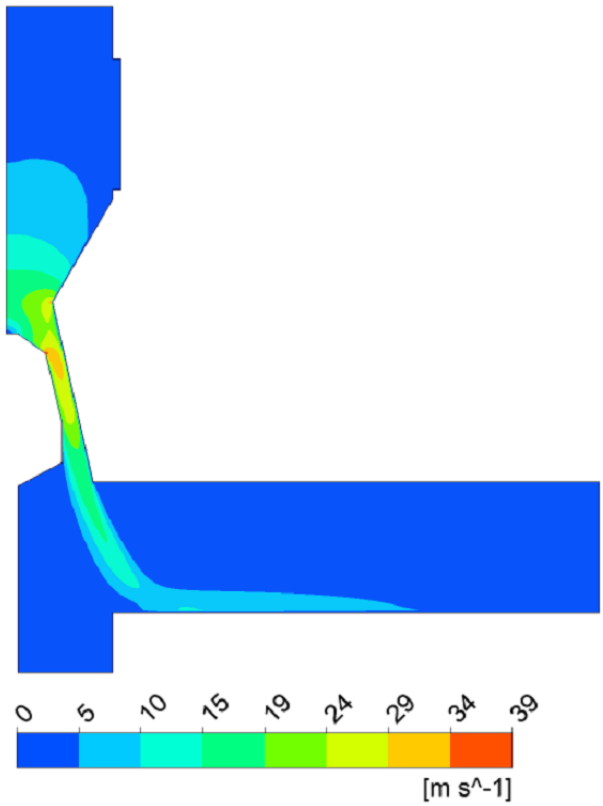

Figure D.1 Velocity magnitude for gas phase at $Q = 0.2631\ m^3/s$.

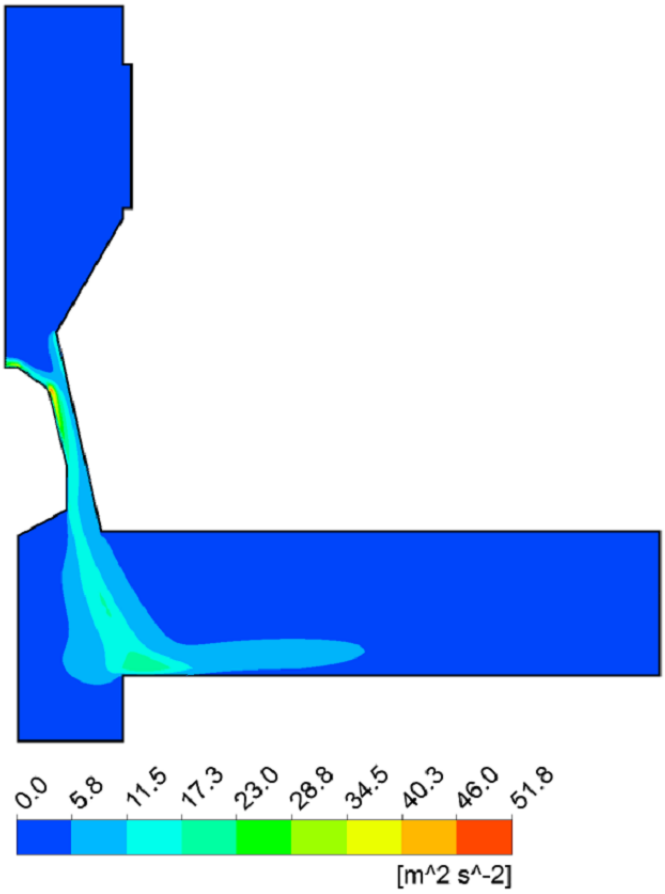

Figure D.2 Turbulent kinetic energy at $Q = 0.2631\ m^3/s$.

Appendix E

Pressure measurement, Glencore Nikkelverk

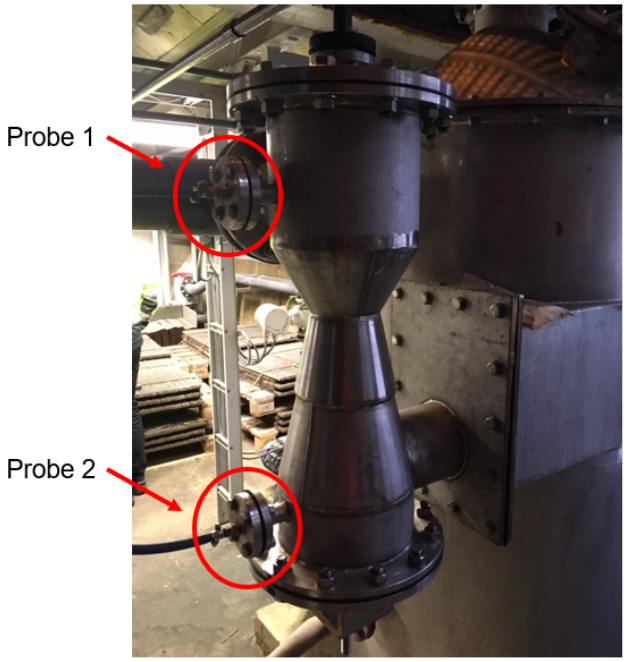

Figure E.1 Positions of pressure measurement.

Appendix F

Full-scale venturi scrubber results

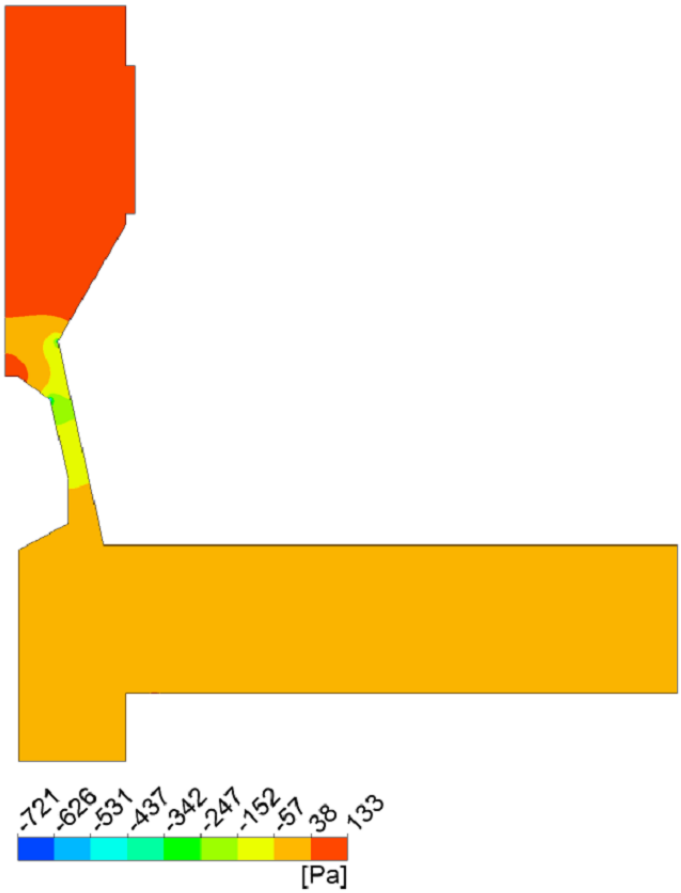

Figure F.1 Static pressure at $Q = 19.44\ m^3/s$.

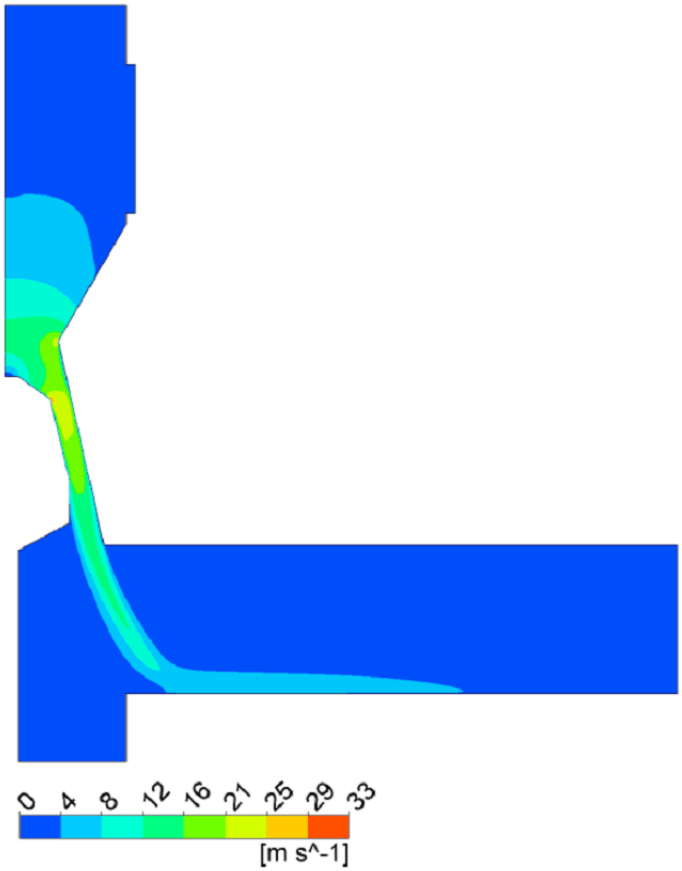

Figure F.2 Velocity magnitude of gas phase at $Q = 19.44\ m^3/s$.

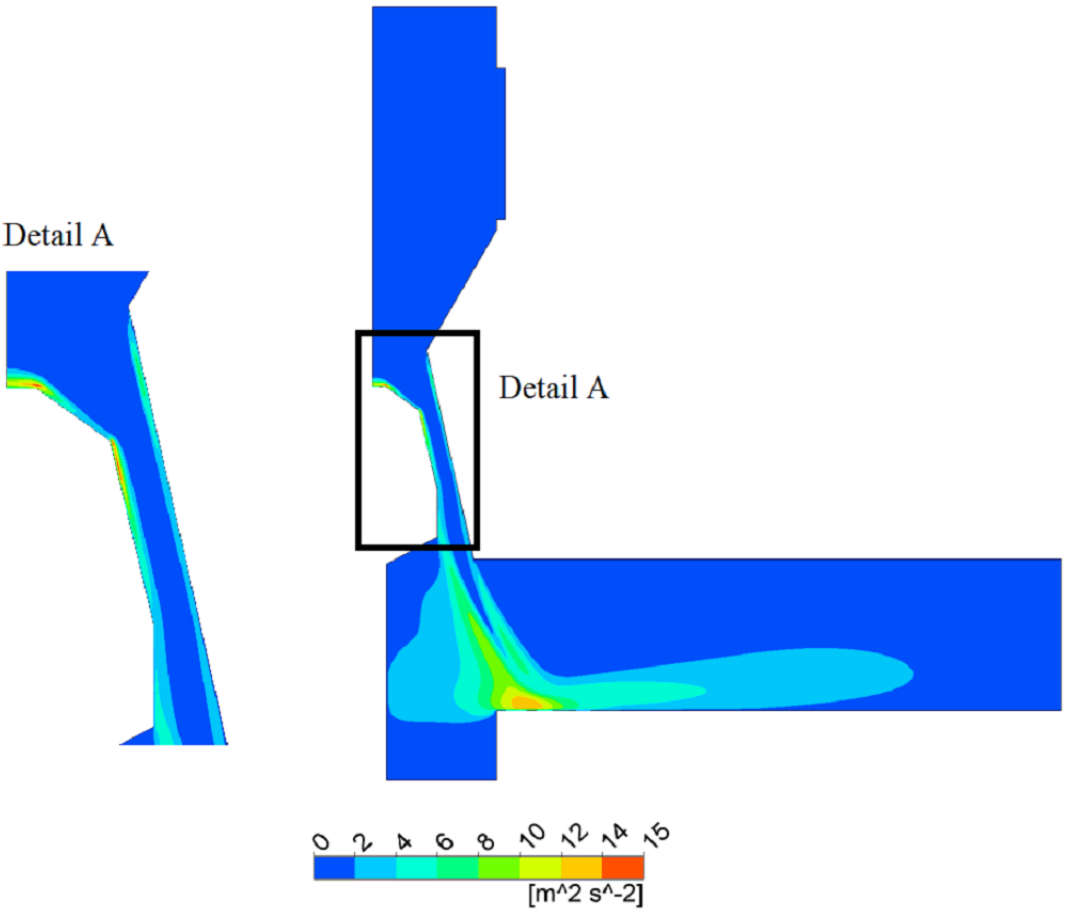

Figure F.3 Turbulent kinetic energy at $Q = 19.44\ m^3/s$.

Jens Gunnar Slettedal

Numerical Investigation of Scrubber

NTNU
Kunnskap for en bedre verden

NIKKELVERK
A GLENCORE COMPANY